Immuno-SPECT Imaging of Aberrant p53 Expression in Pancreatic Ductal Adenocarcinoma



Hudson Alakonya

Linacre College

University of Oxford

A thesis submitted for the degree of

Doctor of Philosophy

Hillary term 2023

Contents

LIST OF FIGURES ..... **VI**

ACKNOWLEDGEMENTS ..... **IX**

ABSTRACT ..... **XII**

ABBREVIATIONS ..... **XIV**

1 CHAPTER 1 – INTRODUCTION **1**

1.1 PANCREATIC CANCER 2

1.1.1 The pancreas anatomy and function *3*

1.1.2 Forms of pancreatic cancer *3*

1.1.3 Pancreatic ductal adenocarcinoma *5*

1.1.3.1 Pancreatic intraepithelial neoplasia (PanINs) 5

1.1.3.2 Intraductal papillary mucinous neoplasms (IPMNs) 6

1.1.3.3 Mucinous cystic neoplasms (MCNs) 8

1.1.4 Risk factors *8*

1.1.5 State of the art PDAC diagnosis and challenges *10*

1.1.6 PDAC treatment *12*

1.2 THE TUMOUR SUPPRESSOR PROTEIN P53 14

1.2.1 TP53 gene *14*

1.2.2 p53 structure and regulation *15*

1.2.3 p53 function *19*

1.2.4 p53 mutations in human cancers *20*

1.2.5 p53 aberrance in pancreatic ductal adenocarcinoma *22*

1.3 MOLECULAR IMAGING 23

1.3.1 SPECT imaging *24*

1.3.2 Molecular imaging agents *26*

1.3.2.1 Monodonal antibodies 27

1.3.2.2 Peptides 29
1.3.3 Cell penetrating peptides 31
1.3.3.1 HIV trans-Activator of transcription peptide (TAT) 32
1.4 ANTIBODY CONJUGATION METHODS 35
1.4.1 Site-specific conjugation 35
1.4.2 Non-site-specific antibody conjugation 36
1.5 AIM OF THE PROJECT 39
2 CHAPTER 2 – PRODUCTION AND VALIDATION OF A NOVEL ANTI-P53 MAB 40
2.1 INTRODUCTION 41
2.2 SELECTION AND VALIDATION OF NEW ANTI-P53 HYBRIDOMA CLONES 43
2.2.1 Materials and methods 43
2.2.1.1 Cell culture 43
2.2.1.2 Anti-p53 hybridomas 44
2.2.2 Western blot 44
2.2.2.1 Cell lysate preparation 44
2.2.2.2 SDS-PAGE & western blot 45
2.2.3 Flow cytometry 46
2.2.4 Immunocytochemistry 46
2.2.5 Determination of p53 Protein expression in Pancreatic Cancer Cell Lines 47
2.2.5.1 Western Blot 47
2.2.5.2 SDS-PAGE & western blot 48
2.2.5.3 ELISA 48
2.3 PRODUCTION AND PURIFICATION OF ANTI-P53 49A1/H10 MONOCLONAL ANTIBODY 49
2.3.1 Anti-p53 49A1/H10 hybridomas culture 49
2.3.2 FPLC Purification (Protein G Column) 50
2.3.3 Reducing and non-reducing SDS-PAGE 51
2.3.4 Saturation binding assay 51
2.3.5 Statistical analysis 52
2.4 RESULTS 53

2.4.1 Validation of anti-p53 (49A1/H10) monoclonal antibody *53*

2.4.1.1 Western blot analysis 53

2.4.1.2 Flow cytometry analysis 54

2.4.1.3 Confocal microscopy 55

2.4.1.4 Anti-p53 49A1/H10 mAb binds to total p53 55

2.4.1.5 Anti-p53 production and purification 58

2.4.1.6 Evaluation of antibody affinity by flow cytometry 58

2.4.2 Evaluation of p53 protein levels in a panel of pancreatic cancer cell lines *59*

2.4.2.1 Western blot analysis of p53 protein levels 59

2.4.2.2 Evaluation of protein levels by ELISA 60

2.5 DISCUSSION 61

2.6 CONCLUSION 67

3 CHAPTER 3 – SYNTHESIS OF RICS AND *IN VITRO* VALIDATION 69

3.1 INTRODUCTION 70

3.2 MATERIAL AND METHODS 72

3.2.1 Conjugation od STP-DBCO on 49A1/H10 mAb via click chemistry *72*

3.2.2 Bioconjugation of anti-p53 49A1/H10 Monoclonal antibody *73*

3.2.3 Radiolabelling of DTPA-Bn-49A1/H10-TAT conjugates with [^{111}In]Cl3 ..... *73*

3.2.3.1 Quality control by iTLC 74

3.2.3.2 In vitro stability in serum 74

3.2.3.3 Effect of [^{111}In]-DTPA-Bn-49A1/H10-TAT on cell viability 74

3.2.4 In vitro cell uptake of radioimmunoconjugates *75*

3.2.5 In vitro retention of radioimmunoconjugates *76*

3.2.6 Immunoreactivity of DTPA-Bn-49A1/H10-TAT *76*

3.2.7 Cell-based competitive radioimmunoassay *77*

3.2.8 Statistical analysis *77*

3.3 RESULTS 78

3.3.1 Radioconjugation of Anti-total p53 (49A1/H10) and MIgG mAb with TAT and indium-111 ..... *78*

3.3.2 In vitro stability of [^{111}In]-labelled antibodies *79*

3.3.3 Immunoreactivity of [^{111}In]-labelled anti-total p53 (49A1/H12) ... *80*

3.3.4 Comparison of blocking properties of [^{111}In]-labelled Anti-total p53 (49A1/H12) ... *81*

3.3.5 In vitro cell toxicity of [^{111}In]-labelled antibodies ... *82*

3.3.6 In vitro uptake of [^{111}In]-labelled antibodies ... *83*

3.3.7 In vitro retention of [^{111}In]-labelled antibodies ... *84*

3.4 DISCUSSION ... 86

3.5 CONCLUSION ... 91

4 CHAPTER 4 – IMMUNO-SPECT IMAGING OF P53 IN SUBCUTANEOUS MOUSE XENOGRAFTS ... 92

4.1 INTRODUCTION ... 93

4.2 MATERIAL AND METHODS ... 94

4.2.1 Mouse models ... *94*

4.2.2 Cell preparation for inoculations ... *94*

4.2.3 Radiolabelling of DTPA-Bn-49A1/H10-TAT conjugates with [^{111}In]Cl_3 ... *95*

4.2.4 SPECT/CT acquisition and image analysis ... *95*

4.2.5 Image analysis ... *96*

4.2.6 Histological analysis of tumour xenografts ... *96*

4.2.6.1 Immunohistochemical staining ... 96

4.2.6.2 Autoradiography ... 97

4.2.7 Statistical analysis ... *98*

4.3 RESULTS ... 98

4.3.1 Biodistribution of Anti-p53 (49A1/H12) and MIgG RICs in p53 xenograft models ... *98*

4.3.2 In vivo SPECT imaging of p53 xenografts ... *100*

4.3.3 Histological analysis of xenografts ... *104*

4.4 DISCUSSION ... 107

4.5 CONCLUSION ... 111

5 CHAPTER 5 – *IN VITRO* SCREENING AND VALIDATION OF P53-TARGETING SMALL PEPTIDES ... 113

5.1 INTRODUCTION ... 114

5.2 MATERIAL AND METHODS ... 115

5.2.1 Cell lines *115*

5.2.2 Peptides *115*

5.2.3 Immunofluorescence microscopy *116*

5.2.4 Biotin-Peptide pull-down assay *117*

5.2.4.1 Anti-total p53 (49A1/H10) mAb biotinylation 117

5.2.4.2 Assay protocol 118

5.2.4.3 SDS-PAGE & western blot 118

5.2.5 MTT Assay to investigate the cytotoxicity of peptides *119*

5.2.6 Statistical analysis *120*

5.3 RESULTS 120

5.3.1 Anti-total p53 (49A1/H10) mAb – peptide colocalization assay *120*

5.3.2 Analysis of peptides interaction with mutant p53 protein by pulldown assay *122*

5.3.3 Peptides cell viability effect *125*

5.4 DISCUSSION 126

5.5 CONCLUSION 130

6 OVERALL DISCUSSION AND FUTURE WORK 132

7 BIBLIOGRAPHY 145

8 APPENDIX 170

8.1 WESTERN BLOT 170

8.2 BIODISTRIBUTION DATA IN PERCENTAGE INJECTED DOSE PER GRAM (%ID/G) 171

8.3 SPECT IMAGES VOI DATA INJECTED ACTIVITY PER MILLILITRE (IA/ML) 173

8.4 DEDICATION 175

List of figures

Chapter 1 – Introduction

Figure 1:1) Anatomical location of the pancreas.....4

Figure 1:2) The Multistep histopathogenesis of PDAC.....7

Figure 1:3) The domain structure of human p53.....17

Figure 1:4) The p53 regulation pathway and function.....19

Figure 1:5) Illustration of SPECT imaging of mouse.....25

Figure 1:6) The basic structure of a mAb and its fragmented domains.....28

Figure 1:7) The HIV-1 TAT peptide.....34

Chapter 2 – Production and validation of a novel anti-p53 mAb

Figure 2:1) Western blot analysis of p53 antibodies.....54

Figure 2:2) Flow cytometry validation of p53 antibodies.....56

Figure 2:3) Anti-total p53 49A1/H10 mAb localisation in the nucleus.....57

Figure 2:4) Immunoreactivity of anti-p53 (49A1/H10) mAb on total p53 protein.....58

Figure 2:5) SDS-PAGE gel images of purified 49A1/H10 mAb. A).....59

Figure 2:6) Analysis of 49A1/H10 mAb affinities using flow cytometry.....60

Figure 2:7) Quantification of p53 protein levels by Western blot and ELISA.....61

Chapter 3 – Anti-p53 mAb radioimmunoconjugates synthesis and *in vitro* validation

Figure 3:1) DBCO-N_3 monoclonal antibody radioconjugation method.....78

Figure 3:2) Radiochemical yield of RICs.....79

Figure 3:3) Stability of [^{111}In]-DTPA-49A1/H10 in PBS and serum.....80

Figure 3:4 Immunoreactivity of [^{111}In]-DTPA-49A1/H10-TAT.....81

Figure 3:5) MTT assay cell viability results after treatment with RICs and controls......82

Figure 3:6) Clonogenic results after exposure to RICs treatment for 14 days. 83

Figure 3:7) Cellular uptake of TAT conjugated and non-TAT conjugated RICs.....84

Figure 3:8) Cellular retention of Anti-p53 and MIgG RICs.....85

Chapter 4 – Immuno-SPECT imaging of p53 in subcutaneous mouse xenografts

Figure 4:1) Ex vivo biodistribution and uptake of Anti-p53 and MIgG RICs.....99

Figure 4:2) Ex vivo tumour uptake ratios.....100

Figure 4:3) In vivo imaging of RICs in MiaPaCa-2 tumours.....101

Figure 4:4) VOI analysis of MiaPaCa-2 SPECT images.....102

Figure 4:5) In vivo imaging of RICs in HT1080 tumours.....103

Figure 4:6) VOI analysis of HT1080 SPECT images.....104

Figure 4:7) In vivo imaging of Anti-p53 and MIgG RICs in H1299 tumours. 105

Figure 4:8) VOI analysis of H1299 SPECT images.....106

Figure 4:9) Immunohistochemistry analysis of xenograft tumour sections.....106

Figure 4:10) Autoradiography of xenograft tumour sections.....107

Chapter 5 – *In vitro* screening and validation of p53-targeting small peptides

Table 5.1) p53 targeting peptides.....116

Figure 5:1) FAMPAC-1 cells Immunofluorescence confocal microscopy. 121

Figure 5:2) MiaPaCa-2 cells Immunofluorescence confocal microscopy. 122

Figure 5:3) HT1080 cells immunofluorescence confocal microscopy. 123

Figure 5:4) H1299 immunofluorescence confocal microscopy and peptide cell uptake. 124

Figure 5:5) Biotin peptide-streptavidin pulldown assay of p53 with cell lysates.....125

Figure 5:6) MTT assay cell viability results after treatment with peptides 1 or 2. 127

Appendix

Figure 8:1) Western blot analysis of p53 antibodies.. 170

List of tables

Chapter 2 – Production and validation of a novel anti-p53 mAb

Table 2.1.1) p53 antibodies for validation. 44

Table 2.1.2) p53 cell lines used in monoclonal antibody validation experiments. 53

Chapter 5 – *In vitro* screening and validation of p53-targeting small peptides

Table 5.1) p53 targeting peptides. Where Cy5 DBCO (non-sulfonated) is attached to azidohexanoic acid (Azhx) via copper-free click chemistry 116

Appendix

Table 8.1) Biodistribution data (raw) of MiaPaCa-2 xenografts in %ID/g. (RIC – radioimmunoconjugate) 171

Table 8.2) Raw biodistribution data of HT1080 xenografts in %ID/g. 171

Table 8.3) Raw biodistribution data of H1299 xenografts in %ID/g. 172

Table 8.4) Raw data in IA/mL of [^{111}In]-DTPA-49A1/H10-TAT in MiaPaCa-2 xenografts. 173

Table 8.5) Raw data in IA/mL of [^{111}In]-DTPA-MIgG-TAT in MiaPaCa-2 xenografts. 173

Table 8.6) Raw data in IA/mL of [^{111}In]-DTPA-49A1/H10-TAT in HT1080 xenografts. 173

Table 8.7) Raw data in IA/mL of [^{111}In]-DTPA-MIgG-TAT in HT1080 xenografts. 173

Table 8.8) Raw data in IA/mL of [^{111}In]-DTPA-49A1/H10-TAT in H1299 xenografts. 173

Table 8.9) Raw data in IA/mL of [^{111}In]-DTPA-MIgG-TAT in H1299 xenografts. 173

Table 8.10) Anti-p53 (49A1/H10) mAb – peptides Pearson R correlation coefficients from coloco2 analysis. 174

Acknowledgements

I wish to express my sincere thanks to the people who have made this journey a success and contributed significantly to transforming my life.

Firstly, my immense gratitude goes to my supervisor Prof. Bart Cornelissen for giving me the single most opportunity to do my research in his lab. This was not only a great opportunity for me but a blessing to my country as I am the first Kenyan to pursue a DPhil in Oncology at Oxford. Your unconditional support and kindness towards me have been beyond my expectation. I believe I must have been the hardest research student you have ever supervised! But I am grateful that you helped me to navigate through my chronic personal challenges until we saw the light at the end of the tunnel. During my whole period in Oxford, I found another father and mother in you. I will forever owe you an immense debt of gratitude.

My laboratory research experience would not have been a success without the conscientious scientists in Cornelissen research group. Your support and motivation throughout my time at the RRI building were immeasurable. I am particularly grateful to Sam for helping me to acclimatise in the lab and training me majority of the preliminary experiments. Your counsel and guidance significantly improved my science. I felt so bad you had to leave for the USA! Mat, I honour you for improving antibody radioconjugation work by bringing to light the DBCO-N_3 monoclonal antibody radioconjugation method, and for training me through the whole protocol with utmost kindness. You are such an ingenious scientist with a great future ahead. During my last year, Gemma's presence and unconditional support were very invaluable. You sacrificed much of your time including weekends to lead me through

radioconjugation and *in vivo* experiments. I sincerely appreciate your generous support. I could have never asked for a better laboratory manager and neighbour than Mike. You never hesitated to show me where to locate the missing reagents and trained me in several protocols when I felt hopeless at the sea (more so the SP8 confocal microscopy). After you left in March 2022, your space became a large and endless desert of you not being there. I still owe you a gift from Kenya. Thank you 'grandpa.'

My life wouldn't have been the same without winning the Rhodes Scholarship. You recognised my academic excellence and generous ambitions while working as a casual labourer on the construction sites in Nairobi and gave me an opportunity to study at the world's most prestigious university. Since becoming a Rhodes Scholar in November 2016, the Rhodes Trust team led by Elizabeth, Mary and Paul have been very supportive to my studies and my family in Kenya. I am not sure I could have managed to push through the tedious and lonely journey without your wholehearted love and care. Leaving my one-week son and two-year daughter to come and begin my studies in the UK remain to be my biggest and most mentally tormenting decision I ever made. I am sincerely indebted to you all for constantly checking on me and supporting me to visit my young family every year. I hope to become a great transformational leader and contribute to the fulfilment of the Rhodes Trust vision.

I would also like to acknowledge and express my unwavering gratitude to Linacre College led by the principal Nick Brown, senior tutor Jane Hoverd and the accommodation manager Karren Morris. Your psychological support and counsel during 'my turbulent' moments at Oxford provided me with the impetus that contributed immensely to DPhil success. I am very much thankful for considering me for the Linacre college hardship funding that helped me to offset my financial burdens and stresses.

It would have been impossible for me to focus on my studies at Oxford without the love and prayers of my dad, mum, and grandma. You have always believed in me as the light of our family since I was a little boy. You sacrificed the little you had to educate me up to undergraduate level, making me the first university graduate in our village. I am forever Indebted to you. I hope my academic and career success brings you more happiness and a healthy life during your remaining years on earth. God bless you.

Last but not least, I wish to thank my little children Charlene and Graham for giving me every reason to work hard and push beyond the odds. Your love, smiles, hugs, and naughtiness have always warmed my heart. I am sorry that you have spent all your first years on earth without fatherly love. I promise to be with you soon and be the best dad always. My courageous and beautiful wife, Sheilah, thank you for your support and patience for the past five plus years, allowing me to successfully complete my MSc in Cancer and PhD in Oncology studies in the UK. I owe you and our sweet dolls a prosperous and inspiring life.

Finally, I am forever worshipful and grateful to Jesus Christ for his sufficient grace, mercy, and favour upon my life. In all my pursuits and circumstances, I am guided and supported by the abundant presence of God. I remain committed to my life purpose to serve, save, and transform lives.

Abstract

Pancreatic ductal adenocarcinoma (PDAC) is a notoriously ferocious malignancy arising from the head of the pancreas, with aggressive biology and early-onset metastases. PDAC develop and progress asymptomatically with over 80% of the patients presenting for diagnosis with inoperable metastatic tumours that are resistant to standard therapies. Late diagnosis has resulted a grim increase of the five-year survival statistics from less than 5% to 8% over the past four decades.

The TP53 gene is mutated in approximately 75% of invasive pancreatic intraepithelial neoplasia lesions (PanIN-3) and PDAC. Mutations of p53 plays an important role in PDAC tumorigenesis, and several mutants have been shown to be overexpressed in both PanIN-3 lesions and PDAC patients. Mutant p53 overexpression is associated with chemoresistance and poor prognosis among PDAC patients. Thus, imaging of p53 overexpression could pave a new path for early diagnosis of enriched high risk PDAC population, and stratifying patients in treatment groups. In this study, I envisioned to interrogate aberrant p53 expression in PDAC models using monoclonal antibody- and peptide-based radioimmunoconjugates (RICs). I aimed to develop radiolabelled imaging agents for early diagnosis and prognosis evaluation of PDAC.

I produced, purified, and validated a novel anti-total p53 monoclonal antibody (49A1/H10) with nanomolar affinity and high specificity and selectivity. 49A1/H10 was employed to quantify mutant p53 levels in a panel of pancreatic cancer cell lines. I then employed the strain-promoted alkyne-azide cycloaddition (SPAAC) click chemistry radioconjugation method (DBCO-N_3 method) to conjugate TAT cell penetrating peptide (CPP) and DTPA on 49A1/H10

mAb. DTPA-49A1/H10-TAT was further radiolabelled with indium-111 radionuclide [^{111}In] to yield [^{111}In]-DTPA-49A1/H10-TAT.

The cellular uptake and retention of [^{111}In]-DTPA-49A1/H10-TAT were investigated in three PDAC cell lines with varying p53 expression. Having completed the *in vitro* validation of the anti-total p53 RICs, I established subcutaneous p53 PDAC xenograft models and employed SPECT/CT to image and quantify the tumour uptake and biodistribution of [^{111}In]-DTPA-49A1/H10-TAT.

In the second part of my project, I attempted to validate p53-targeting peptides using *in vitro* techniques.

In this thesis, I establish preliminary evidence of SPECT imaging mutant p53 overexpression in PDAC models. This study opens new avenues for further exploring the suitability of imaging mutant p53 as a biomarker early diagnosis and prognosis evaluation of PDAC patients.

Abbreviations

[^{18}F]FDG] – 18F-fluorodeoxyglucose

ADC – Antibody drug conjugate

ARF – Alternative reading frame

ATM – Ataxia telangiectasia mutated

ATR – Ataxia telangiectasia and Rad3 related protein

BCA Assay – Bicinchoninic acid assay

BRCA 1 and 2 – Breast Cancer gene 1 & 2

CA19.9 – Carbohydrate antigen 19-9

CDKN2A – Cyclin dependent kinase inhibitor 2A

cDNA – complementary deoxyribonucleic acid

CEA – Carcinoembryonic antigen

CEACAM-6 – Carcinoembryonic cell adhesion molecule 6

CO_2 – Carbon dioxide

CPP – Cell penetrating peptide

CRISPR – Clustered regularly interspaced short palindromic repeats

CT – Computed tomography

DAPI – 4',6-diamidino-2-phenylindole

DAR – drug antibody ratio

DBCO – Dibenzocyclooctyne

DBD – p53 DNA binding domain

DMEM – Dulbecco's modified eagle medium

DNA – deoxyribonucleic acid

DNA-PK – DNA dependent protein kinase

DNE – dominant negative effect

DOTA – 2,2',2'',2'''-(1,4,7,10-Tetraazacyclododecane-1,4,7,10-tetrayl)tetraacetic acid

DREAM – Dimerization partner, RB-like, E2F and multi-vulval class

DTPA – Diethylenetriamine pentaacetate

ECM – Extracellular matrix

EDC/NHS – N-ethyl-N'-(3-(dimethylamino)propyl)carbodiimide/N-hydroxysuccinimide

EDTA – Ethylenediamine tetraacetic acid

EGFR – Epidermal growth factor receptor

ELISA – Enzyme-linked immunoassay

EPR – Enhanced permeability and retention

EUS-FNA – Endoscopic ultrasound-guided fine needle aspiration

Fab – Fragment antigen-binding region

FBS – Foetal bovine serum

Fc – Fragment crystallizable region

FcRn – Neonatal Fc receptor

FOLFIRINOX – Folinic acid, fluorouracil, irinotecan hydrochloride and oxaliplatin

FPLC – Fast protein liquid chromatography

GNAS – Guanine nucleotide binding protein

SMAD4 – Mothers against decapentaplegic homolog 4

GoF – Gain-of-function

HER2 – Human epidermal growth factor receptor 2

HIV 1 – Human immunodeficiency virus type 1

HRP – Horseradish peroxidase

IHC – Immunohistochemistry

IPMN – Intraductal papillary mucinous neoplasm

iTLC – Instant thin layer chromatography

IWGAV – International working group on antibody validation

KPC – LSL-KrasG12D/+, LSL-Trp53R172H/+, Pdx-1-Cr

KRAS – Kristen rat sarcoma viral oncogene homolog

LKB1 – Liver kinase B1 or Serine/threonine kinase 11

mAb – Monoclonal antibody

MCN – Mucinous cystic neoplasm

MDCT – Multi-detector computed tomography

MDM2 – Mouse double minute 2 homolog

MES – 2-(N-morpholino)ethanesulfonic acid

MLH1 – MutL homolog 1

M-PER – Mammalian protein extraction reagent

MRI – Magnet resonance imaging

MTT – 3-(4,5-dimethylthiazol-2-yl)-2,5-diphenyl tetrazolium bromide

MUC1 – Mucin short variant S1

MUC5AC – Mucin 5AC, oligomeric mucus/gel-forming

MUC6 – Mucin 6, oligomeric mucus/gel-forming

MWCO – Molecular weight cut-off

NAD – Nicotinamide adenine dinucleotide

$NaHCO_3$ – Sodium bicarbonate

NET – Neuroendocrine tumours

NGS – Next generation sequencing

NHS – N-Hydroxysuccinimide

NSCLC – Non-small cell lung cancer

OCT – optimal cutting temperature compound

PanIN – Pancreatic intraepithelial neoplasia

PBS – Phosphate buffered saline

PBST – PBS + 0.1% Tween

PDAC – Pancreatic ductal adenocarcinoma

PDGFRb – Platelet derived growth factor receptor beta

PET – Positron emission tomography

PRSS1 – Serine protease 1

PVDF – Polyvinylidene fluoride

RIA – Radioimmunoassay

RIC – Radioimmunoconjugate

RNAi – RNA interference

ROS – Reactive oxygen species

RT ¬ Room temperature

SDS-PAGE – Sodium dodecyl sulfate polyacrylamide gel electrophoresis

SPAAC – Strain-promoted Azide - Alkyne Click Chemistry reaction

SPECT – Single photon computed tomography

SV40 – Simian virus 40

TAD – p53 transactivation domain

TAT – Transactivator of transcription

TBS – Tris-buffered saline

TET – p53 tetramerization domain

TP53 – Tumour protein 53

US FDA – United States Food and Drug Administration

VOI – Volume of interest

γH2AX Phosphorylated H2A histone family member X

1 Chapter 1 – Introduction

1.1 Pancreatic cancer

Pancreatic cancer refers to all forms of tumours that develop from the pancreas. These tumours arise when cells of the pancreas start to divide and proliferate abnormally affecting the normal function of the pancreas, such as glucose homeostasis and secretion of digestive enzymes. Pancreatic tumours often metastasise to organs such liver, lungs, peritoneum, and lymph nodes. Clinically, pancreatic cancer is used to refer to pancreatic ductal adenocarcinoma (PDAC), which is a notoriously aggressive and devastating tumour that arise from the pancreas ductal cells. PDAC accounts for over 90% of pancreatic cancer cases and is infamous for late diagnosis, resistant to standard therapies, poor prognosis and presents the lowest of 5-year survival rate among all solid cancers (Klein, 2019).

Globally, pancreatic cancer is ranked the tenth leading cause of cancer incidence and seventh leading cause of cancer mortality. In 2020, it accounted for a total of 495,773 new cases and 466,003 related deaths (Hu et al., 2021). Moreover, it is projected that by 2030, both the incidence and mortality will skyrocket by two-fold, and PDAC will become the second cause of cancer mortality (Orth et al., 2019). The incidence of pancreatic cancer varies across regions and populations. Europe and North America have the highest age-standardised rate incidence (ASR) of 7.7 and 7.6 per 100,000 people, respectively. Africa has the lowest ASR of approximately 2.2 per 100,000 people. PDAC cases are more common in men (5.5 per 100,000) compare to women (4.0 per 100,000). Exposure to risk factors and accessibility to better diagnostic modalities are the major contributing factors to the disparity in the incidences (Rawla et al., 2019). Pancreatic cancer 5-year survival rates have remained below 9% over the past 20 years. Europe and North America have the highest mortality rates of 7.5 and 6.5 per 100,000 while South-Eastern Asia and East Africa have the lowest rates of 2.1 and

1.4 per 100,000, respectively. The major cause of pancreatic cancer high mortality rate is that over 80% of pancreatic cancer patients are diagnosed with late-stage metastatic tumours that are non-resectable and resistant to standard therapies.

1.1.1 The pancreas anatomy and function

The pancreas is a 14-24 cm glandular organ located in the upper abdomen behind the stomach. It is surrounded by other major organs such as the liver, spleen, and small intestine. The anatomy of the pancreas depicts three major parts: the head, the body, and the tail **(Figure 1:1)**. The head and the body comprise the exocrine tissues of the pancreas and is composed of acinar, centroacinar and ductal cells. The exocrine pancreas function to secrete zymogens in response to cues emanating from the stomach and duodenum. These enzymes include trypsin, lipase, and amylase, which are involved in the breakdown of proteins, lipids, and carbohydrates, respectively (Sayed & Mukherjee, 2022).The pancreas duct system consists of the main, interlobular and the intralobular ducts. The main pancreatic duct drains the fluid produced by the exocrine cells into the duodenum.

The endocrine tissues of the pancreas are composed of the islets of Langerhans. The islets consist of four specialised endocrine cells, 30% α-cells, 60% β-cells, with the remainder 10% made up of δ-cells, γ-cells, and ε-cells (ghrelin-producing). These cells secrete energy homeostasis hormones directly into the blood, including glucagon (α-cells), insulin (β-cells) and somatostatin (δ-cells). γ-cells and ε-cells secrete pancreatic polypeptide and ghrelin, respectively (A-Kader & Ghishan, 2012).

1.1.2 Forms of pancreatic cancer

The pancreas is prone to develop two forms of tumours, exocrine and neuroendocrine. The most notorious cancer of the pancreas is the pancreatic ductal adenocarcinoma (PDAC) that

develop from the exocrine tissues (Hu et al., 2021). Other rare exocrine neoplasms include acinar cell carcinomas, adenosquamous carcinomas, colloid carcinomas and hepatoid carcinomas. Neuroendocrine tumours (NETs) are minor pancreatic malignancies and include insulinomas, glucagonomas, somatostatinomas and gastrinomas. Other diseases of pancreases include acute and chronic pancreatitis, cystic fibrosis, and diabetes mellitus (Haeberle & Esposito, 2019).

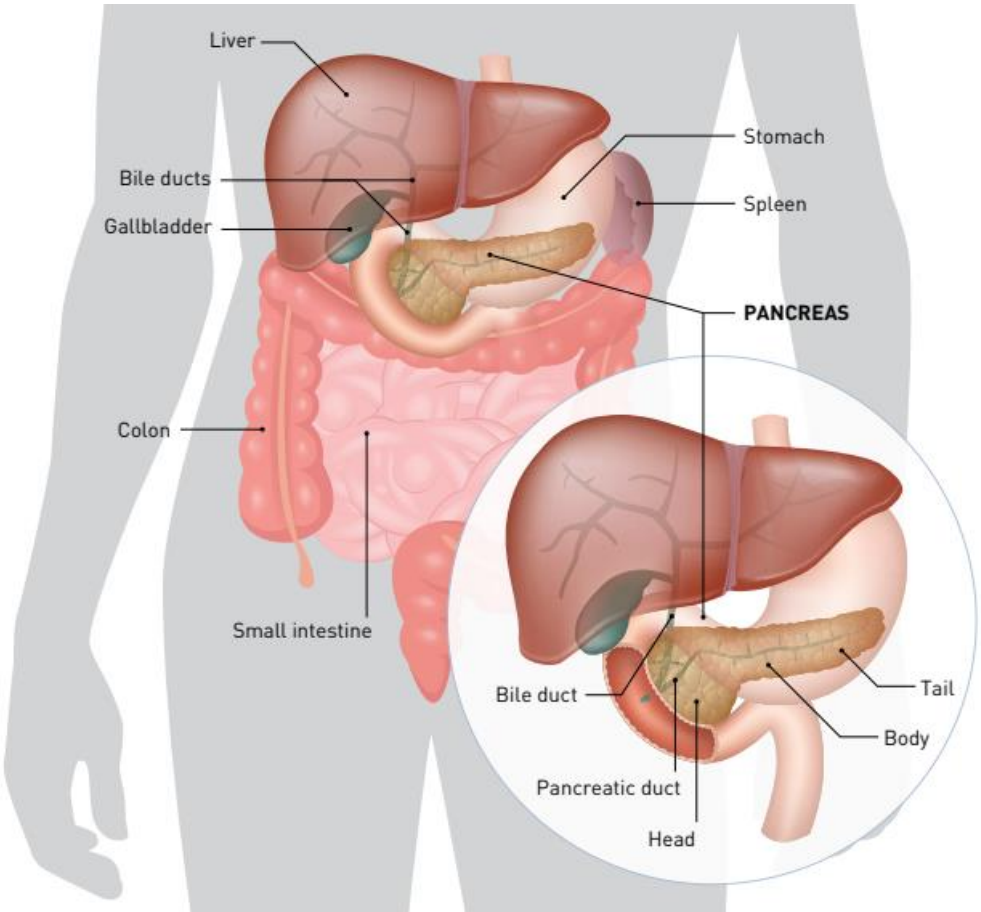


Figure 1:1) Anatomical location of the pancreas. The pancreas is located in the upper abdomen behind the stomach and is structurally divided into the head, body, and tail. It surrounded by major organs of the digestive system. PDAC develops from the head and the body of the pancreas while neuroendocrine tumours form at the tail. Image adapted from (Adel. Nelly, 2019)

1.1.3 Pancreatic ductal adenocarcinoma

PDAC is a highly ferocious malady presenting the worst prognosis and highest fatality rate among solid malignancies. PDAC's grim statistics are attributed to its aggressive asymptomatic progression resulting in majority of the patients diagnosed with inoperable metastatic tumours that are resistant to chemo/radiotherapies. Less than 20% of PDAC patients qualify for curative surgery, with an overall five-year survival rate of approximately 27%, and recurrence rate of up to 70% (Ratnayake et al., 2020). As such, tackling this aggressive tumour effectively calls for urgent development of novel (early) diagnostics and targeted therapies.

The genesis and progression of PDAC occurs through multiple genetic perturbations that transform the normal pancreas to non-invasive precursor lesions, that over time develop into invasive tumours. Mutations in KRAS, CDKN2A, TP53 and SMAD4 genes, telomere shortening, and epigenetic alteration are hallmarks of PDAC tumorigenesis (Cicenas et al., 2017). Histology and genetic studies characterised three main precursor lesions of PDAC: namely, pancreatic intraepithelial neoplasia (PanIN), intraductal papillary mucinous neoplasm (IPMN) and mucinous cystic neoplasm. PanIN lesion accounts for approximately 75% of all PDAC cases and are generally known as the canonical precursor lesions of PDAC (Hezel et al., 2006). The three precursor lesions are discussed in detail in the ensuing sections.

1.1.3.1 Pancreatic intraepithelial neoplasia (PanINs)

PanINs are small (<0.5 cm), non-invasive, flat, or papillary epithelial neoplasia, and usually arise from small intralobular pancreatic ducts. PanINs consist of cuboidal to columnar epithelial cells with varying amounts of mucins. Low-grade PanINs express MUC5AC and MUC6, while high-grade PanINs express MUC1 (Hruban et al., 2008). These lesions are graded

as low or high grade based on the degree of cytological and architectural atypia, and cumulative genetic alterations (**Figure 1:2**). Low-grade PanIN-1 and PanIN-2 lesions have flat or papillary lesions with basally located nuclei and mild-to-moderate cytological atypia. They are characterised by KRAS mutations and telomere shortening, which are the earliest pancreatic genomic alterations. Acquisition of other genomic abnormalities including loss of CDKN2A/p16 transform PanIN-1 into PanIN-2, characterised by nuclear polymorphism, crowding and hyperchromasia with frequent papillae. Both PanIN-1 and -2 are inconsequential lesions common in elderly people over the age of 50 years, hence not suitable for imaging for early diagnosis (N. Kalimuthu & Notta, 2016; Nagaraju & Ahmad, 2019).

PanIN-3 are high-grade invasive lesions hallmarked by loss of polarity, presence of mitotic figures, irregular stratification, and severe architectural and cytological atypia. Approximately 75% of these lesions harbour TP53 mutations, mostly missense, with evidence showing that several mutant p53 such as R175H, R248W and R273H are overexpressed (Koorstra et al., 2009a; Wang et al., 2016). It has been estimated that it takes up to 12 years for PanIN-3 to transform into invasive PDAC. Such a window provides an opportunity for screening high risk PDAC population using PET or SPECT as well as early therapeutic intervention (J. C. Knight et al., 2020; Peters et al., 2018).

1.1.3.2 Intraductal papillary mucinous neoplasms (IPMNs)

IPMNs account for 15-30% of total invasive PDAC tumours. They are cystic epithelial neoplasms with papillary projections and high mucin production. IPMNs occur predominantly in the main pancreatic duct and/or its branches and are grossly detectable on radiological imaging modalities because of their large size (approximately 1 cm) (Basturk et al., 2015). Like PanINs, they are categorised into low-grade and high-grade based on degree of dysplasia with

cumulative genetic alterations. KRAS and GNAS mutations occur in about 50% and 79% of IPMN respectively, while CDKN2A/p16, TP53 and SMAD4 mutations are noted in up to 40% of IPMNs (Amato et al., 2014).

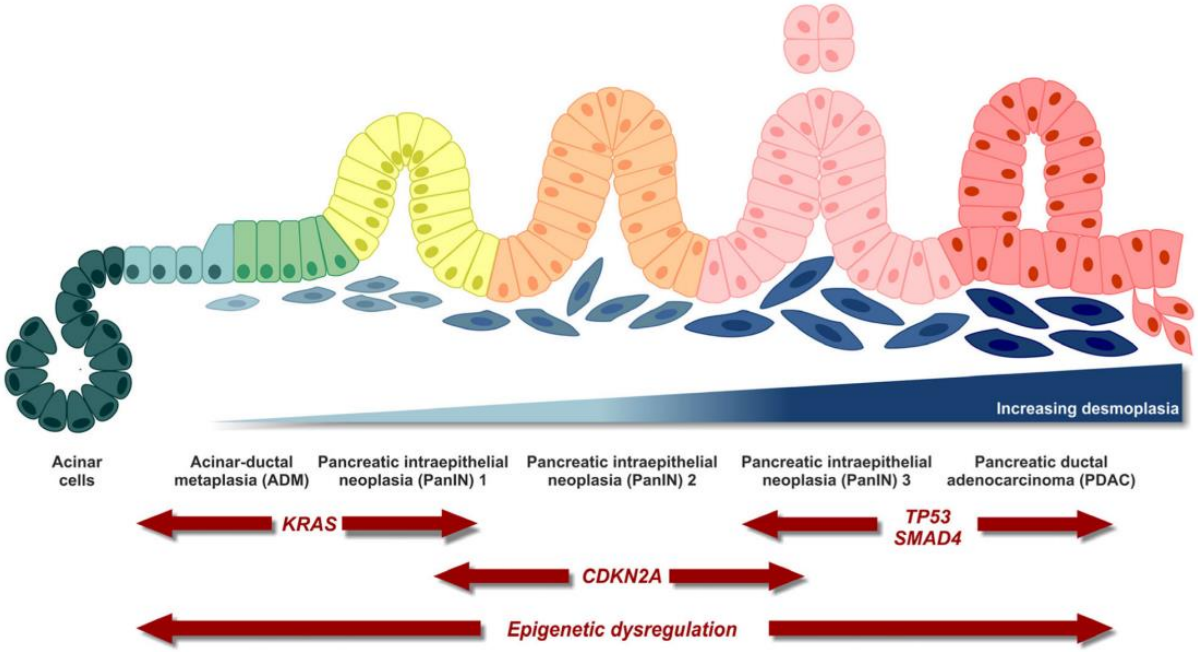


Figure 1:2) The Multistep histopathogenesis of PDAC. The pancreas exocrine cells tumorigenesis occurs during the acinar-ductal-metaplasia process and proceeds to PanIN lesions before development of PDAC. Image adapted from (Orth et al., 2019)

IPMNs can be categorised as main, branch, or mixed duct types based on their location or as gastric, intestinal, and pancreatobiliary types depending on the predominant cellular types (Machado et al., 2015). Main duct-type show dilation of the main pancreatic duct due to papillary epithelial proliferation and mucin production, which are usually absent in the branch duct-type. Mixed duct-type are involved in both the main and branch-ducts. Gastric-type IPMNS are characterised by blunted papillary architecture with columnar epithelial cell, mucin containing cytoplasm and basally located round oval nuclei. Intestinal types have villous shape papillary structure, basophilic cytoplasm, and cigar-shaped elongated nuclei. Pancreatobiliary types have branched papillary structure, amphophilic cytoplasm and round to oval nuclei.

The median age of IPMN carriers range from 60 to 66 years. They are more common in men than in women (ratio: 3/1.3 in Europe, 3/2.1 in the United States, and 3/1.8 in Asia) and arise most frequently in the proximal pancreatic head and the "uncinatus" process. IPMNs may require up to six years to become invasive (J. Y. Kim & Hong, 2018).

1.1.3.3 Mucinous cystic neoplasms (MCNs)

MCNs are cystic mucinous producing epithelial cells that usually arise in the distal part of the pancreas (body and/or tail) and account for up to 16% of the invasive PDAC. They are typically reported in perimenopausal women, with few cases described in men (Thompson et al., 1999). MCNs are histologically composed of an epithelial lining covered by tall columnar mucin-containing cells and non-mucinous flat or cuboidal epithelial cells. They also display underlying ovarian-type stroma components, which is a feature that differentiates them from IPMNs. Like IPMNs and PanINs, they are classified as low-grade and high-grade dysplasia, and have overlapping genetic alterations, including KRAS, TP53, SMAD4, and CDKN2A/p16 mutations (Hezel et al., 2006).

1.1.4 Risk factors

PDAC aetiology is linked to known demographic and environmental risk factors, with some few cases associated with autosomal dominant genetic conditions. These risk factors can be broadly grouped into two groups, namely, modifiable, and non-modifiable risk factors. The former ones include tobacco and alcohol use, chronic pancreatitis, obesity, and type-2 diabetes. Non-modifiable risk factors include old age, familial lineage with PDAC history and predisposed genetic factors due to autosomal dominant genetic conditions (Capasso et al., 2018).

Over 90% of PDAC cases are diagnosed in peoples aged over 55 years, with majority of the cases presenting in the 6th and 7th decade of life. A handful of PDAC among young population occur mainly due to underlying genetic conditions, with strong evidence in families with a positive history of PDAC and patients with BRCA 1 or BRCA 2 mutations. Chronic tobacco use accounts for about 35% of total PDAC cases, although this varies with age, gender, and country. The risk of developing PDAC increases by 75% among smokers compared to non-smokers. Following smoking cessation, this risk persists for a minimum of 10 years. Excessive alcohol consumption is also an established risk factor, with evidence suggesting that people who drink three or more drinks per day have a 1.22 to 1.36-fold increased risk of developing PDAC (Hu et al., 2021). Binge alcohol consumption is also responsible for approximately 90% of chronic pancreatitis cases, an established PDAC risk factor. Both type 1 and 2 diabetes have been associated with pancreatic cancer development, with higher risk observed in new-onset type 2 diabetes. Diabetes associated with acute or chronic pancreatitis, type 3c, has shown to confer a higher risk, with up to 30% of PDAC patients presenting its symptoms (Capasso et al., 2018).

It is well established that 10¬15% pancreatic cancer cases are of familial origin. Family members whose first- and second-degree relatives had pancreatic cancer have an 80% increased risk of developing it during their lifetime. Genetic alterations in specific genes have been shown to cause inherited genetic disorders that predispose people to developing PDAC, which accounts up to 10% of all cases. They include germline mutations of INK4a/ARF, BRCA2, and LKB1, MLH1 and PRSS1. Germline mutations in the cationic trypsinogen gene PRSS1 cause hereditary pancreatitis which results a 35-fold increased incidence of PDAC. Both BRCA1 and BRCA2 mutations increases people's susceptibility to PDAC development. The risk is even higher among females, who are twice likely to develop PDAC than males (Permuth-Wey & Egan,

2008). Other known risk factors include blood group, with non-O blood groups associated with a higher risk of PDAC. African Americans have a 50%-90% increased risk of PDAC compared to the Caucasian population. Increased risk has also been observed in patients infected with Helicobacter pylori (Capasso et al., 2018).

1.1.5 State of the art PDAC diagnosis and challenges

Early detection of PDAC remains a great challenge due to aggressive and asymptomatic pathogenesis. The majority of cases progress with nonspecific symptoms such as weight loss, jaundice, back pain, dyspepsia, and nausea. Only less than 20% of all PDAC patients have resectable tumours at the time of diagnosis. While high risk humans can be screened for the presence of invasive PanIN-3 lesions, the current imaging modalities lack the required sensitivity and specificity to detect lesions less than 1 cm (L. Zhang et al., 2018). Patients with suspicious symptoms are diagnosed with multi-detector computed tomography (MDCT) as the first line modality for diagnosis. MDCT has a sensitivity and specificity of 89% and 90% respectively, and exceptional tumour staging and predicting eligibility for surgery. However, it suffers from an inability to detect tumours less than 2 cm and unable to differentiate real pancreatic tumours from mass-forming pancreatitis (Brennan et al., 2007). Magnetic resonance imaging (MRI) is also used in the diagnosis and staging of PDAC tumours. MRI is better than MDCT is detecting lesions less than 2 cm and offer the advantage of differentiating pancreatic tumours from mass-forming pancreatitis. Its main challenge in PDAC diagnosis is limited sensitivity to detect lesions less than 1 cm. Endoscopic ultrasound with fine needle aspiration (EUS-FNA) is utilised as a second line diagnostic to identify smaller lesions where MDCT and MRI have failed with sensitivity of about 85% and specificity of 96%. However, EUS-FNA requirement of a biopsy tissues coupled to operator dependency limits its diagnostic reliability. A combination of PET ^{18}F-fluorodeoxyglucose ([^{18}F]FDG) with CT has demonstrated

superiority in N-staging and detecting liver metastasis. However, FDG-PET suffers from an inability to differentiate between mass-forming pancreatitis and pancreatic cancer and is unreliable in diabetic patients (Horvat et al., 2018; Strobel & Büchler, 2013).

There are ongoing efforts to develop novel PET imaging agents for early diagnosis of PDAC. The fibroblast activating protein (FAP) is highly expressed in cancer associated fibroblasts, the major component of PDAC stroma. FAP has been targeted by its inhibitor FAPI, for both diagnosis and treatment of PDAC (Mori et al., 2023). The PET imaging agent Gallium 68 (^{68}Ga)–labelled FAPI (FAPI) has made notable progress in clinical imaging and tumour staging of PDAC demonstrating superior performance in metastatic lesions detection and tumour stating compared to standard care imaging (R€ Ohrich et al., 2021). Compared to FDG PET,FAPI PET has better detection threshold of smaller lesions and show low uptake in organs such as brain, liver, head and neck mucosa and liver where background uptake of FDG PET is very high. However, FAPI PET has limited specificity in regions with high FAP expression including wounds, active inflammation, and high fibroblast activity in endometrium (Luo et al., 2021; Moradi & Iagaru, 2020). FAPI PET is not currently approved for clinical use but is likely to gain FDA approval within this decade due to its promising clinical trial results. Recently, CEACAM6, a highly abundant cell surface adhesion receptor that is overexpressed in primary and metastatic classical PDAC subtypes has become a target for PDAC imaging (Pandey et al., 2019). The Tuveson lab at Cold Springs Harbour Laboratory has developed Zirconium-89 labelled monoclonal antibodies known as TOBi-bodies targeting CEACAM-6 abnormal expression in PDAC. The PET TOBi-bodies enabled detection of mice incipient human organoid-derived PDAC tumours that were undetectable by palpation or high-resolution ultrasound imaging techniques (Oni et al., 2020). TOBi-bodies are promising PET imaging agents for PDAC diagnosis and are still under preclinical investigation.

Currently, there is no reliable biomarker for early PDAC screening. While CA19.9 is elevated in about 80% of PDAC patients it is suboptimal for early detection, due to its low positive predictive value of 0.5-0.9%, given that it is also expressed in other maladies including jaundice, hepatobiliary disease, chronic pancreatitis, and other cancers. More pointedly, approximately 6% of the white population and 20% of the black population do not express CA19-9. Thus, its reliability as diagnostic biomarker can result in both false positives and negatives. However, CA19-9 is useful as a prognostic marker for monitoring recurrence after resection with a sensitivity and specificity of 80% and 88% respectively (E. Poruk et al., 2013; Marrelli et al., 2009).

1.1.6 PDAC treatment

PDAC display extensive genetic heterogeneity and multiple aberrant pathways which make the development of targeted therapies very challenging. Tumours are characterised by dense desmoplastic tissues consisting of extracellular matrix (ECM), cancer-associated fibroblasts, muscle fibroblasts, immune cells, and pancreatic stellate cells. The dense stromal networks create a rigid barrier that diminish vascularisation and attenuate penetration of drugs such as gemcitabine, contributing to the high level of therapeutic resistance (Orth et al., 2019; Ratnayake et al., 2020).

The less than 20% of patients that present with resectable tumor receive surgery and neoadjuvant therapy as the main form of treatment. This group mainly receive gemcitabine and radiotherapy (54 Gy) prior to operation to remove the shrunken tumours. Over 80% of the remaining PDAC patients usually have non-resectable malignancies and are subjected to systemic chemotherapy as first-line treatment. Nucleoside analogues such as gemcitabine and capecitabine, or the pyrimidine analogue 5-fluorouracil (5-FU) are used in monotherapy

settings or in combination with radiotherapy. A poly-chemotherapeutic regimen composed of folinic acid, 5-FU, irinotecan, and oxaliplatin (FOLFIRINOX), is the current standard treatment for PDAC patients with metastatic disease with an overall and progression-free survival rates of 11.1 and 6.4 months respectively. FOLFIRINOX is however associated with increased toxicities including grade 3 or 4 thrombocytopenia, neutropenia, febrile neutropenia, and diarrhoea, or grade 2 alopecia, which limit administration to elderly people and patients with poor performance status (Adel. Nelly, 2019; Orth et al., 2019).

Since only less than 20% of PDAC patients can have curative surgery, and the standard of care chemotherapies remain ineffective, efforts are being geared towards targeted therapies and immunotherapies. PDAC lack suitable biomarkers for targeted therapeutics development and patients show resistance to immunotherapies that work favourably for other cancers. Several efforts are in the pipeline to target frequently mutated genes, abnormal signalling pathways and components of the PDAC microenvironment. Immune checkpoint inhibitors including therapeutic antibodies targeting cytotoxic T-lymphocyte-associated protein 4 (CTLA-4) or programmed cell death protein 1 (PD-1) have been used to treat PDAC patients benefiting up to 2% of patients. Only PDAC patients with microsatellite instability benefited from the two immunotherapies. The strong PDAC immunosuppressive and desmoplastic microenvironment accounts to the low successes of immunotherapies among patients (Orth et al., 2019). A universal feature of PDAC tumours is the dense stroma composed of both cellular and acellular materials. Hyaluronan, a major component of the pancreatic stroma has been targeted for stromal depletion using a recombinant human hyaluronidase 20 (rHuPH20). rHUPH20 in combination with gemcitabine and nab-paclitaxel resulted in promising phase I and II trials results and is currently under phase III trial no NCT02715804 in order to fully understand its clinical performance (Hingorani et al., 2018).

KRAS mutations are found in more than 90% of PDAC patients, with the most prevalent mutation G12D occurring in around 36% among PDAC patients. Efforts have been made to develop small molecules inhibiting this mutant. The most promising one is the $KRAS^{G12D}$ inhibitor MRTX1133 that has demonstrated enhanced anti-tumour activity and selectivity at preclinical stage and is lined up for clinical trials in PDAC patients (Hallin et al., 2022). The TGFβ is strongly expressed in PDAC, and its dysregulation is common feature enhancing PDAC progression and aggressiveness. TGFβ signalling has been targeted for inhibition using small molecules such as LY-210976 and Vactosertib (TEW-7197. A combination of either of the two inhibitors with gemcitabine or nal-IRI plus 5-Fluorouracil/Leucovorin, respectively, have demonstrated promising anti-tumours results in orthotopic pancreatic cancer mouse models are currently still under investigation (Hong et al., 2020).

Effective PDAC treatment remain a jigsaw puzzle to clinicians and scientists. Better understanding of molecular drivers underlying PDAC pathogenesis would pave the way for discovery of sensitive/specific biomarkers for targeted treatments development. A combination of emerging therapies with current treatment modalities could also help to improve their current grim clinical outlook of PDAC patients.

1.2 The tumour suppressor protein p53

1.2.1 TP53 gene

The TP53 gene, located on chromosome 17p13.1. encodes a 53 kDa protein known as p53 that is universally dubbed as the 'guardian of the genome.' p53 function is critical in preserving the integrity of the genome and preventing malignant transformation. p53 activates transcription of a plethora of genes involved in cell-cycle arrest, DNA damage repair, senescence, apoptosis, autophagy, and anti-angiogenesis (Riley et al., 2008a, 2008b; X. Zhou

et al., 2019). It is also involved in modulation of mammalian cell differentiation and proliferation (A. K. Jain & Barton, 2018; Liu & Xu, 2011). p53 role as a tumour suppressor protein was discovered following a long controversial scientific detour. In 1979, Linzer and Levine discovered a 53-54 kDa protein during the study of SV40 aetiology in mice and hamsters bearing SV40-induced tumours. The 53-54 kDa protein was found bound to SV40 large T antigens, in immunoprecipitation assays using sera harvested from the tumour models in question (Levine & Oren, 2009; Linzer & Levine, 1979). Almost a decade later, Oren and colleagues found that co-transfection of p53 cDNA with ras oncogene into rat embryo fibroblasts enhanced malignant transformation (Michalovitz et al., 1990). This led to a conclusion that p53 was an oncogene. However, it soon became apparent that the p53 cDNA that was used in these experiments came from cancerous cells and had a point mutation. Further experiments using a p53 from normal cells suppressed transformed fibroblast cells, a eureka moment that revealed p53 as tumour suppressor protein and not an oncogene. p53 is the master tumour suppressor protein in humans and its mutations lead to tumorigenesis events. Mutant p53 is found in over 50% of human malignancies (Levine & Oren, 2009; X. Zhou et al., 2019).

1.2.2 p53 structure and regulation

p53 is a 393 amino acid (aa) protein with a complex structure consisting of both well-organised and disorderly domains. The former includes the central DNA binding domain (DBD) (aa 94-292) and the tetramerization domain (OD) (aa 325-356). At the N-terminal is the natively unfolded acidic transactivation domain (TAD) (aa 1-62) and the proline-rich region (PRR) (aa 63-94), while at the extreme C terminal is the lysine rich negative autoregulatory domain (CTD) (**Figure 1:3**). The TAD domain provides a binding surface for several p53 binding partners including its main negative modulator MDM2, coactivators such p300 and CPB and

other members of transcription initiation complex. TAD is further subdivided into TAD 1 (aa 1-40) and TAD 2 (aa 40-62). The PRR domain structurally links the TAD domain to the DBD. It is composed of five SH3 domain-binding motifs (PXXP), that participates in p53-mediated antiproliferation activity (Baptiste et al., 2002; Joerger & Fersht, 2007, 2008; Taniguchi & Kawakami, 2012a).

The DBD region consists of an immunoglobulin-like β-sandwich that provides a binding surface for p53 downstream target genes. This binding surface consists of two motifs: the loop helix motif (L1, β-strands S2 and S2' and parts of the extended β-strand S10, and the C-terminal helix) and other two large loops (L1 and L2). The former functions by interacting with the major groove of the consensus DNA sequences while loop L1 and L2 docks to the minor groove. The two loops, L1 and L2 are stabilised by a zinc ion that is tetrahedrally coordinated by three cysteines and one histidine side chain (Cys-176, His-179, Cys-238 and Cys-242). The loss of zinc leads to destabilization and aggregation (Butler & Loh, 2003; Joerger & Fersht, 2008). The p53 OD region consists of short β-strand and α-helix connected by a glycine residue. This domain function by regulating the oligomerization state of the protein. The negative regulatory domain binds to DNA in a non-specific manner. The lysine-rich region is believed to regulate the sequence-specific DNA binding and harbour posttranslational modifications sites including acetylation, ubiquitination, and sumoylation, among others (Joerger & Fersht, 2010).

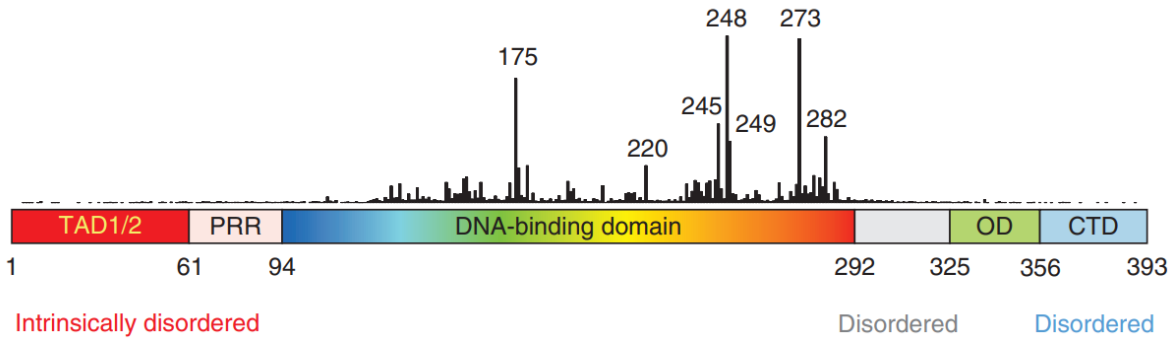


Figure 1:3) The domain structure of human p53. The protein has five major domains: the amino-terminal transactivation domain (TAD and TAT 2), proline rich region (PRR), DNA binding domain (DBD), Tetramerisation domain (OD) and the extreme carboxyl terminus (CDT). The vertical bars indicate amino acids relative mutation frequency in human cancer. The image was adapted from (Joerger & Fersht, 2010).

High levels of p53 in healthy cells can trigger senescence and apoptosis that lead to premature ageing of the organism. Consequently, the p53 levels are tightly regulated and have a very short half-life under a normal physiological state of the cells. p53 responds to a plethora of genomic stresses through a series of posttranslational modifications, that occur via positive and negative autoregulatory feedback loops resulting in the upregulation of protein levels. The major cellular event that takes place during the activation of p53 involves the disassociation from its main negative regulator the MDM2/MDMX complex (**Figure 1:4**). MDM2 is an E3 ubiquitin ligase that directly interacts with p53 at the N-terminal tagging ubiquitin moieties on the C-terminal end. This facilitates the nuclear export of p53 protein to the cytoplasm and subsequent proteasomal degradation. The constant interaction of p53 protein with the MDMX complex is responsible for maintaining low p53 levels in normal healthy cells. In the event of cellular insults detrimental to the integrity of the genome, the p53/MDMX association is inhibited through several posttranslational modifications, including phosphorylation and acetylation at specific amino acids in p53 polypeptide (Joerger & Fersht, 2010). The most predominant of the p53 modifications involves the phosphorylation at

serine-15 by kinases such as DNA-PK, ATM and ATR. This prohibits p53 ubiquitination and facilitates its accumulation in the nucleus and ensuing activation of downstream transcriptional activity. The second way by which p53 is shielded from MDM2 is through the association of MDM2 with its negative inhibitor 'alternative reading frame' (ARF). The binding of ARF to MDM2 triggers transient disruption of MDM2 ubiquitination and the subsequent proteasomal degradation of p53. However, cells lacking the ARF gene are still able to induce genotoxic stress-mediated p53 accumulation and activation, implying that the former pathway is the most crucial. The acetylation of p53 plays an important role in promoting specific binding of p53 to consensus DNA. Transcriptional coactivators such as CBP/p300 and PCAF acetylate p53 at lysine-373 and lysine-382, and lysine-320, respectively (Harris & Levine, 2005).

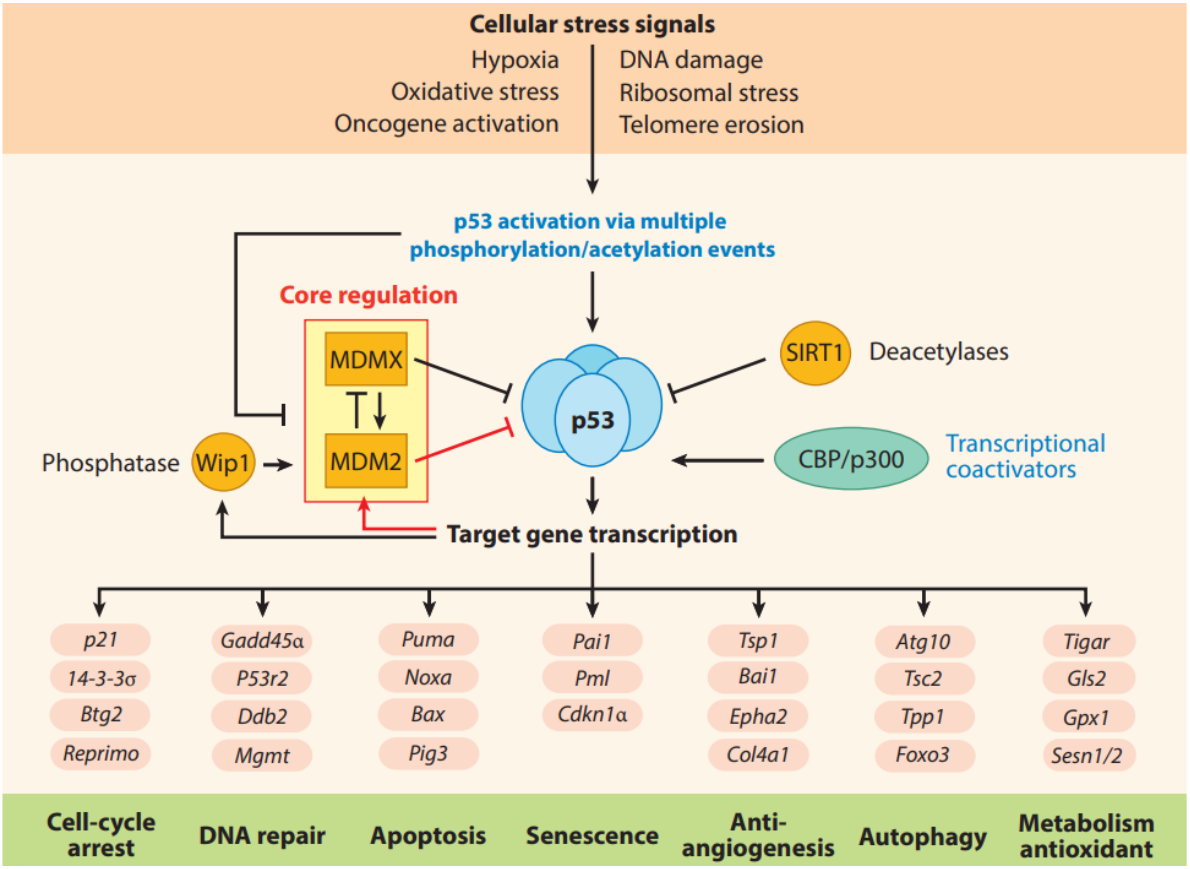


Figure 1:4) The p53 regulation pathway and function. In unstressed cells, p53 protein levels are constantly degraded via a negative feedback loop by MDMX/MDM2 complex and SIRT1. The p53 is activated upon cellular stress through multiple phosphorylation and acetylation events leading to accumulation in the nucleus and subsequent transactivation of downstream target gene involved in cell-cycle arrest, DNA repair, senescence, and apoptosis. The image was adapted from (Joerger & Fersht, 2016).

1.2.3 p53 function

Functionally active p53 drives transcription of an array of genes involved in anti-tumorigenesis molecular events including cell cycle arrest, cellular senescence, and apoptosis. p53 regulation of cell cycle arrest is achieved by indirect transcriptional repression of several genes involved in the G1-to-S, the G2-to-mitosis transitions and spindle assembly checkpoints upon p53-mediated upregulation of p21/CDKN1A. Among the downregulated genes can be counted cyclin A, cyclin B1, cyclin-dependent kinase-1 and polo-like kinase 1(PLK1). p53-induced cell cycle arrest occurs through the p53–p21–DREAM–E2F/CHR pathway, where it directly binds to p21 leading to its transcriptional activation and upregulation. The activated p21 subsequently inhibits CDK complexes such as cyclin E/A-CDK2 and cyclin D-CDK4/6, leading to hypophosphorylation of pRB-related proteins p107 and p130. The p107 and p130 interact with other proteins such as the MuvB core complex, E2F4 and E2F5 to form the DREAM complex. The final step entails the binding of the DREAM complex to the E2F and CHR (cell cycle genes homology region) promoter sites. This represses the expression of cell cycle coordinating genes, providing an opportunity for the repair of damaged DNA (Engeland, 2017).

Another major function of p53 is promotion of cell death in the event the damaged DNA is irreparable. This insures against transfer of damaged genetic material to daughter cells and potential tumorigenesis. p53 mainly triggers cell death by directly activating members of the

Bcl-2 family (Bax) and BH3-only proteins (Puma, Noxa and Bid), to drive the intrinsic apoptotic pathway. The activated BH3-only proteins bind and inhibit the pro-survival BCL-2 proteins leading to release and activation of pro-apoptotic BCL-2 members such as Bax and Bak, which cause mitochondrial outer membrane permeabilization and release of caspase-9 that initiates the death of damaged cells. The choice between the two p53-apoptotic pathways is depended upon several factors, including the type of stress signal, exposure time to the genomic insult, and levels of p53 among others (Aubrey et al., 2017; J. Chen, 2016). By promoting apoptosis, p53 function to ensure that any cell carrying irreparable genomic damage is eliminated thus preventing any tumorigenic events.

In addition, p53 induces the activation of other anti-malignant processes such as DNA damage repair, anti-angiogenesis, autophagy, and metabolic regulation. The exact mechanisms through which p53 regulates these processes remain to be fully elucidated, albeit they all function to prevent malignant transformation (Joerger & Fersht, 2016; Mary, 2021).

1.2.4 p53 mutations in human cancers

The prevalence of p53 mutations varies both at the cellular and tumour level and among cancer patients. Cancers with most frequent TP53 mutations include ovarian serous carcinoma (96%), small cell lung cancer (85%) and pancreatic cancer (75%) (Blandino & di Agostino, 2018). Overall, p53 mutations represent the most frequent gene abrogation in human cancers. Next-generation sequencing (NGS) of human tumours revealed that p53 is inactivated through somatic and germline mutations. Somatic mutations occur in more than 50% of human cancers with germline mutations present in up to 17% of all familial cancers. Unlike other tumour suppressor proteins that are inactivated through truncated mutations, p53 mutations mainly occur through single amino acid substitutions that lead to the

expression of full length, but otherwise aberrant protein. The penetrance of different p53 mutations includes 75% missense, 9% frameshift insertions and deletions, 5% silent mutations among other infrequent mutations (Muller & Vousden, 2014). Approximately 80% of the missense mutations are clustered between exons 4 and 9 of the p53 gene.

p53 mutations abrogate wild type function by either inducing conformational changes (structural mutants e.g., R175H, G245S, R249S, and R282W,) or disrupting the ability of the DBD domain to interact with its consensus sequences (contact mutants e.g., R248W and R273W). These distortions incapacitate p53's ability to transactivate or repress its downstream targets (Blandino & di Agostino, 2018; Perri et al., 2016). Mutant p53 is often stabilised through interaction with type 1 phosphatidylinositol phosphate kinases (PIPKIα or PIP5K1A) promoting its association with small heat shock proteins such as HSPB1 and HSPB5. This causes mutant p53 to accumulate in the nucleus of cancer cells (Choi S., et al 2019; H. Li et al., 2019). Alexandrova and colleagues demonstrated that osteosarcoma and fibrosarcoma tumour mouse models with a high frequency of p53 loss of heterozygosity (LOH) are more stable and show increased oncogenic potential. The stabilised mutants acquire gain-of-function (GoF) capability promoting cancer invasiveness, metastatic potential, and resistance to therapies (Alexandrova et al., 2017). In addition, mutant p53 exert dominant-negative effect (DNE) by forming mixed tetramers with wild type p53, masking their tumour suppressive function. DNE also occur when mutant p53 hetero-oligomerises with its family members p63 and p73 incapacitating their tumour killing activities (H. Li et al., 2019). Overall, p53 mutations in human cancers have been proved to be essential for cancer development and aggressiveness conferring poor prognosis and dismissal survival rates among cancer patients.

1.2.5 p53 aberrance in pancreatic ductal adenocarcinoma

p53 alterations in PDAC are majorly composed of somatic mutations with a few cases presenting germline mutations. Germline mutations of p53 lead to the Li Fraumeni syndrome, a rare devastating condition that condemn people to develop aggressive cancers including sarcomas, leukaemia, and pancreatic cancer (Peters et al., 2016). p53 somatic mutations appear to contribute to malignant progression rather than initiation. The majority of p53 alterations are found in the late-stage invasive lesions and PDAC. The selection pressure from accumulating DNA damage events, reactive oxygen species (ROS) and telomere erosions contributes to p53 inactivation. While p53 mutation occur in majority of PDAC patients, chronic pancreatitis patients have very few p53 abnormalities, or even lack them. Several studies have compared the frequency of gene alterations in pancreatic cancer and chronic pancreatitis. Casey and colleagues assayed for p53 mutations in 24 pancreatic cancer patients and 8 chronic pancreatitis patients. Eight of twenty-four (33%) cancer samples were mutated for the p53 gene while none of the chronic pancreatitis patients had p53 mutations (Casey et al., 1993). In two other experiments, 4/167 and 2/23 chronic pancreatitis patients confirmed positive for p53 mutations (Talar-Wojnarowska et al., 2006). The low frequency of p53 mutations in chronic pancreatitis patients can be used as a molecular imaging differential marker, where CT and MRI fail to discern between focal mass-forming pancreatitis from real pancreatic tumours.

PDAC patients overexpressing mutant p53 show increased metastasis and chemo/radiotherapy resistance. In one study, mutant p53 was shown to induce overexpression of platelet-derived growth factor receptor b (PDGFRb) and enhance pancreatic cancer metastasis through inhibition of p73/NF-Y complex that represses PDGFRb. The repression of p73 function occurs through a mutant p53 dominant negative effect, where

it forms inactive hetero- tetramers with p73 preventing it from forming PDGFRb inhibitory complex p73/NF-Y (Weissmueller et al., 2014). Mutant p53 has also been shown to stimulate PDAC cells resistance to gemcitabine treatment. Stabilised mutant p53 induced the expression of its target genes CdK1 and CCNB1, thereby causing gemcitabine resistance in PDAC cell lines Panc1 (R273H), PaCa44 (C176S) and MiaPaCa2 (R248W) (Fiorini et al., 2015). However, a combination of gemcitabine with mutant p53 reactivating molecules, CP-31398 and RITA inhibited PDAC cell lines proliferation, confirming the chemoresistance potential of mutant p53. The one major limitation of the above studies is that they only used a few of the known p53 hotspot mutants. Since p53 mutations are heterogenous, a broad panel of p53 mutant cell lines should be included in similar experiments in order to provide clinically meaning and instructive conclusions.

The high penetrance of p53 mutations and/or overexpression in both invasive PanIN-3 lesions and PDAC, and its implications in PDAC poor prognosis presents an opportunity to develop imaging agents for early diagnosis and prognosis evaluation.

1.3 Molecular imaging

Cancer imaging is very useful for the detection of the precise location of tumours, patient treatment stratification and assessing response to treatments. A variety of techniques are employed to investigate the presence of cancers in the body, including those that give anatomical information or those that help to assess the molecular and biochemical nature of the cancerous tissues. Anatomical imaging modalities include MRI, CT and (E)US that provide tissue alteration and morphological information enabling the pathologist to diagnose the disease status. These techniques have proved indispensable in tumour identification and staging aiding clinicians to make informed treatment decisions. Functional imaging modalities

include PET, SPECT, and optical imaging techniques such as fluorescence imaging. They utilise targeted imaging agents to assess biochemical processes inside intact organisms such as protein-protein interactions, metabolic processes, and gene expression patterns. PET and SPECT are exquisitely sensitive as they can investigate molecular targets in picomolar concentrations. Since molecular alterations such as gene mutations and/or abnormal expression initiate disease development before manifestation of physical and anatomical symptoms, imaging such processes can aid in early diagnosis of maladies such as cancer. The use of functional imaging modalities offer advantage in disease screening compared the anatomical imaging counterparts (James & Gambhir, 2012; Pysz et al., 2010). In addition, molecular diagnostics enable patient treatment stratification and therapeutic response assessment which lead to better decision making and changing of strategy during treatment.

1.3.1 SPECT imaging

SPECT is a radionuclide molecular imaging technique that detects the spatial concentration of radiopharmaceuticals inside living organisms to diagnose a pathological condition or biological process based on the emission of gamma rays. SPECT was first described in 1963, 10 years after the invention of the gamma camera. However, the first clinical application took stage in the 1970s and became widespread in the 1980s. SPECT utilises the gamma camera that rotates around the subject to capture gamma rays and reconstruct tomographic images. A scintillation camera consists of a lead collimator which allows photons travelling in different directions to pass through to a NaI (Tl) crystal that converts the energy of the γ-ray photons to lower-energy photons which are in turn converted to electric signals by photomultiplier tubes (PMTs), or, in more modern versions, semi-conductor-based light detectors. The signal from the PMTs is processed by electronic circuitry to provide information of photon interaction with the crystal (James & Gambhir, 2012). SPECT utilises radionuclides that emit

γ-ray photons such as [^{99m}Tc] ($t_{1/2}$ = 6 h), [^{123}I] ($t_{1/2}$ = 13.3 h), and [^{111}In] ($t_{1/2}$ = 2.8 days) to obtain images from the subject. The radionuclides are usually bound to imaging vectors such as antibodies or small molecules (Khalil et al., 2011). The imaging agent is administered intravenously into the subject to reach the relevant target as well as clear from the blood and non-target tissues. The images are then acquired providing information of the three-dimensional distribution and concentration of the radionuclide (**Figure 1:5**), as a proxy for the targeting vector, as a proxy for the target epitope's distribution and concentration.

The main difference between PET and SPECT is that PET cameras detect radionuclides that emit positrons such as [^{18}F], [^{89}Zr] or [^{64}Cu], followed by emission of gamma rays resulting from annihilation between the emitted positron and electron. Some examples of clinical SPECT imaging agents that target molecular processes include the radiolabelled small molecule [^{99m}Tc]TRODAT-1 for dopamine transporter (DAT) imaging, peptide [^{111}In]-DTPA-octreotide for imaging the somatostatin receptor (423), and [^{99m}Tc]-Annexin V for imaging apoptosis.

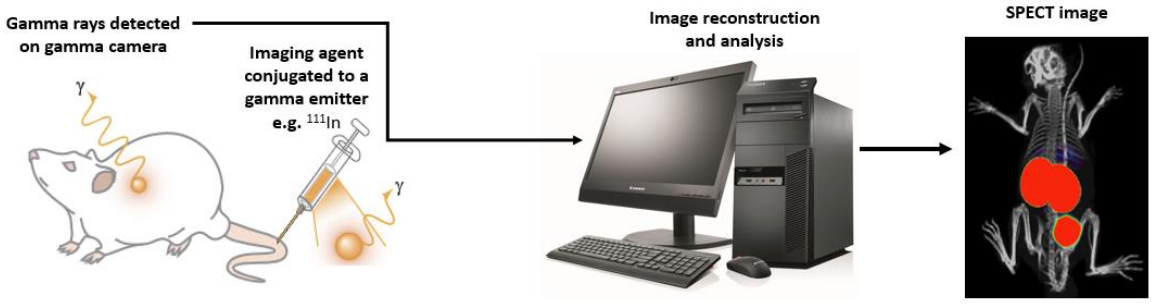


Figure 1:5) Illustration of SPECT imaging of mouse. A targeting vector such as a monoclonal antibody or peptide is radiolabelled with a gamma emitting radionuclide such as indium-111. The radiolabelled imaging agent is injected into the mice and allowed to engage with its target. Gamma photons emitted by the radionuclide are detected using a SPECT camera and the three-dimensional spatial distribution of the radiotracer is used to reconstruct the images. The image was adapted from (James & Gambhir, 2012).

In the laboratory, a miniaturized small animal SPECT is employed in imaging mice and rats during preclinical studies. Preclinical SPECT has better spatial resolution of 0.25 mm compared to preclinical PET with 1 mm, and a far inferior spatial resolution of 8–10 mm, compared with clinical PET's 5–7 mm, making PET to be the mostly in the clinic for cancer diagnosis. Small animal SPECT scanners have been widely utilized in imaging the biodistribution of radiotracers in mice (James & Gambhir, 2012). The Cornelissen group at Oxford have employed this imaging technique to visualise and quantify several cancer biomarkers including claudin-4, γH2AX, and ICAM-1 (Cornelissen et al., 2011; J. C. Knight et al., 2017). The use of µSPECT scanners in preclinical studies holds great value towards the discovery of new molecular imaging agents and precision medicines.

1.3.2 Molecular imaging agents

Molecular imaging agents are the molecular detectives that travels across the body seeking their target of interest. A molecular imaging agent is composed of a targeting vector (e.g., peptide, small molecule, or antibody) and a signalling molecule such as radioisotope or fluorescent molecules. The molecular imaging agents must be able to timely reach its target, clear from background regions and provide a contrasting information between the region of interest and non-target regions. To be able to successfully image the subject, the imaging agent must possess certain characteristics. They include 1) high target to non-target ratio, 2) high selectivity for the target of interest, 3) good safety profile, 4) suitable pharmacokinetics, 5) excellent *in vivo* stability and 6) cost-effective synthesis (James & Gambhir, 2012).

PET and SPECT imaging use radionuclides conjugated to targeting vectors as imaging agents. The most utilised vectors for radionuclide imaging include monoclonal antibodies, small

molecules, and peptides. For the purpose of this study, I will focus on monoclonal antibodies and peptides.

1.3.2.1 Monoclonal antibodies

Monoclonal antibodies are 150 kDa, Y-shaped glycoproteins produced by one clone of B lymphocytes. They form part of the adaptive immune system and act by binding to specific antigens and directing T-killer cells to destroy targets. The Y-shaped structure of the antibody comprises of four polypeptide chains including two pairs of identical heavy (50 kDa) and light chains (25 kDa), connected by several disulphide bonds. These chains form three functional domains including two antigen binding domains (Fabs) responsible for target engagement and a single fragment crystallisable (Fc) domain, which interacts with the host immune system (**Figure 1:6**) (Rodrigo et al., 2015).

In the lab, monoclonal antibodies are produced via immunisation of animals such as mice or rabbits with specific antigens stimulating the secretion of antibodies in the serum. The antibody producing B-cells are isolated and fused with immortal myeloma cells to form hybridoma cells that secrete antibodies when cultured in the lab. The large-scale production of monoclonal antibodies via hybridoma technology was first described by Kohler and Milstein in 1975 (Köhler & Milstein, 1975; Mitra & Tomar, 2021). The use of hybridoma technology has enabled researchers to generate a plethora of different antibodies for various applications including both diagnosis and treatment of maladies. *In vitro* assays such as Western blot, ELISA, flow cytometry, immunocytochemistry, and immunohistochemistry employ antibodies to detect antigens. Monoclonal antibodies are currently the cornerstone of cancer diagnosis and treatment with approximately 30 therapeutic antibodies approved by the US FDA for treatment of cancer patients as of December 2019 (Lu et al., 2020).

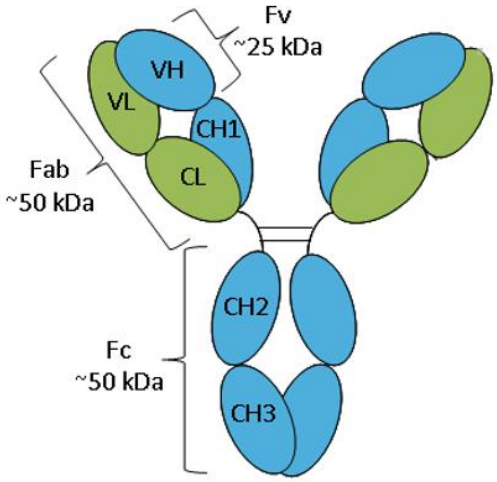


Figure 1:6) The basic structure of a mAb and its fragmented domains. A monoclonal antibody is composed of two 50 kDa heavy chains and two 25 kDa light chains linked with disulphide bonds in the hinge region. The image was adapted from (Rodrigo et al., 2015).

Because of their high affinity and specificity, monoclonal antibodies can be conjugated to signal emitting molecules such as fluorophores or radioisotopes and employed to image target epitopes of interest for disease diagnosis. However, monoclonal antibodies are associated with several drawbacks that impede their use to image patients. Firstly, they experience a prolonged serum half-life as a result of interaction with the neonatal Fc receptor, FcRn, resulting in an average half-life of several weeks. While this is ideal for enhanced target site accumulation and interaction, the long-blood circulation result in high background signal that lowers that image contrast. Also, the long half-life cause patients to wait for several days before imaging which can reduce screening compliance. Furthermore, intact antibodies often result in high liver uptake due to interaction of the Fc portion with hepatocyte receptors. This reduces the imaging sensitivity for detecting liver metastases (Rath et al., 2015). Lastly, the large size of whole antibodies (150 kDa) and its hydrophilic nature limits intracellular targeting. With approximately 30% of cancer biomarkers expressed and elevated inside the cells, unmodified antibodies cannot be used to for imaging intracellular targets. These limitations can be overcome using antibody fragments that have faster pharmacokinetics

compared to native antibodies. Several antibody-derived products with different size and improved bio-distribution and serum half-life have been developed, including F(ab')2 fragments, scFv, affibodies and nanobodies (Rodrigo et al., 2015). These antibody fragments have been employed as imaging agents for PET and SPECT imaging of cancer biomarkers such as HER2 and PSMA (Altunay et al., 2021; Knowles et al., 2014).

The conjugation of cell penetrating peptides with a nuclear localisation sequence to the native monoclonal antibody facilitate cellular entry and delivery into the cytoplasm and the nucleus. Several cell penetrating peptides have been employed to aid in intracellular delivery of IgG including HIV-1 TAT peptide obtained from the transactivator of transcription of human immunodeficiency virus - (HIV-1). Monoclonal antibodies conjugated with TAT have been used to image several intracellular targets such as γH2AX and ATM (J. Knight et al., 2015; Koren et al., 2011).

The use of monoclonal antibodies in cancer imaging continue to expand with increasing biomarker discovery and improvement of the quality of commercially available antibodies. As such, monoclonal antibodies will remain important imaging agents in both research and clinical application.

1.3.2.2 Peptides

Small peptides (5-50 amino acids) are alternatives to antibodies as imaging agents. Peptides offer advantages such as rapid target accumulation and quick elimination from the blood and non-target tissues producing high imaging contrast within hours. They also possess high binding affinities and specificities and are less costly to produce compared to small molecules and antibodies. In addition, their simple structure makes them more amenable to radiolabelling compared to MAbs (Fani et al., 2012a; Sun et al., 2017).

Several peptides have been radiolabelled with radionuclides such as indium-111, Zirconium-89 and Technetium-99 for *in vivo* imaging of cancer biomarkers such as HER2, EGFR and somatostatin, both in preclinical research and in the clinic (Ducharme & Lapi, 2020; M. H. Kim et al., 2022; Perik et al., 2006). Peptides targeting somatostatin such as [^{111}In]-DTPA^{0}-octreotide and its analogues are already used in the clinic to image neuroendocrine tumours (Poeppel et al., 2011). The approval of radiolabelled peptides as molecular imaging agents is beset by several limitations. One major drawback of native linear peptides is susceptibility to proteolytic enzymes, hence very short biological half-life. Chemical modifications such as cyclisation, PEGylation, introduction of unnatural amino acids and amidation have been successfully employed to improve peptide metabolic stability *in vivo*. Peptides can also display very high uptake in the kidneys which has been linked with nephrotoxicity. This challenge has been addressed through infusion of a mixture of amino acids, such as lysine and arginine, that reduces kidney uptake and enhances renal clearance of peptide radiopharmaceuticals (Ayo & Laakkonen, 2021; Fani et al., 2012).

Peptide targeting sequences are derived using three main methods: derivatization from natural proteins, screening peptide libraries using phage display and chemical synthesis and structure-based rational engineering. Phage display is frequently used because it is favourably cheaper and can allow for screening of a large peptide library. A library of peptides is usually expressed in the phage particles and allowed to interact with the target protein followed by several rounds of washes and elution and optimisation of high affinity peptides (Sun et al., 2017a; Tal et al., 2016).

1.3.3 Cell penetrating peptides

Only small and highly lipophilic molecules can efficiently translocate the cell membrane and localize into cells (Slastnikova et al., 2018). The delivery of larger cargos such as monoclonal clonal antibodies and proteins has proved very challenging. Several *in vitro* methods have been used to deliver large molecules to the interior of the cells including electroporation, microinjection and electrosonic jet injection. These techniques are limited to *in vitro* experiments and therefore cannot be translated in animal studies or clinical use (Torchilin, 2006). Molecular cargo carriers termed as cell penetrating peptides (CPP), that allow efficient intracellular delivery of diagnostic and therapeutic agents have helped to circumvent these limitations. CPP have been used to deliver various cargoes including nucleic acids, proteins, SiRNA, therapeutic agents and nanoparticles. CPP, also called protein transduction domains, are 5-30 amino acids in length and mostly positively charged at physiological pH due to the presence of basic amino acids such arginine and lysine residues (Derakhshankhah & Jafari, 2018). The first CPPs to be discovered were TAT and penetratin derived from HIV-TAT and Antennapedia homeodomain, respectively. Both have been employed in the delivery of different therapeutic regimens, such as fluorescent or radioactive compounds for imaging and peptides/proteins for therapeutic application. The cargos are usually attached to the CPP via covalent conjugation or electrostatic interaction. A plethora of CPPs have been discovered, either from native protein such as TAT and penetratin or a combination of sequences motifs from other peptides, for instance transportan. CPP can also be made synthetically such as the polyarginine family (Milletti, 2012).

CPPs cross the cell membrane through different mechanisms, but the details of their mechanisms remain a matter of debate and further characterisation. They include energy-dependent mechanisms such as endocytosis pathways and energy-independent mechanisms

for instance direct penetration pathways. The method of internalization depends on several factors including size of the cargo-CPP conjugate, peptide concentration, the nature of the CPP and the type of peptide sequence. At higher concentration, many cationic CPPs show to enter the cells via direct penetration, whereas the dominant mechanism of uptake tend to be endocytosis at lower concentrations (Ruseska & Zimmer, 2020).

1.3.3.1 HIV trans-Activator of transcription peptide (TAT)

TAT is a 14 kDa RNA-binding protein that plays a pivotal role in viral genome transcription and replication. TAT interacts with a structured RNA element (TAR) of the human immunodeficiency virus (HIV-1) recruiting various transcriptional complexes such as enzymes with histone and acetyl transferase activity to enhance the processivity of RNA polymerase II thus promoting the elongation of viral transcripts (Brigati et al., 2003). Initial studies demonstrated that TAT (an 86-amino acid protein) was able to efficiently cross the lipid bilayer of the plasma membrane and localise into the nucleus of the cells. The characterisation of different domains of the TAT protein revealed the specific region involved in cellular transduction. TAT contains a very strong transcriptional domain composed of a cysteine-rich region and a hydrophobic core motif, along with an arginine-rich RNA-binding motif (ARM) that specifies its binding (**Figure 1:7**). The TAT peptide, with amino acid sequence YGRKKRRQRRR, is derived from this ARM region (aa 47-57). This peptide has been explored for intracellular delivery of diverse non-permeable drugs such as anti-sense oligonucleotides and intact monoclonal antibodies. The GRKKR sequence of TAT was established as a nuclear localisation sequence that facilitates the entry of TAT cargo complexes into the nucleus. The mechanism of nuclear import of the TAT peptide involves association with nuclear import carriers such as importin-α and β, leading to translocation across the nuclear membrane (Freitas & Cunha, 2009).

A variety of TAT constructs have been employed in the intracellular delivery of molecular imaging agents. Polyakov et al., first demonstrated that membrane permeant peptide conjugated to HIV-1 Tat transactivation protein sequences (GRKKRRQRRR) and technetium-99m ([(99m) Tc]Tat-peptide) was able to concentrate rapidly within the cytoplasm and nucleus of living human cells (Polyakov et al., 2000). The Reilly group showed the use of TAT in delivering ^{123}I- or [^{111}In]-labelled monoclonal antibodies into the nucleus *in vivo*, interacting with intracellular targets (Cornelissen et al., 2007). Cornelissen et al. has employed [^{111}In]-labelled and 89Zr-labelled TAT-IgG conjugates for *in vivo* imaging of γH2AX, a DNA damage marker *in vivo* in breast and pancreatic ductal adenocarcinoma cancer xenograft models (Cornelissen et al., 2011; J. Knight et al., 2015; J. C. Knight et al., 2017). In this project, we will employ the TAT peptide (GRKKRRQRRRPPQGYG) for the intracellular delivery of a p53 monoclonal antibody for *in vitro* and *in vivo* imaging of PDAC tumour models.

The mechanism of TAT cellular uptake involves lipid raft–dependent macropinocytosis, which is a specialised form of fluid phase endocytosis that involves membrane protrusion causing the plasma membrane to transport extracellular contents into the cells. The specific mechanism of arginine-rich peptide such as TAT entail the interaction of the peptide with membrane proteoglycans such as heparan sulfate proteoglycan leading to the activation of Rac protein that induces F-actin organisation and macropinocytosis (Futaki et al., 2007). Once the peptide in macropinosome is inside the cell, they leak out into the cytoplasm followed by nuclear import. The mechanism of endosomal escape remains poorly understood, with several mechanisms proposed including direct translocation across endosomal membrane, proton-sponge hypothesis and induction of vesicle budding and collapse (Sahni A et al., 2020, Sonawane et al., 2003).

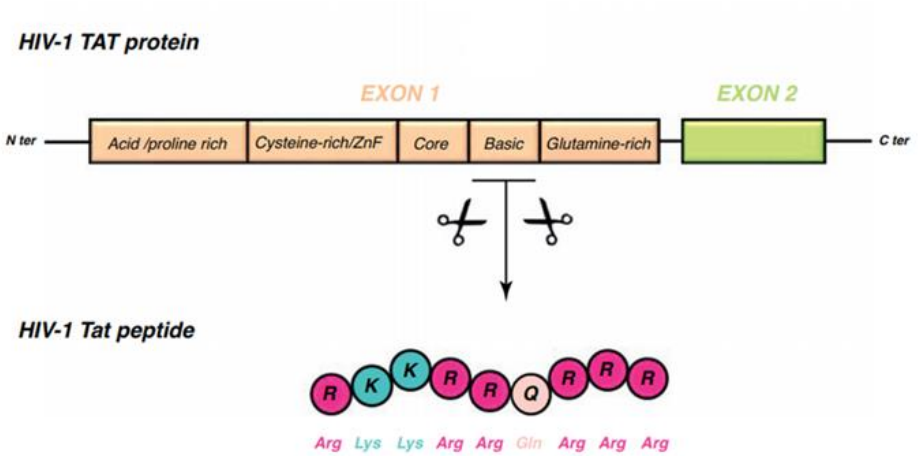


Figure 1:7) The HIV-1 TAT peptide. The TAT peptide is derived from the basic domain of the TAT protein and facilitates entry into the cell promoting viral gene expression. Adapted from (Rizzuti et al., 2015).

Endosomal entrapment of TAT peptide and its cargos remain a hindrance to effective intracellular delivery of therapeutics, and thus affecting therapeutic efficacy. Research is ongoing to attempt to solve this problem, including the use of cyclised TAT peptides or linear oligoarginines which have demonstrated improved cargo delivery compared to linear TAT peptide. These have, however, not made way into in vivo applications due to high concentrations of CPP required to achieve desirable results in vivo (>10 µM) (Nischan et al., 2015; Schneider et al., 2021). Recently, Vallis group at Oxford have designed tricyclic CPPs (Tat trimers) based on the linear and cyclic sequences of the TAT peptide. The TAT trimers exhibited increased and efficient cellular uptake in HeLa and CHO cells. In addition, the trimeric TAT was distributed homogeneously in the cytoplasm and nucleoli with no evidence of endosomal entrapment, which was contrast to monomeric TAT. These novel peptides accumulated in cells within 15 minutes at a concentration of <1µM, with no evidence of unwarranted cellular toxicities (Tietz et al., 2022). The trimeric peptides are promising carriers for intracellular delivery of therapeutic cargos and should be further investigated and/or optimised for *in vivo* applications and clinical translation.

1.4 Antibody conjugation methods

Monoclonal antibodies have revolutionised the treatment of cancer, yet their scope of clinical application and therapeutic efficacy remain limited. To increase their diversity and efficacy, therapeutic antibodies are covalently modified with cytotoxic payloads such as tubulin inhibitors and DNA damaging agents (Criscitiello et al., 2021). Monoclonal antibodies can also be modified by covalent addition of detective agents such as gamma-emitting radionuclides and fluorescent molecules for use in molecular imaging of tumours and other diseases (Chomet et al., 2021; Haugland, 1995).There are different methods that are employed to conjugate antibodies to ligands. One method of classifying antibody conjugation strategies is based on the site-specificity and categorises the conjugation methods into site-specific and non-site specific.

1.4.1 Site-specific conjugation

Site-specific antibody conjugation involves the coupling of antibodies with ligands on unique and defined sites through native or engineered amino acids. The most common site-specific conjugation involves coupling moieties to an antibody through engineered cysteine residues. A cysteine residue is engineered into specific sites on the antibody heavy or light chains. The cysteine contains thiol reactive groups which can be conjugated via disulphide exchange or addition of electrophiles such as iodoacetamide and maleimide (Q. Zhou, 2017). Using this method, Junutula and colleagues successfully produced a homogeneous engineered thio-trastuzumab-mpeo-DM1 conjugate for targeting HER2 positive breast cancer with improved therapeutic efficacy compared to one prepared using non-site-specific conjugation. In another work, antibodies engineered with cysteines were coupled with thiol-reactive linkers containing cytotoxic monomethyl auristatin E (MMAE), using thiol-maleimide chemistry. A

homogeneous antibody drug conjugate was obtained with a drug-antibody ratio (DAR) of 1.6 compared to 3.1 DAR when conventional native cysteine residues conjugation was used (Junutula et al., 2008, 2010).

Conjugation via engineered cysteine residues ensures precise control of the antibody-drug-ratio (ADR), hence consistence ADC production, minimising batch-to-batch variation. The major drawback of cysteine conjugation is that it us susceptible to maleimide exchange with other reactive thiols *in vivo* such as albumin, glutathione, or cysteine present in plasma (Q. Zhou, 2017). Site-specific antibody modification can also occur through incorporation of unnatural amino acids such as acetylphenylalanine and azido-lysine via engineered orthogonal tRNA/aminoacyl-tRNA synthetase pairs, engineered short peptide tags such as glutamine tag or through the N297 glycans located on the CH2 domain of the antibody Fc region (Q. Zhou, 2017). Site-specific conjugation offers the advantage of minimising production of heterogeneous antibody-ligand conjugates i.e., number of ligands coupled to a specific site on the antibody (Panowski et al., 2013). One is therefore able to maintain the site and number of payloads coupled to an antibody which leads to pure drug load with similar pharmacokinetics profile. However, these techniques are very labour intensive and costly compared to conventional antibody conjugation methods.

1.4.2 Non-site-specific antibody conjugation

Non-site-specific antibody modifications involve the covalent modifications of either surface-exposed lysines (~80) or interchain disulphides (8 in IgG1). Lysine -based conjugation occurs via the amine side chains because of their nucleophilicity. Of the ~80 lysines on the monoclonal antibody, only 20 are solvent accessible and serve as potential sites for attaching payloads via an amide or amidine bond (McCombs & Owen, 2015). Activated esters such as

N-hydroxysuccinimidyl (NHS) or sulfo-NHS esters react with the antibody lysine residues forming an amide bond, while imido ester compounds such as Traut's reagent forms amidine bonds (N. Jain et al., 2015). While conjugation on lysines can lead to high number of payloads added to the antibody leading to high ADR (0-8), there is lack of control over the number of payloads attached per antibody as well the site of conjugation. This can lead to generation of over one million species of antibody-drug-conjugates with diverse pharmacokinetics properties. There is also lack of batch-to-batch consistence (Panowski et al., 2013). This heterogeneity can be minimised by reducing the number of payloads added (1-4) or carrying out antibody lysine conjugation reaction under very stringent conditions by exploiting the differences in pKa values of N-terminal α-amine (6.8 - 9.1) and lysine ε-amino group (10.5). The former strategy comes with the challenge of compromising the antibody binding kinetics due to the proximity of the N-termini to the antigen biding domains (Scheck & Francis, 2007).

The conjugation of monoclonal antibodies on native cysteines occurs via partial reduction of the four interchain cysteine bonds exposing eight sulfhydryl groups for attaching electrophiles such as iodoacetamide and maleimide. Up to eight payloads can be attached per antibody, generating more than 100 different species of ADCs. Over-modifying native cysteines can damage the antibody backbone affecting the *in vivo* pharmacokinetics. Also, cysteine-based conjugation is prone to substitution *in vivo* with native thiol-containing molecules such as albumin and glutathione which affects the stability and bioavailability of the ADC (Panowski et al., 2013).

Non-site-specific conjugation randomly tags any of the surface exposed modifiable amino acids with residues producing heterogenous mixtures of antibody conjugates. The

heterogeneity in conjugation site and antibody payload presents an inherent challenges of product characterisation, batch-to-batch consistency, and varying pharmacokinetics.

1.5 Aim of the project

Monoclonal antibody and peptide-based radioimmunoconjugates (RICs) have a great potential to improve cancer imaging, owing to their exceptional nanomolar affinities and exquisite specificities. While RICs have been employed to image a variety of maladies, their scope of application remains underexplored. The prime objective of this DPhil project was to develop SPECT mAb RIC for *in vitro* and *in vivo* interrogation of mutant p53 expression status in PDAC models. PDAC is a highly aggressive and lethal malignancy with the lowest survival rates mainly due to lack of effective diagnostics and therapies. This work served to establish a proof-of-concept that imaging aberrant mutant p53 expression in PDAC models is possible.

In Chapter 2, a new anti-p53 (49A1/H10) mAb was produced, purified, and characterised. Its specificity and affinity were determined in PDAC cell lines with different p53 expression and/or mutation status.

In Chapter 3, the 49A1/H10 mAb was conjugated to the TAT peptide and the metal ion chelator DTPA, to allow radiolabelling with [^{111}In]. The binding affinity, serum stability, cellular uptake, and retention of the radiolabelled 49A1/H10 were evaluated in three PDAC cell lines with increasing levels of p53 protein.

In Chapter 4, the ability of [^{111}In]-DTPA-49A1/H10-TAT to image total p53 in PDAC subcutaneous xenografts was evaluated using SPECT imaging.

In Chapter 5, an attempt was made to characterise and select a lead peptide with high p53 specificity and affinity.

2 Chapter 2 – Production and validation of a novel anti-p53 mAb

2.1 Introduction

Monoclonal antibodies possess high binding specificities and affinities combined with versatility making them exceptional therapeutics. In the laboratory, they are employed in cell and protein-based immunoassays such as Western blot, ELISA, flow cytometry and in the diagnosis and treatment of preclinical animal disease models. Monoclonal antibodies are increasingly becoming the cornerstone of disease diagnosis and treatment such as covid-19 and cancer. As of March 2022, 14 monoclonal antibody drug conjugates (ADCs) had been approved for clinical use, with over 100 candidates under clinical evaluation (Fu et al., 2022).

Critical to the approval of monoclonal antibodies for use is the antibody validation process. Monoclonal antibodies must be evaluated for specificity, binding kinetics, off-target toxicity, and reproducibility before qualifying for use in laboratory research or in the clinic. Despite their daily use, most of commercial antibodies suffer from batch-to-batch variation and lack of reproducibility due to inadequate validation process, limiting their applications. To overcome these challenges, standard protocols for the validation of antibodies have been developed. The International Working Group for Antibody Validation (IWGAV) proposed for five conceptual pillars for antibody validation: (i) genetic strategies, (ii) orthogonal strategies, (iii) independent antibody strategies, (iv) expression of tagged proteins, and (v) immunocapture followed by mass spectrometry (Uhlen et al., 2016). At least one of these pillars must be met during the antibody validation process. Assays such as Western blot, ELISA, immunohistochemistry, immunocytochemistry, and flow cytometry are employed in validating antibody specificities and affinities. To ensure antibody reproducibility, IWGAV proposed the identification of antibody sequence as well as assignment of lot numbers to all antibody batches. An excellent antibody should be highly selective and specific, possess

picomolar/nanomolar affinity, reproducible and able to binds to its target in both near-native or denatured form (Voskuil, 2014).

TP53 is the main tumour suppressor gene and the most mutated in human cancers. As such, TP53 gene and its product p53 protein have dominated basic cancer research with over 9,500 p53 antibodies listed on Antibodypedia website, and over 113,000 reference publications found on PubMed (Antibodypedia, n.d.). TP53 mutations have been shown to cause cancer aggressiveness and resistance through gain-of-function and dominant negative effect capabilities. In addition, mutant p53 overexpression promote tumour aggressiveness and therapy resistance (Alexandrova et al., 2017). In PDAC, TP53 mutations occur in approximately 75% of PanIN-3 lesions and PDAC tumours. The majority of PanIN-3 lesions and PDAC tumours have been shown to overexpress p53 hotspot mutants, which also correlate with poor prognosis among patients. Of note, mutant R248W and R273H have been found to be overexpressed in PDAC tumours and enhance tumour aggressiveness and resistance to chemotherapies (Fiorini et al., 2015; Morton et al., 2010).

This study aimed to validate a novel anti-p53 monoclonal antibody for use in subsequent aims of the project, as well determine the levels of p53 hotspot mutants in PDAC cell lines. Eight anti-p53 hybridoma clones (**Table 2.2.1**) were employed in the validation assays to select the best clone with favourable specificity and affinity. Western blot was used to evaluate the selectivity and specificity of the antibodies on denatured cell lysates. Immunocytochemistry followed by confocal microscopy was used to confirm both the localisation and specificity of antibodies on fixed cells with near-native proteins. Flow cytometry was employed to confirm both p53 specificity and binding affinities of antibodies on near-native cells. Cell lines with

different p53 status (wild type, structural and contact mutants, and p53 null) were employed to evaluate both the antibody specificity and binding on total p53 protein.

In addition, four cell lines expressing p53 hotspot mutants representing approximately 22% of all p53 mutants in PDAC were evaluated for p53 expression levels in relation to normal human pancreas tissue lysate.

2.2 Selection and validation of new anti-p53 hybridoma clones

2.2.1 Materials and methods

p53 antibodies in hybridoma supernatant were evaluated for selectivity and specificity using Western blot, flow cytometry and immunocytochemistry assays. Two mutant p53 cancer cell lines, human FAMPAC-1 (R175H) and murine B8484 (R172H), were used as p53 positive cell lines. Two p53 null cancer cell lines, human H1299 and mouse P2FIR were used as negative controls. In addition, we employed a commercially available rabbit p53 polyclonal antibody PAB 10442-1-AP (Proteintech, USA) as a positive control and Mouse IgG as the negative control.

2.2.1.1 Cell culture

Except where mentioned, all cell lines employed in our experiments were cultured in Dulbecco's Modified Eagle Medium (DMEM) (Thermo Fisher Scientific, UK), supplemented with 10% (v/v) of foetal bovine serum (FBS) (Gibco, USA), 100 units/mL penicillin, 100 ug/mL streptomycin, and 2 mM L-glutamine (Thermo Fisher Scientific, UK). Cells were grown in T-175 flasks (Greiner Bio-One, UK) and maintained in a 5% CO_2 humidified chamber at 37°C and passaged when they reached 70 – 80% confluence.

2.2.1.2 Anti-p53 hybridomas

All the eight novel p53 antibodies (**Table 2.2.1**) were generated and donated to us by Professor Alison Banham, (NDCLS).

Table 2.2.1) p53 antibodies for validation.

Antibody	Species	Dilution
49A	Mouse	1 : 10
49A1/B12	Mouse	1 : 10
49A1/B4	Mouse	1 : 10
49A1/D4	Mouse	1 : 10
49A1/E5	Mouse	1 : 10
49A1/H10	Mouse	1 : 10
49A1/H12	Mouse	1 : 10
p53 Polyclonal antibody 10442-1-AP	Rabbit	1 : 1000
Mouse (G3A1) mAb IgG1 Isotype Control	Mouse	1 : 1000
Anti-PCNA antibody [EPR3821] (HRP)	Rabbit	1 : 5000
Goat anti-Mouse IgG (H/L): HRP	Mouse	1 : 5000
Goat anti-Rabbit IgG (H/L): HRP	Rabbit	1 : 5000

2.2.2 Western blot

Western blot was performed to evaluate antibodies specificities on denatured human and murine cell lysates with different p53 expression status.

2.2.2.1 Cell lysate preparation

Cells at confluence were harvested by adding 3 mL trypsin-ethylenediaminetetraacetic acid (Trypsin-EDTA) (Sigma Aldrich) to T-175 flask and incubated for 5 min. Trypsin-EDTA was

neutralised by addition of 7 mL of culture media to the detached cells and then placed on ice. Cells were washed 2× in cold PBS and lysed in 100 – 300 µL Mammalian Protein Extraction Reagent (M-PER buffer) (Thermo Fisher Scientific, UK) containing cOmplete™ EDTA-free Protease Inhibitor Cocktail (Sigma, UK) by shaking gently at 400 rpm for 5 min at room temperature (RT). The lysates were centrifuged at 14,000 × g for 20 min to pellet the cell debris. The supernatants were collected in fresh microcentrifuge tubes and the protein concentration determined by BCA assay (Sigma, UK) prior to further analysis or storage at -20℃ until required.

2.2.2.2 SDS-PAGE & western blot

Whole cell lysates were fractionated by SDS-PAGE midi-gel electrophoresis XCell4 SureLock™ Midi-Cell system (Thermo Fisher Scientific, UK). The samples were reduced and linearised by addition of 4× Laemmli SDS Protein Loading Buffer ((Thermo Fisher Scientific, UK) followed by heating at 90°C for 5 min. Each of sample (30 µg /15 µL) was loaded into a pre-cast 4-12% NuPAGE Bis-Tris gels (Thermo Fisher Scientific, UK). Proteins were separated in NuPAGE MES SDS Running Buffer (20X) (Thermo Fisher Scientific, UK) for 45 min at 200 V. The fractionated proteins were transferred to a pre-activated PVDF membrane using an iBlot 2 Dry Blotting System (Thermo Fisher Scientific, UK), and rinsed in PBS pH 7.4 for 5 min. Membranes were blocked with 5% (w/v) skim milk powder solution (Sigma-Aldrich for 1 h at RT and then washed 3 x 5 min with PBST (PBS + 0.1% Tween). The blocked membranes were incubated with the primary antibodies (dilutions 1:100 for antibody supernatants and 1:1000 for commercial control antibodies) for 2 h at RT, washed 3 x 5 min with PBST and then incubated with HRP-conjugated secondary antibodies (dilution 1:5000) to for 1 h. The immunoblots were washed 3 x 5 min in PBS and then developed by addition of chemiluminescent substrate (1:1 solution of Luminol/Enhancer solution and stable peroxidase solution) (Thermo Fisher scientific, UK)

for 5 min. The protein bands images were acquired using the C-DiGit Chemiluminescent Western Blot Scanner (LI-COR Biosciences, USA). Membranes were then rinsed in tap water for 5 minutes and then incubated with the stripping buffer (Thermo Fisher Scientific, UK) for 10 min at room temperature. Membranes were then reprobed for PCNA loading control using Anti-PCNA antibody (Abcam).

2.2.3 Flow cytometry

Cells at confluence were harvested by enzymatic release using 0.25% Trypsin EDTA solution and centrifuged at 250 x g for 5 min and the media discarded. Cells were washed 2x in cold PBS by centrifugation for 5 min at 250 x g. This was followed by fixing in freshly prepared 4% paraformaldehyde for 10 min, washed 3x in PBS, permeabilised with 0.1% (v/v) Triton X-100 in PBST for 20 min and washed again 3x in PBS. Cells were blocked with 2% (w/v) BSA in PBST for 30 min, incubated with the primary antibodies diluted in blocking buffer for 2 h at RT and washed 3x in PBST. Primary antibody-stained cells were incubated with Alexa Fluor® 488 conjugated secondary antibody for 1 h. The cells were washed 3x in PBS and then resuspended in fresh PBS for further analysis. Cells analysis was done using Invitrogen Attune NxT flow cytometer (Invitrogen, CA, USA). Data was analysed using the FloV10 software.

2.2.4 Immunocytochemistry

Cells (20,000 per well) were seeded in 200 µL of culture in a Falcon® 8-well culture slides (Corning Life Sciences) and incubated for adherence overnight in a 5% CO_2 humidified chamber at 37°C. The media was removed, and the slide chambers washed three 3 x 5 min with cold PBS on a Talboys Standard Analog 1000RS Rocking Shaker (Thermo Fisher Scientific, UK). The slide-bound cells were fixed in in freshly prepared 4% paraformaldehyde for 10 min, washed 3x in PBS, permeabilised with 0.1% (v/v) Triton X-100 in PBST for 20 min and washed

again 3x in PBS. Blocking solution (2.5% (w/v) BSA, 5% (v/v) goat serum and 0.3 M glycine prepared in PBST) was added and incubated for 1 h at RT. The blocking solution was aspirated, and coverslips washed 3 x in PBST and then incubated with primary antibody for 2 h. The secondary antibody in blocking solution was added and incubated for 1 h at RT. The stained cells were washed 3x in PBS and the mounting media containing DAPI (Vector Laboratories, CA, USA) added. The mounted slides were stored at 4°C. Finally, image acquisition of the stained cells was performed using Leica TCS SP8 platform (Leica Microsystems, Wetzlar, Germany), equipped with 63× oil immersion objective lenses. Optimised imaging acquisition and processing parameters were maintained across all samples and experiments. Images were analysed using ImageJ software (National Institutes of Health, USA).

2.2.5 Determination of p53 Protein expression in Pancreatic Cancer Cell Lines

TP53 mutants are wide in spectrum and show heterogeneous expression profile. To qualify as an ideal imaging biomarker, p53 must be expressed in excess fold in diseased state compared to the healthy tissue to provide a clear contrast and high signal to background ratio. These assays aimed to investigate the expression levels of four p53 hotspot mutants in PDAC cell lines: FAMPAC-1 ($p53^{R175H/+}$), MiaPaCa-2 ($p53^{R248W/+}$), BxPC-3 ($p53^{Y220C/+}$) and PANC-1 ($p53^{R273H/-}$) relative to normal pancreas tissue lysate (HPWTL) using Western blot and ELISA.

2.2.5.1 Western Blot

Cells at 70 – 80% confluence were harvested by enzymatic release using 0.25% Trypsin EDTA solution. Cells were washed 2x in cold PBS and counted using Countess 3 Automated Cell Counter (Thermo Fisher Scientific, USA). For each cell line, 1,000,000 cells were lysed in 100 µL M-PER buffer containing cOmplete™ EDTA-free Protease Inhibitor Cocktail. The lysates were centrifuged at 14,000 × g for 20 min to pellet the cell debris and supernatants for each

cell line was collected. The protein concentration of each sample was determined by BCA assay (Sigma, Dorset, UK) prior to storage a -20°C until required further analysis.

2.2.5.2 SDS-PAGE & western blot

Equal amount (30 µg/15 µL) of linearised cell lysates was loaded onto a pre-cast 4-12% NuPAGE Bis-Tris gels. Proteins were fractionated in NuPAGE MES SDS Running Buffer (20X) using SDS-PAGE midi-gel electrophoresis XCell4 SureLock™ Midi-Cell system for 45 min at 200 V. The separated proteins were transferred to a pre-activated PVDF membrane using an iBlot 2 Dry Blotting System and rinsed in PBS pH 7.4. The membranes were blocked with 5% (w/v) skim milk powder solution for 1 h at RT and the rinsed 3 x 5 min in PBST. The blocked membranes were incubated with the anti-p53 49A1/H10 monoclonal antibody (concentration: 5 µg/mL) for 2 h at RT and washed as described above. The membrane was incubated with anti-mouse IgG secondary antibody, coupled to HRP (dilution 1:5000) for 1 h. The immunoblots were then washed 3 x 5 min in PBS and then developed by addition of chemiluminescent substrate (1:1 solution of Luminol/Enhancer solution and stable peroxidase solution) for 5 min. The protein bands images were acquired using the C-DiGit Chemiluminescent Western Blot Scanner. The protein bands were semi-quantitatively analysed using Image J software.

2.2.5.3 ELISA

The p53 protein levels were determined using the Human p53 ELISA Kit (BMS256) (Thermo Fisher Scientific, UK) according to manufacturer's protocol. The kit contains all the buffers and reagents needed for the assay. Cell lysates for all cell lines were prepared using M-PER buffer as described in section **2.1.15**. ELISA plate wells were washed 2x with 300 µL of wash buffer per well. The wash buffer was allowed to sit in the wells for 30 seconds before aspiration.

Wells were covered with 50 µL of sample diluent before 50 µL of 4 µg/mL of each sample added in triplicate wells to a final concentration of 2 µg/mL. Each well was added with 50 µL of Biotin-Conjugate and the plate covered with an adhesive film. The plate was incubated at RT on a microplate shaker (300 rpm) for 2 h. The well contents were aspirated and then washed 3x with the wash buffer. Wells were covered with 100 µL of Streptavidin-HRP and incubated at RT on a microplate shaker for 1 h. Each well was added with 100 µL of TMB-substrate and incubated in the dark on the bench for 10 min to allow for colour development. Excessive colour development was stopped by adding 100 µL of the stop solution to each well. The absorbance for each well was read on a spectro-photometer using 450 nm as the primary wavelength and 620 nm as the reference wavelength. A standard curve was created by plotting the average absorbances of the standard concentrations against human p53 concentrations. The p53 concentrations for the cell lines were determined using the standard curve.

2.3 Production and purification of anti-p53 49A1/H10 monoclonal antibody

The characterisation of the novel eight antibodies led to the selection of clone 49A/H10 as the best p53 mAb for large scale production, purification and use in future experiments. The antibody hybridomas were cultured and harvested in supernatant for purification using protein G purification method.

2.3.1 Anti-p53 49A1/H10 hybridomas culture

The 49A1/H10 hybridomas were thawed and cultured in T25 flasks in RPMI 1640 media supplemented with 10% (v/v) of foetal bovine serum (FBS) (Gibco, USA), 100 units/mL penicillin, 100 µg/mL streptomycin, and 2 mM L-glutamine. The cells were incubated in 5%

CO_2 humidified chamber at 37°C and allowed to grow until they reached 90% confluence. Hybridomas were harvested and washed 2x in cold PBS via centrifugation at 250 x g. The PBS was discarded, and the cells transferred in CD Hybridoma Medium (Life Technologies) containing 100 units/mL penicillin, 0.1 mg/mL streptomycin, 50 µg/mL gentamicin and cultured to adapt and thrive in FBS free media. The exponentially growing 49A1/H10 cells were expanded in 10 T175 flasks (1:20 dilution) and grown for three weeks for maximal antibody production. The supernatants containing the antibody were harvested and centrifuged at 4400 x g for 20 min to pellet the hybridomas and then filtered 2x through 0.2 µm filters before further purification to obtain a pure antibody.

2.3.2 FPLC Purification (Protein G Column)

Antibody purification was performed using fast protein liquid chromatography (FPLC) ÄKTA prime plus system (GE Healthcare, Sweden) in conjunction with a 1 mL HiTrap protein G purification column (GE Healthcare, Sweden). The filtered hybridoma supernatant was adjusted to pH 7.4. The protein G column was primed for antibody binding by pumping 10 mL of 20 mM Sodium Phosphate pH 7 (binding buffer) through the column. The hybridoma supernatant was then pumped through the column at a flow rate of 1 mL per minute to allow for antibody binding on the column. The column was washed with 10 column volumes of the binding buffer and the bound antibody eluted using 0.1 M glycine, pH 2.7 and collected as fractions of 500 uL. Each fraction was naturalised by pre-added 50 µL of 0.5 M sodium bicarbonate, pH 8.5. The fractions were combined, and the antibody concentration determined by UV absorbance spectrometry at 280 nm. The antibody was concentrated to >2 mg/mL using a Vivaspin® 50,000 MWCO centrifugal concentrator (Sigma-Adrich, USA) and buffer exchanged to PBS pH 7.4 using a HiTrap desalting column (Sigma-Adrich, USA). Aliquots of 200 µg in 100 µL were stored at -20°C for future use.

2.3.3 Reducing and non-reducing SDS-PAGE

For reducing SDS-PAGE, 2x SDS protein sample buffer was prepared by mixing: 1.25 mL 1 M Tris-HCL (pH 6.8), 4.0 mL 10% (w/v) SDS, 2.0 mL glycerol, 0.5 mL 0.5 M EDTA, 4 mg bromophenol blue, 0.2 mL 14.3 M β-mercaptoethanol and 2.05 ddH20. Anti-total p53 (49A1/H10) mAb sample was mixed with equal volume of 2x SDS protein sample buffer and the sample placed on a heating block at 95°C for 5 min. 15 µL of 20 µg of each sample loaded onto a pre-cast 4-12% NuPAGE Bis-Tris gels (Thermo Fisher Scientific, UK). Proteins were separated in NuPAGE MES SDS Running Buffer (20×) (Thermo Fisher Scientific, UK) for 45 min at 200 V. For non-reducing SDS-PAGE, the 2xSDS protein sample buffer was prepared without β-mercaptoethanol. The gels were washed in PBS and stained by incubating on a shaker for 1 h at RT in 100 mL Coomassie blue staining solution (0.1% Coomassie® R-250, 40% ethanol and10% acetic acid). The gels were distained in 100 mL distaining solution (10% ethanol and 7.5% acetic acid) by incubating for 2 h on a shaker at RT. The gels were then transferred in ddH20 and imaged using an iPhone 7 mobile camera (Apple, USA).

2.3.4 Saturation binding assay

The k_D for 49A1/H10 was determined using flow cytometry on mutant and wild type p53 with increasing antibody concentrations in nanomolar range. Cells were harvested by enzymatic release using 0.25% Trypsin EDTA solution and centrifuged for 5 min at 250 x g and the media discarded. Cells were washed twice in cold PBS by centrifugation for 5 min at 250 x g. At least 200,000 cells per well in triplicate were dispensed on a 96-well plate. Cells were fixed by freshly prepared 4% paraformaldehyde for 10 min, washed 3x in PBS, permeabilised with 0.1% (v/v) Triton X-100 in PBST for 20 min and washed again 3x in PBS. Wells were blocked with 2% (w/v) BSA in PBST for 30 min, incubated with the 49A1/H10 diluted in the blocking buffer for 2 h at RT and washed 3x in PBST. The stained cells were incubated with Alexa Fluor®

488 conjugated secondary antibody for 1 h. The wells were washed 3x in PBS and then resuspended in fresh PBS for further analysis. Cells analysis was done using Invitrogen Attune NxT flow cytometer (Invitrogen, USA). Data were analysed using FlowJoTM (BD Biosciences, USA).

2.3.5 Statistical analysis

GraphPad Prism v8 (GraphPad Software, CA, USA) was utilised in statistical analysis of all data. One-way ANOVA with Tukey's post hoc test was used to compare differences in group means for p53 protein levels in different cell lines. All experiments were carried out at least in triplicate and presented as mean ± one standard deviation unless otherwise stated.

2.4 Results

2.4.1 Validation of anti-p53 (49A1/H10) monoclonal antibody

Antibody validation experiments aimed to select a p53 monoclonal antibody that bound to total p53 (mutant and wild type) with excellent specificity and nanomolar affinity. Six cell lines with different p53 expression status were selected for use in our validation experiments (**Table 2.1.2**).

Table 2.1.2) p53 cell lines used in monoclonal antibody validation experiments. (CT – contact mutant, LNM – lymph node metastases, SM – structural mutant, SCLC – small cell lung cancer, WT – wild type).

Cell line	Organ	Disease	Genetic status	p53 status
MiaPaCa-2	Exocrine pancreas	PDAC	$p53^{R248W/R248W}$	CT
FAMPAC-1	Exocrine pancreas	PDAC	$p53^{R175H/R175H}$	SM
HT1080	Connective tissue	Fibrosarcoma	$P53^{wt}$	WT
H1299	Lungs (LNM)	SCLC	P53-/-	Null
B8484	Pancreas	KPC mouse	$p53^{R175H/R175H}$	SM
ASPC-1	Pancreas	PDAC	$P53^{-/-}$	Null
P2FIR	Pancreas	KPC mouse	$P53^{-/-}$	Null
BxPC-3	Pancreas	PDAC	$P53^{Y220C/Y220C}$	SM
PANC-1	Pancreas	PDAC	$P53^{R273H/WT}$	CT

2.4.1.1 Western blot analysis

Western blot was performed as the first screening assay to assess the presence of p53-specifc protein bands corresponding to the molecular weight of p53. Antibodies were evaluated for murine and human p53 binding specificity, hence the use FAMPAC-1, H1299, B8484 and P2FIR whole cell lysates. Clones 49A, 49A1/B12, 49A1/C2, 49A1/D4, 49A1/H10 and 49A1/H12 produced p53 specific bands between 40 and 50 kDa in FAMPAC-1 and B8484 lysates. Clones

49A1/B4 and 49A1/E5 bound to FAMPAC-1 and not in B8484 lysates. No antibody displayed any non-specific related bands in H1299 and P2FIR cell lysates (**Figure 2:1**).

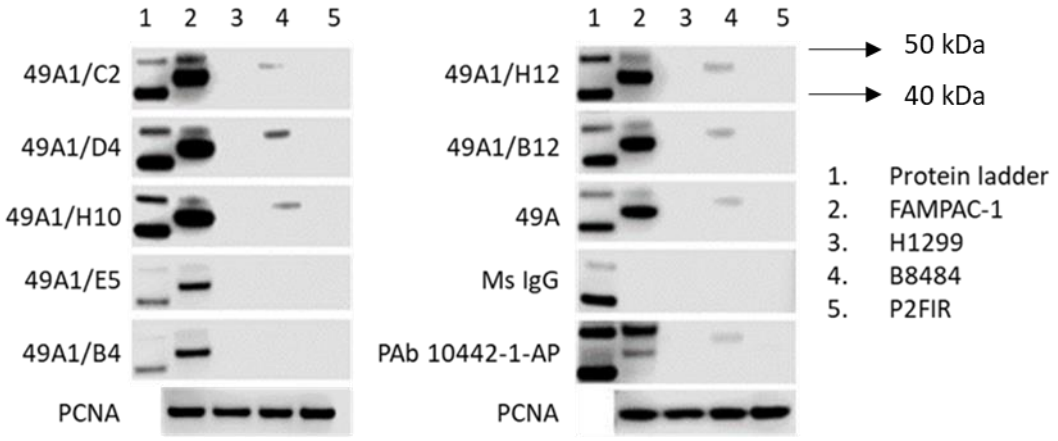


Figure 2:1) Western blot analysis of p53 antibodies. A) Western blot showing p53 protein bands of different p53 antibodies. Membranes were incubated with the primary p53 antibodies and then probed by HRP-conjugated anti-mouse IgG secondary antibody and imaged using the C-DiGit Chemiluminescent Western Blot Scanner. After imaging, membranes were washed with Western blot stripping buffers and probed for PCNA loading control using Anti-PCNA antibody. Full blot Western blots are shown in Appendix section **Figure 8:1A.**

2.4.1.2 Flow cytometry analysis

Western blot results were confirmed using flow cytometry for clones 49A, 49A1/H12, 49A1/D4, 49A1/H10 and 49A1/H12. Incubation of fixed and permeabilised FAMPAC-1, H1299, B8484 and P2FIR cells with antibodies followed by Alexa Fluor® 488 conjugated secondary antibody staining revealed higher staining among all the five clones in FAMPAC-1 and B8484 cells. H1299 and P2FIR staining intensities were comparable to negative controls mouse IgG non-specific control or secondary antibody only (**Figure 2:2A and B**). Ratios of mean fluorescent intensities of FAMPAC-1 to H1299 and B8484 to P2FIR were computed (**Figure 2:2 C**). Clones 49A and 49A1/H12 had the highest ratios of 20.95 ± 4.92 and 87.261 ± 13.72 and 18.52 ± 4.74 and 82.42 ± 13.61, respectively. Antibody 49A was polyclonal mother clone and

was ruled out as potential candidate for further validation, thus enabling anti-p53 49A1/H12 mAb to be selected as the best antibody. However, its hybridomas were completely incapable of growing in FBS free CD Hybridoma Medium for antibody production. Consequently, anti-p53 49A1/H10 which had FAMPAC-1 to H1299 ratio of 17.01±4.05 and B8484 to P2FIR 52.48±9.13 emerged as the favourite candidate for large scale production and further validation.

2.4.1.3 Confocal microscopy

To further confirm the specificity of anti-p53 49A1/H10 mAb, we performed immunofluorescence staining and microscopy to evaluate the cellular localisation of the antibody. Anti-p53 49A1/H10 mAb signal was primarily seen in the nucleus and colocalised strongly with DAPI signal in FAMPAC-1, MiaPaCa-2 and HT1080 cells and not H1299 (**Figure 2:3**).

2.4.1.4 Anti-p53 49A1/H10 mAb binds to total p53

We performed a western blot to evaluate the specificity of anti-p53 49A1/H10 mAb on all forms of p53 (structural and contact mutants, and wild type). The results demonstrated that the antibody binds to MiaPaCa-2 (p53 contact mutant), FAMPAC-1 (p53 structural mutant) and HT1080 (p53 wild type) cell lysates. There were no non-specific p53 bands H1299 (**Figure 2:4**). These data confirmed that 49A1/H10 is a total p53 binder, hence the name anti-(total)-p53 49A1/H10 monoclonal antibody.

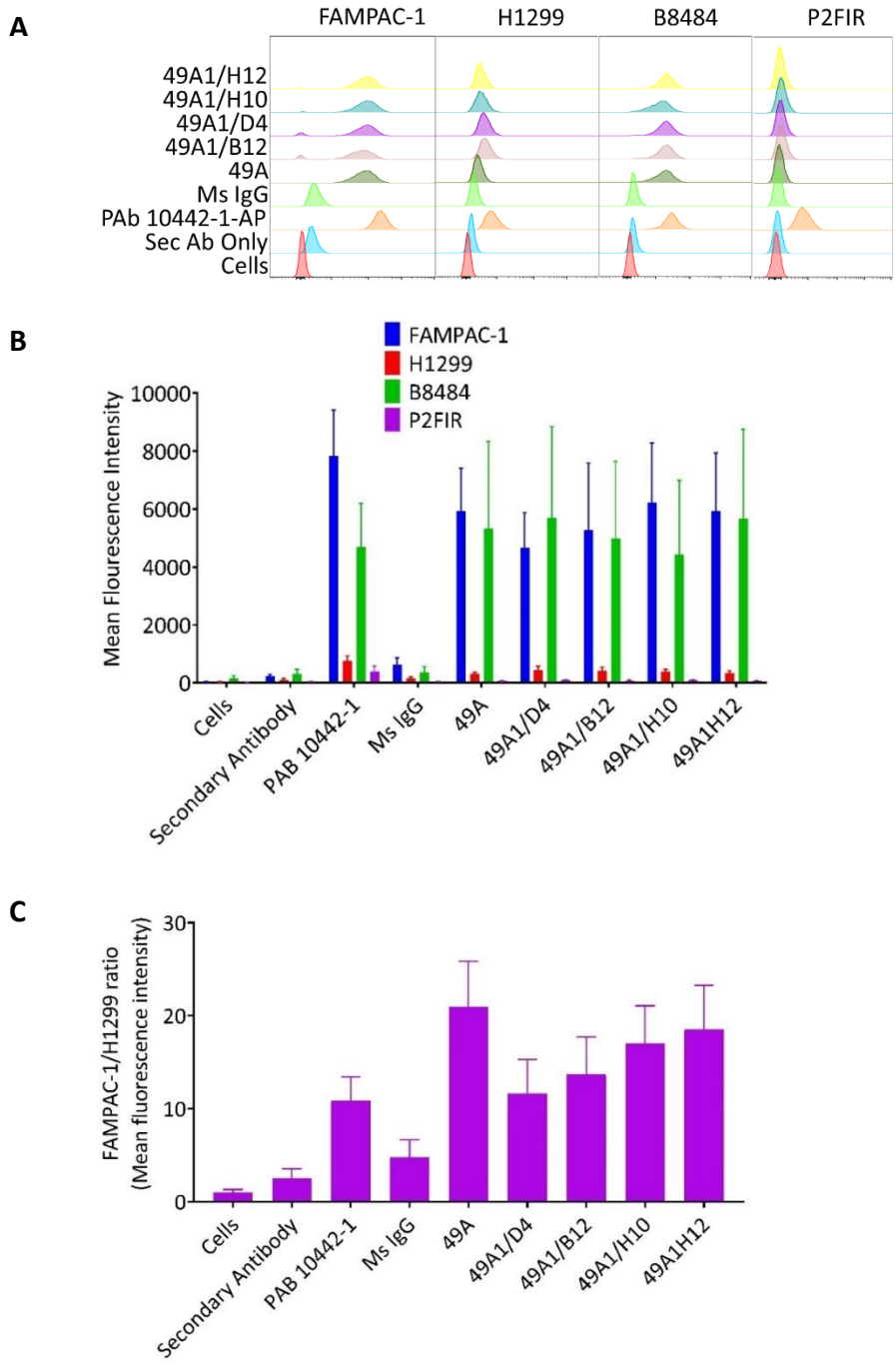


Figure 2:2) Flow cytometry validation of p53 antibodies. A) Histogram overlay plots depicting levels of p53 expression after staining cell with Alexa Flour 488 dye. **B)** Bar chats representation of mean fluorescence of p53 antibodies. **C)** Ratios of specific to non-specific antibody staining were calculated by dividing the mean fluorescence intensity of FAMPCA-1 by H1299 cells. Values and error bars represent mean ± SD from three independent experiments performed in triplicate.

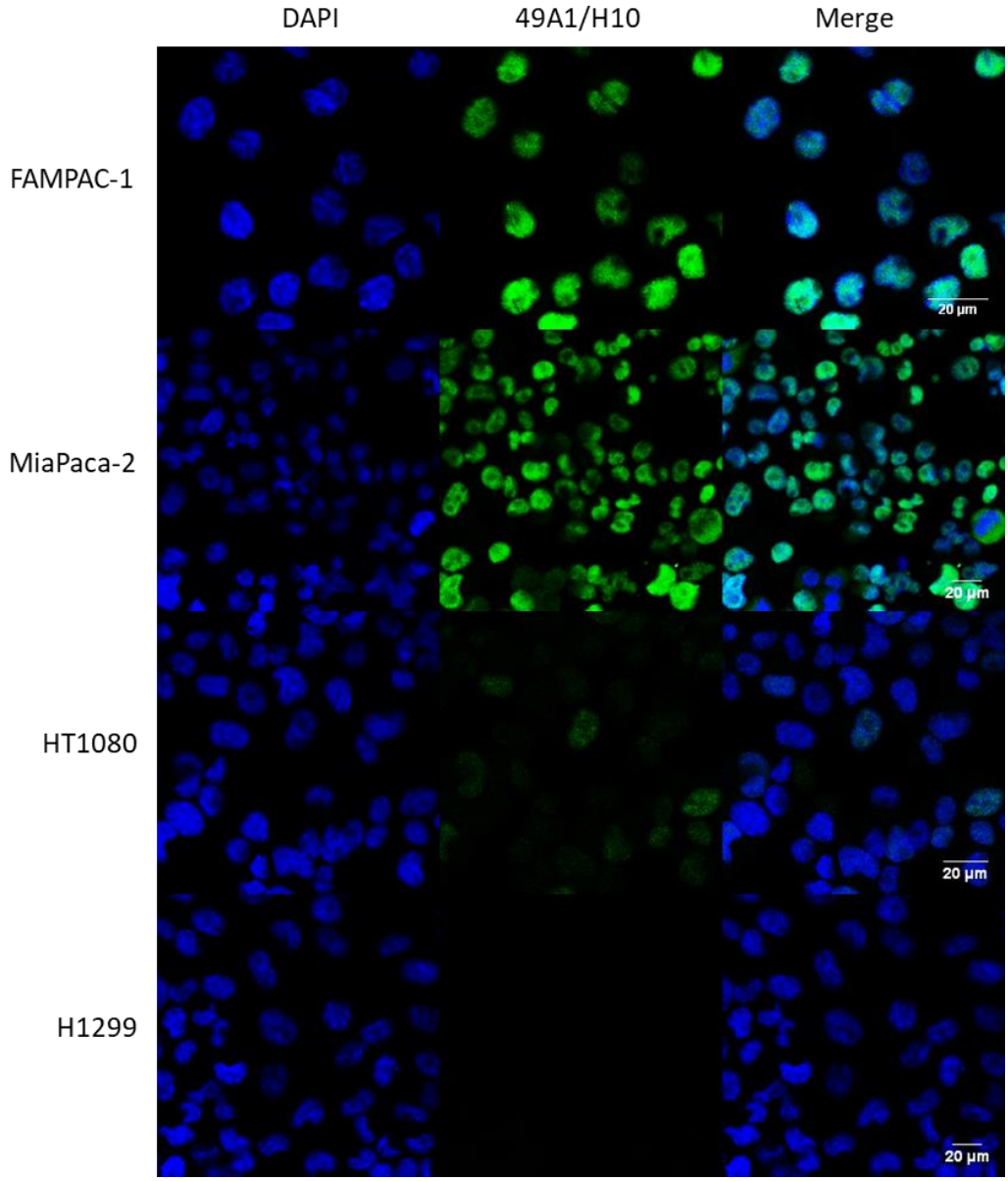


Figure 2:3) Anti-total p53 49A1/H10 mAb localisation in the nucleus. Immunofluorescence microscopy showing localisation of mutant and wild type p53 in the nucleus following incubation of fixed and permeabilised cells with anti-total p53 49A1/H10 mAb and staining with Alexa Fluor 488 secondary antibody.

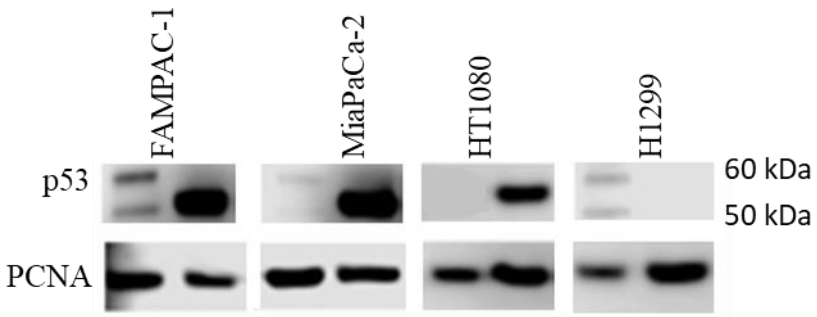


Figure 2:4) Immunoreactivity of anti-p53 (49A1/H10) mAb on total p53 protein. Western blot analysis of extracts from four cell lines expressing different p53 form, showing the antibody binds to total p53 protein. Full Western blot images are shown in **Figure 8:1B** in the appendix section.

2.4.1.5 Anti-p53 production and purification

The anti-(total)-p53 49A1/H10 mAb hybridomas were cultured for three weeks for antibody production. The supernatant was clarified and purified using protein liquid chromatography (FPLC). Approximately 8 mg of the antibody was collected and stored at -20°C in aliquots of 100 µg/100 µL PBS. The antibody identity and molecular weight were confirmed using both reducing and non-reducing SDS-PAGE. One band, approximately 150 kDa was observed after Coomassie blue staining of non-reducing SDS-PAGE gel (**Figure 2:5A**). Two bands, one approximately 25 kDa and the other 50 kDa were observed on the reducing SDS-PAGE gel (**Figure 2:5B**). Together, these assays confirmed that the purified protein was a monoclonal antibody weighing 150 kDa, which is the molecular weight of an intact monoclonal antibody. The 25 kDa and 50 kDa molecular weights represent the light and heavy chains, respectively, after reduction of interchain disulphide bonds.

2.4.1.6 Evaluation of antibody affinity by flow cytometry

The binding affinity of anti-(total)-p53 49A1/H10 mAb was analysed on fixed and permeabilised FAMPAC-1, MiaPaCa-2, HT1080 and H1299 cells using flow cytometry. Our

results revealed the antibody had nanomolar affinities (K_D values less than 1 nM): FAMPAC-1 K_D = 0.99±0.10 nM, MiaPaCa-2 K_D = 0.74±0.15 nM and HT1080 K_D = 0.31±0.12 nM (**Figure *2:6***).

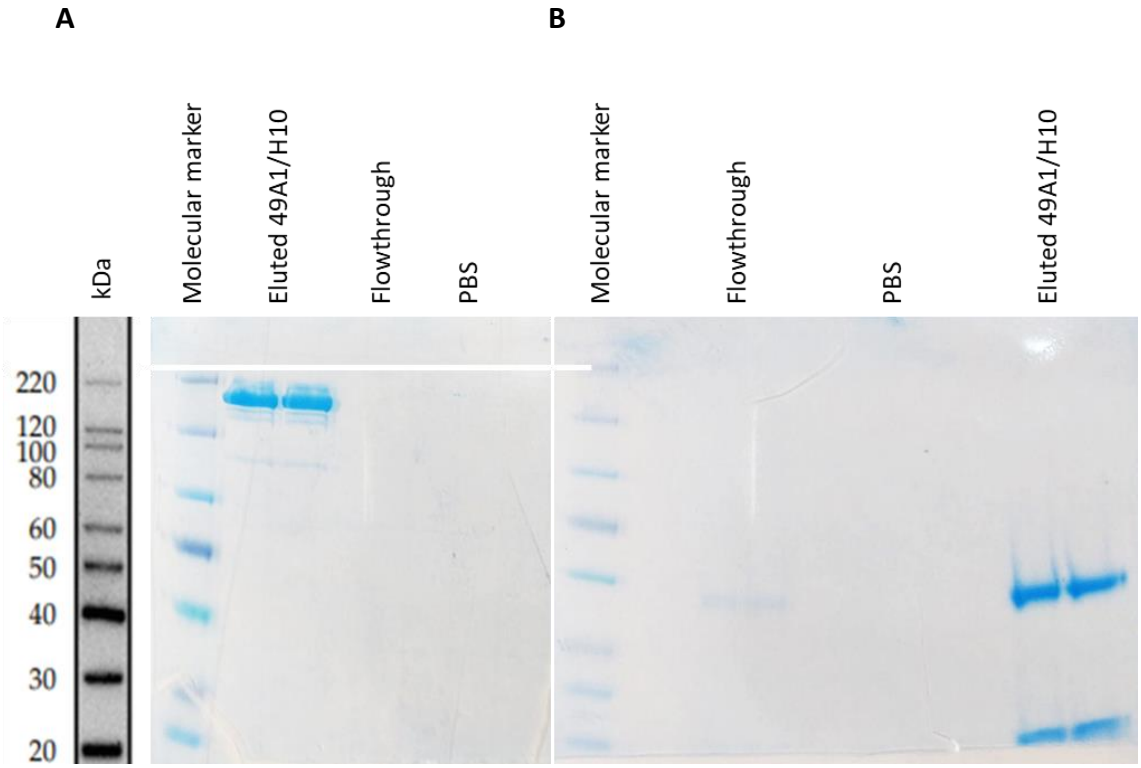


Figure 2:5) SDS-PAGE gel images of purified 49A1/H10 mAb. A) Under non-reduced showing only one band at about 150 kDa and **B)** reduced conditions showing two bands seen at about 50 and 25 kDa. Each sample was loaded on the gel in duplicate.

2.4.2 Evaluation of p53 protein levels in a panel of pancreatic cancer cell lines

2.4.2.1 Western blot analysis of p53 protein levels

We examined the expression levels of mutant p53 in four cell lines FAMPAC-1, MiaPaCa-2, BxPC-3, and PANC-1 in comparison to normal whole tissue pancreas lysate. The expression levels of p53 were first evaluated using Western blot (**Figure 2:7 A and B**). Mutant p53 relative levels in the four cell lines were found to be overly but variably overexpressed compared to normal pancreas tissue lysate, with MiaPaCa-2 cells showing the highest p53 levels.

2.4.2.2 Evaluation of protein levels by ELISA

The western blot results were corroborated by ELISA assay which showed that mutant p53 were significantly higher in FAMPAC-1, MiaPaCa-2, BxPC-3, and PANC-1 cells compared to normal pancreas tissue lysate ($p<0.0001$) (**Figure 2:7C**).

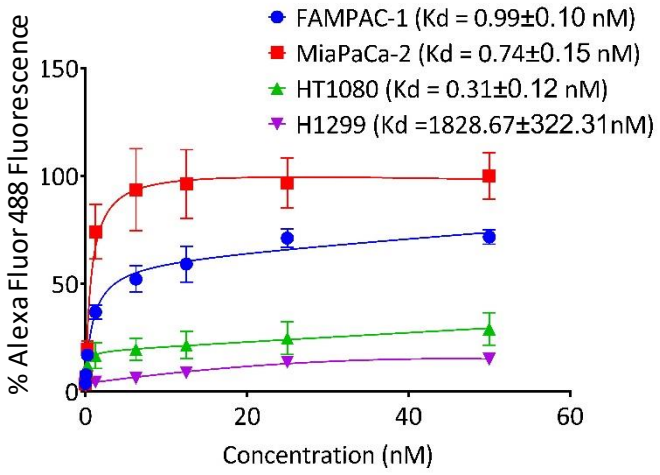


Figure 2:6) Analysis of 49A1/H10 mAb affinities using flow cytometry. The cells were incubated with anti-(total)-p53 49A1/H10 monoclonal antibody and stained with Alexa Fluor 488 dye conjugated secondary antibody. Fluorescence data was analysed and the k_D obtained by fitting the binding curves using GraphPad prism one site binding model.

The Human p53 ELISA Kit (BMS256) (Thermo Fisher, Scientific, UK) determines the p53 amount in Units/mL. MiaPaCa-2 cells had the highest p53 amount of 11.46±3.24 Units/mL per 1000,000 cells, while FAMPAC-1, BxPC-3 and PANC-1 amounts were 7.66±1.86, 5.70±2.22 and 8.34±1.83, respectively. The amount of p53 in normal human pancreas whole tissue lysate (HPWTL), AsPC-1 and blank control were 0.27±0.10, 0.09±0.04 and 0.17±0.10, respectively. Together, Western blot and ELISA data confirmed that p53 hotspot mutants are overexpressed in pancreatic cancer.

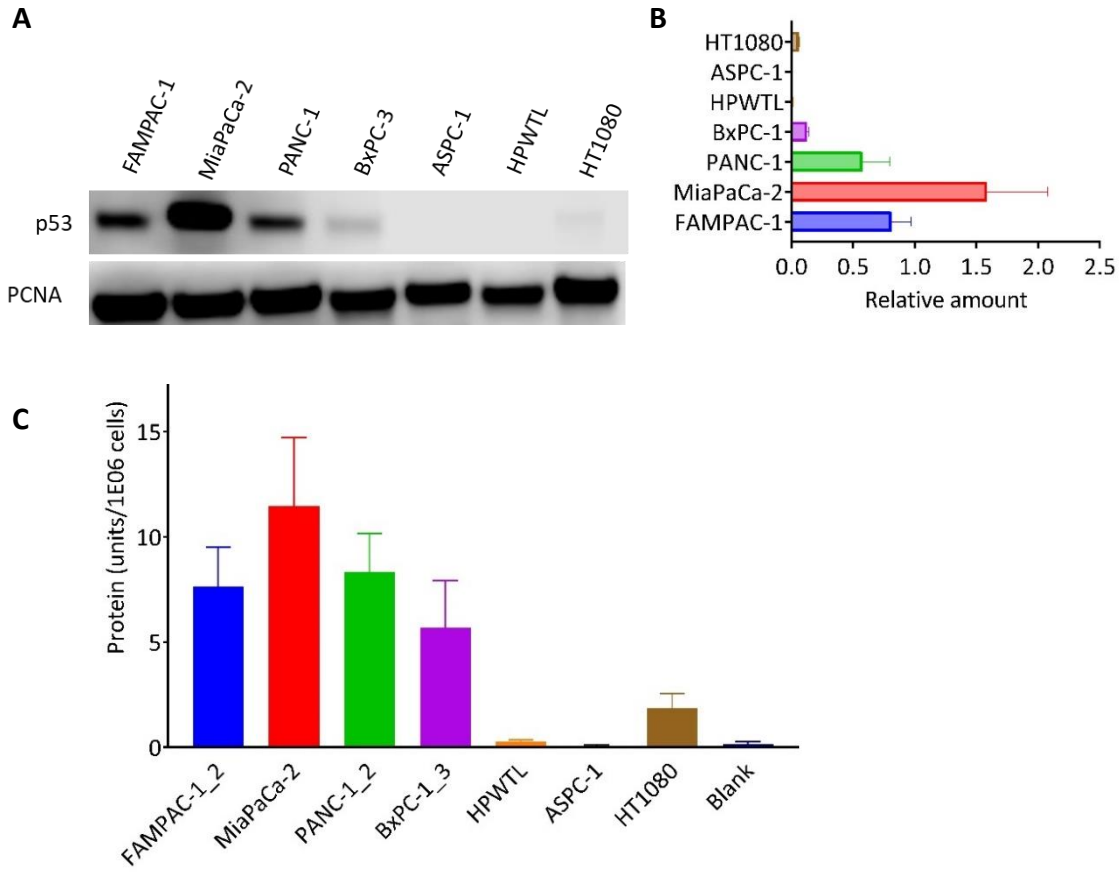


Figure 2:7) Quantification of p53 protein levels by Western blot and ELISA. A) Western blot p53 protein bands from whole cell lysates of PDAC cell lines and HT1080 cells. **B)** Bar graph representation of p53 protein levels quantified from protein bands and normalised to PCNA loading control. **C)** Quantification of p53 protein levels by ELISA. Concentration of p53 in units/mL from cell extracts of 10^6 cells. Values are mean $\pm$SD, from three independent experiments.

2.5 Discussion

Antibody-based therapeutics continue to impact the way patients are diagnosed in clinics. Central to the deployment of an antibody for clinical application are two important steps: the discovery and validation of a disease-specific biomarker and the production and validation of biomarker-specific monoclonal antibody possessing high specificity and affinity. A plethora of cancer biomarkers have been characterised and targeted for either diagnosis or treatment. However, most of the available biomarkers represent only a small subset of the cancers,

hence only a few patients can benefit from their therapeutic targeting. Nevertheless, the heterogeneity of cancer at cellular, tissue and patient levels make it hard to find a biomarker that homogeneously represent a particular cancer or cancers in general. There is therefore a dire need to continue characterising new therapeutic targets as well as develop targeted therapies for the existing ones.

A good biomarker must be exclusively overexpressed abnormally in cancer and not in healthy tissues, which makes it possible to contrast neoplastic cells from normal ones, as well as negate cross-reactivity of the therapeutic agents on health tissues which can result in unwarranted off-target toxicity. The high prevalence of TP53 mutations in invasive PanIN-3 lesions and PDAC, coupled to overexpression makes it a potential biomarker for molecular imaging. TP53 mutations are also absent in chronic pancreatitis which is often misdiagnosed as invasive PDAC by conventional imaging CT scan, MRI and [^{18}F]FDG PET. Thus, mutant p53 can help to contrast inconsequential non-invasive PDAC lesions from invasive ones. Nevertheless, mutant p53 overexpression in PDAC patients correlates with poor prognosis, making it a suitable prognosis biomarker for patients' treatment stratification (Casey et al., 1993; Koorstra et al., 2009).

Targeting of a disease specific biomarker for diagnosis require an imaging agent with high specificity and binding affinity. These two critical properties help to ensure high specific tumour accumulation and retention, resulting in high contrast between malignant and health tissues. Another important factor is the molecular size of the imaging agent, which determines the rate of tumour accumulation and clearance from the not-target tissues and the circulatory system. Small imaging agents such as peptides and affibodies have faster tumour accumulation rate and clearance from health tissues and blood. However, faster

pharmacokinetics profile can negatively affect tumour uptake due to faster clearance. Several imaging agents such as monoclonal antibodies and its derivative fragments, regulatory peptides analogues, small molecules and affibodies have already been employed to image cancer at preclinical level or in the clinic (Dammes & Peer, 2020; Sun et al., 2017; Tolmachev & Orlova, 2020). Of these, monoclonal antibodies represent the most researched and utilised therapeutics because of their excellent specificities and binding affinities and known pharmacokinetics/biodistribution profile. Monoclonal antibodies are produced via immunization of laboratory animals such and mice and rabbits with a specific antigen followed by antibody screening and fusion of splenocytes with myeloma cells to generate monoclonal antibody generating immortal hybridoma cells. While thousands of antibodies have been produced and validated by different research groups and biotechnology companies, most of them are bedevilled by the challenge of lack of reproducibility and poor specificity due to inadequate validation assays. It is important for researchers to confirm the properties of monoclonal antibodies before using them. In addition, basic science research projects that require large quantities of monoclonal antibodies can be challenging to complete due to the huge cost of commercially available antibodies. As a results, most researchers opt to produce and validate in-house antibodies for use their research works. The purpose of the chapter was to validate a new anti-total p53 monoclonal antibody interrogating p53 status in subsequent chapters as well as evaluate the expression of mutant p53 in PDAC cells.

In this work, we have demonstrated that mutant p53 is overexpressed in PDAC cells compared to normal tissue. We chose the four cell lines (MiaPaCa-2, BxPC-3, PANC-1, and FAMPAC-1) because they express p53 hotspot mutants that represent approximately 22% of all p53 mutants in PDAC (Cicenas et al., 2017). ELISA results using a commercially available Human

p53 ELISA kit demonstrated that mutant p53 among PDAC cell lines is significantly overexpressed compared to normal pancreas tissue (**Figure 2:7C**). The mutant p53 displayed heterogeneous levels of expression across the four cell lines. The high level of the mutant protein presents a suitable target for imaging as this will provide a contrast signal between tumour and normal tissues. The ELISA results were confirmed by Western blot results using our inhouse made 49A1/H10 p53 mAb (**Figure 2:7B**). In addition, the Western blot results (**Figure 2:7A**) confirmed the p53 specificity of the 49A1/H10 monoclonal antibody as it bound to all the mutants and wild type p53 cell lysates and not AsPC-1 cell lysates that are p53 null.

While these data demonstrated that all the p53 mutants are overly expressed, the p53 protein levels were variable across the four cell lines, and only four p53 mutant cell lines were used in these assays. Over 1000 TP53 mutations have been characterised with approximately 80% being point mutations yet only a few hotspot mutants (R248W, R273H and R175H0 have been the major focus of studies. The above mutants have been shown to be overexpressed in most cancers including PDAC, and the overexpression associated with tumour aggressiveness, therapy resistance and overall poor prognosis (Vogiatzi et al., 2016). There is a need for further evaluation of the expression status of p53 missense mutants across a broad panel of mutant p53 expressing cell lines and human tumour tissues. The p53 expression status should be correlated with cancer stage and patient's prognostic data in order to have clinically meaningful and instructive data. This will inform the scope and relevance of imaging mutant p53 among high-risk cancer population and patients.

In addition to evaluating the expression levels of mutant p53 as a biomarker for PDAC imaging, we also validated a new monoclonal antibody targeting total p53 protein. Selecting an antibody with high specificity and affinity is crucial when developing antibody-based

molecular imaging agents. While a plethora of commercially available anti-p53 mAbs are available on the market, our work required large quantities of p53 antibodies which would have been costly if purchased. We therefore considered validating a new antibody from hybridoma clones that were generated by our collaborator Professor Alison Banham, (NDCLS). The hybridoma clones were first validated for specificity using Western blots across a panel of murine and human cell lysates with different expression status. Western blot enables the qualitative evaluation of antibody specificity on denatured protein samples, with antibody reactivity confirmed by presence of protein bands marching its molecular weight on the protein ladder. Our results (**Figure 2:1**) showed that 5/8 antibody clones produced human and murine p53-specific protein bands with no cross-reactivity in p53-null cell lysates. Both the novel p53 antibodies and the positive control Rb 10442 PAb produced two band between 40 kDa and 50 kDa in FAMPAC-1 and MiaPaca-2 cells. This was, however, not shown murine p53 cells or HT1080 wild type cells (**Figure 2:4**). The two bands could potentially be one allele of mutated p53 with altered molecular weight (P53 Antibody (10442-1-AP) | Proteintech, n.d.). Western blot data was confirmed by flow cytometry which quantified the fluorescence intensities of the antibodies in p53 expressing cells relative to p53-null cells. The flow cytometry data (**Figure 2:2**) confirmed that the five antibodies were p53-specific with significant differences in the staining intensity in p53 positive cells compared to p53-negative cells. The best clone among the five was selected based on the ratio of fluorescent intensity in p53 positive to p53 null cells. Clones 49A1/H12 and 49A1/H10 emerged as the best candidates for large scale production and further validation, as they displayed higher ratios of specific to non-specific signal compared to the other antibodies except for 49A which had the highest ratio **(Figure 2.2C**). The reason for not selecting clone 49A as the best antibody

was because it is a polyclonal mother clone, yet we were interested in selecting a monoclonal antibody.

Antibody conjugation and *in vivo* assays require high purity levels. It is therefore imperative that during large scale antibody production, the hybridomas should be cultured in protein and FBS free media. Both 49A1/H12 and 49A1/H10 were cultured in CD Hybridoma Medium (Life Technologies) for large scale production and purification. However, clone 49A1/H12 failed to grow and adapt in both normal RPMI-1640 media containing FBS and in CD Hybridoma Medium. This problem could be due to chromosomal loss in these hybridomas which can be induced during the fusion of splenocytes and myeloma cells. We therefore proceeded to grow and produce large quantities of clone 49A1/H10. A pure monoclonal antibody can be confirmed using both reducing and non-reducing SDS-PAGE. Monoclonal antibodies are 150 kDa proteins composed of two-50 kDa identical heavy polypeptide chains and two-25 kDa identical polypeptide chains that are connected by disulphide bonds. A purified intact antibody produces a single 150 kDa molecular band after non-reducing SDS PAGE and 50 kDa band and 25 kDa protein bands after a reducing SDS-PAGE assay. Our results (**Figure 2:5**) confirmed this following the purification of harvested 49A1/H10 antibody.

To further validate purified clone 49A1/H10, we performed a western blot to evaluate its specificity of mutant and wild type p53 protein. Our data (**Figure 2:4**) confirmed that this antibody is a total-p53 binding antibody. Both wild-type and mutant p53 have been shown to be overexpressed in neoplastic tissues while normal tissues express low level of p53 (Sugrue et al., 1997). We required a monoclonal antibody that bound to total p53 so to enable assessment of expression levels of mutant and wild type p53 in tumours compared to normal tissues. Visualising the cellular location of an antibody is also an important antibody validation

strategy. We employed confocal microscopy to visualise the subcellular localisation of anti-total p53 (49A1/H10) mAb in FAMPAC-1 MiaPaCa-2, HT1080 and H1299 cells. Both wild type and mutant p53 are majorly expressed in the nucleus of cells. Immunocytochemistry results (**Figure 2:3**) showed anti-total p53 (49A1/H10) mAb staining in the nucleus of FAMPAC-1 MiaPaCa-2 and HT1080 and not in H1299.

The mAb binding affinity is very important in the retention of an imaging agent in tumours enabling a high contrast with health tissues. Monoclonal antibodies with nanomolar or picomolar affinities provide excellent binding kinetics for therapeutic application. We determined the affinity of anti-total p53 (49A1/H10) mAb on both wild type and two forms for p53 mutants using flow cytometry. The antibody displayed approximately same dissociation constant in nanomolar range (**Figure 2:6**). The use of human p53 N-terminal peptide amino acids 13-27 (PLSQETFSDLWKLLP) might explain the similarity in affinities in both two mutant forms and wild type p53. This region is highly conserved in mammals and less mutable, thus maintaining the near native conformation in both wild type and mutated p53 protein. The nanomolar affinity of the anti-total p53 (49A1/H10) mAb makes it an excellent targeting molecule for further modification into a molecular imaging agent.

2.6 Conclusion

This work has established evidence of overexpression of mutant p53 protein in approximately 22% of all p53 mutants in PDAC tumours. The high levels of abnormal p53 in PDAC relative to normal pancreas tissues qualify mutant p53 as a potential biomarker for PDAC imaging *in vivo*. Our subsequent work will focus on attempting to image mutant and wild type p53 in mouse xenografts. We have also validated a novel anti-total p53 (49A1/H10) mAb with high binding specificity and nanomolar affinity. This antibody will be modified with a HIV-1 TAT cell

penetrating peptide (CPP-TAT) and radiolabelled with indium-111 radionuclide for use as a SPECT imaging tracer for interrogating p53 expression status in mouse xenografts.

3 Chapter 3 – Synthesis of RICs and *in vitro* validation

3.1 Introduction

Molecular PET and SPECT represent the most advanced imaging modalities for disease diagnosis, patients' treatment stratification and assessment of treatment response. These imaging techniques possess target sensitivity of up to picomolar range and are capable of non-invasive whole-body imaging, making them suitable for detection of the earliest molecular abnormalities preceding invasive cancer development as well as detection of all neoplastic lesions across the human body. The use of molecular imaging techniques requires the administration of a targeting molecule that interacts with disease-specific biomarkers coupled to a radionuclide that emit a signal detectable by the PET or SPECT camera. Several targeting molecules with varying binding kinetics and pharmacokinetics profiles have been developed including monoclonal antibodies and their small fragments derivatives, affibodies, peptides and small molecules. The choice of a radionuclide is determined by the type of imaging modality; gamma-emitting radionuclides for SPECT and positron emitting radionuclides for PET, and the pharmacokinetics properties of the targeting molecule (James & Gambhir, 2012).

Because of their excellent binding kinetics and long residence time in blood that result in high uptake and retention in tumours, monoclonal antibodies represent the most favourable biologics for cancer imaging. Monoclonal antibodies have been heavily exploited in cancer for early diagnosis and prognosis evaluation of patients using PET and SPECT imaging (Dammes & Peer, 2020). For a monoclonal antibody to qualify as a PET/SPECT imaging agent, it must be conjugated to a chelator and subsequently radiolabelled with a radionuclide. Conventional antibody imaging agents are limited to detection of cell surface markers. Many cancer-induction changes occur within the cell and are therefore inaccessible to target using

antibodies. However, modification of antibodies with a cell penetrating peptide (CPP) help to overcome both the cell and nuclear membrane barriers and target intracellular biomarkers. Both the chelator and the CPP are conjugated to the antibody via reactive natural or engineered amino acid residues. It is imperative that a conjugation method/protocol that does not severely alter the antibody's binding affinity and immunoreactivity is utilised. The most commonly used conjugation method is the carbodiimide crosslinking chemistry, that involves the reaction of the mAb carboxylic residues with EDC/NHS to form an amine reactive O-acylisourea intermediate (Khorana, 1953). The activated antibody is reacted with the N-terminal group of the CPP, resulting in mAb-CPP conjugates. The mAb-CPP conjugates are then reacted with amine reactive bifunctional chelator for instance S-2-(4-isothiocyanatobenzyl)-diethylenetriamine pentaacetic acid (p-SCN-Bn-DTPA) for radionuclide labelling. This method suffers from several limitations including inability to control conjugation of the CPP to specific mAb carboxylic groups (Aspartic acid, glutamic acid, or C-terminal group) and production of heterogeneous conjugates due to potential for mAb amine reactive O-acylisourea Intermediate reacting with amines on other mAbs rather than CPP, or p-SCN-Bn-DTPA reacting with primary amine residues on CPP instead of the antibody. As a result, RICs with different pharmacokinetics profiles are produced which affects both *in vitro* and *in vivo* performance. The method is thus prone to low quality RICs and batch-batch variation.

The Cornelissen group at Oxford developed a novel antibody-conjugation method based on the copper-free strain-promoted azide-alkyne cycloaddition (SPAAC) reaction (Veal et al., 2021). The new method referred to as DBCO-azide (DBCO-N_3) method involve the reaction of mAb lysine residues with a known amount of the bifunctional conjugation agent, dibenzocyclooctyne-4- sulfo-2,3,5,6-tetrafluorophenol ester (STP-DBCO) (Click Chemistry

Tools, AZ, USA). The mAb-DBCO conjugate is then reacted with known amount of CPP-TAT – azidohomoalanine (Cambridge Peptides, UK) and DTPA azide chelator (N_3-Bn-DTPA) (Department of Chemistry, University of Oxford, UK). Both mAb and DBCO can be quantified at absorbance 280 nm and 309 nm, respectively, making it possible to quantify the nanomoles of STP-DBCO conjugated to the mAb, and provide better control of the CPP/chelator to mAb ratio. The whole reaction can take place at RT in less than 8 h.

In this project, I set out to conjugate the anti-total-p53 (49A1/H10) mAb with CPP-TAT and DTPA chelator, and radiolabel with indium-111 radionuclide using the DBCO-N_3 method described above. The anti-total-p53 (49A1/H10) and Mouse IgG non-specific control RICs will be evaluated for radiochemical purity, stability in serum, binding kinetics, and cellular uptake. The specificity of the anti-total-p53 (49A1/H10) RICs on p53 protein will be evaluated *in vitro* in MiaPaCa-2, HT1080 and H1299 cells. This chapter presents the results of the *in vitro* characterisation of RICs. The results will determine whether the RICs qualify for *in vivo* imaging of p53 in mouse xenografts using SPECT/CT.

3.2 Material and methods

3.2.1 Conjugation od STP-DBCO on 49A1/H10 mAb via click chemistry

Anti-total p53 (49A1/H10) mAb or Mouse (G3A1) mAb IgG1 Isotype Control (Cell Signalling Technology, UK) (200 µg each) were buffer exchanged with 0.1 M $NaHCO_3$ pH 8.5 on an amicon ultra-0.5 centrifugal Filter 100 kDa MWCO (Sigma-Aldrich, UK) by centrifuging at 12,000 x g for 3 x 4 min to a final concentration of ≥5 mg/mL. Antibodies were then reacted with a 7-fold molar excess of dibenzocyclooctyne-4-sulfo-2,3,5,6-tetrafluorophenyl (STP-DBCO) (Click Chemistry Tools, USA) pre-dissolved in dimethyl sulfoxide (DMSO) at RT for 4 h. The reaction products were purified, and buffer exchanged to PBS by centrifuging at 1500 × g

in a Zeba Spin desalting column (40 K MWCO, 0.5 mL) (Thermo Fisher Scientific, USA). The DBCO to antibody ratio was determined by measuring the absorbance of the antibody (280 nm) and DBCO (309 nm) using the NanoDrop™ One Microvolume UV-Vis Spectrophotometers (Thermo Fisher Scientific, USA).

3.2.2 Bioconjugation of anti-p53 49A1/H10 Monoclonal antibody

The antibody-DBCO conjugates were reacted with a 2-fold molar equivalent relative to DBCO molecules of 3.4 mM N_3-Bn-DTPA pre-dissolved in PBS + 20% DMSO (synthesised by Deborah Sneddon, Department of Chemistry, University of Oxford, UK), and, concurrently, a 1-fold molar equivalent, also relative to DBCO, of 1 mM azide-tagged cell penetrating peptide TAT-azidohomoalanine (TAT-N_3, GRKKRRQRRRPPQGYG-hA(N_3) pre-dissolved in PBS (Cambridge Peptides, UK) at 4°C for 16 h. The reaction product was purified, and buffer exchanged to 0.5 M sodium citrate pH 5.5 to remove unreacted products using centrifugal filtration in a Zeba Spin desalting column (40 K MWCO, 0.5 mL) (Thermo Fisher Scientific, USA). The TAT-antibody-DTPA conjugate was quantified by reading the absorbance of the antibody and DBCO at 280 nm and 309 nm, to determine the extent of unreacted DBCO relative to the antibody concentration.

3.2.3 Radiolabelling of DTPA-Bn-49A1/H10-TAT conjugates with [^{111}In]Cl3

For *in vitro* assays, 1 µg of each antibody was separately radiolabelled with 0.1 MBq of indium-111 chloride ([^{111}In]Cl_3). Aliquots of DTPA-Bn-IgG-TAT conjugates (100 – 200 µg) in 0.5 M sodium citrate pH 5.5) were reacted with [^{111}In]Cl_3 (Perkin Elmer, USA) for 1 h at RT. The radiochemical yield was determined by instant thin layer chromatography (iTLC). For radiolabelling yields below 95%, the RIC product was purified to remove any unreacted

[^{111}In]Cl_3 by buffer exchange with PBS using centrifugal filtration in a Zeba Spin desalting column (100 kDa MWCO, 0.5 mL) (Thermo Scientific, USA).

3.2.3.1 Quality control by iTLC

iTLC strips (5 mm x 100 mm) impregnated with salicylic acid (Agilent Technologies, USA) were used as a stationary phase and freshly prepared 50 mM EDTA buffer (pH 7) was applied as the mobile phase. Aliquots of RICs (2 µL) were separately spotted on the strips (10 mm above the baseline) and dipped in the 50 mM EDTA buffer to run for approximately 7 min until the solvent front was 80 – 90 mm from the baseline. The radiochemical yield was calculated by measuring area under the curve of baseline peak relative to free indium-111 in the solvent peak using a radio-TLC AR-2000 imaging scanner (Eckert & Ziegler, Germany).

3.2.3.2 *In vitro* stability in serum

RICs were diluted in 250 µL of PBS or normal mouse serum (Abcam, UK) to a final concentration of 0.25 µg/mL and incubated at 37°C for 24 h, 48 h and 72 h. Aliquots of PBS or serum (2 µL) were taken after each incubation period and spotted on the iTLC strips (10 mm above the baseline) and dipped in the 50 mM EDTA buffer to run for approximately 7 min until the solvent front is 80 – 90 mm from the baseline. The radiochemical yield was calculated as described above (**Section 3.2.3.2**).

3.2.3.3 Effect of [^{111}In]-DTPA-Bn-49A1/H10-TAT on cell viability

MTT and clonogenic assay were used to evaluate the non-target related toxicity of RICs on MiaPaCa-2, HT0180 and H1299 cells. For MTT assays, each cell line was seeded in 100 µL media in triplicates on a 96-well F-bottom plate and incubated overnight in 5% CO_2 incubator at 37°C. The media was removed and refreshed with fresh culture medium containing either [^{111}In]-DTPA-49A1/H10-TAT (1.5 nM, 1 MBq/µg), native 49A1/H10 mAb (1.5 nM), or PBS

Control. The plates were incubated for 1 h to allow for intracellular uptake of RICs. The media containing residual RICs was aspirated, and cells replenished with fresh media, and further incubated for 72 h at 37°C. The media was removed, plate washed with PBS, and refreshed with 100 µL fresh media containing 0.5 mg/mL MTT reagent. The plates were incubated for 3 h at 37°C. The MTT solution was discarded and 200 µL of DMSO added, followed by incubation at 37°C for 2 h. The plates were taken in the Tecan infinite M200 pro plate reader (Life sciences, UK), shaken for 3 min to solubilize the purple crystals and the absorbance values were measured at 565 nm. The results were used to calculate percentage cell viability.

For clonogenic assays, MiaPaCa-2 (250 cells/well), HT1080 (250 cells/well) and H1299 (125 cells/well) cells were seeded overnight on 6-well plates in a 5% CO_2 incubator at 37°C. The media was removed and refreshed with media containing either [^{111}In]-DTPA-49A1/H10-TAT (1.5 nM, 1 MBq/µg), native 49A1/H10 mAb (1.5 nM), or PBS Control and incubated further for 1 h. The media containing the unbound RIC was removed and cells washed three times with sterile PBS and fresh media added. The plates were incubated further for 12 days to allow for colonies to form. The supernatant was removed, and the plates washed 3x with PBS. Colonies were stained with a crystal violet biological stain (Sigma-Aldrich, MO, USA) at RT for 24 h. The plates were washed with tap water and dried for 24 h before colonies were imaged and counted using the GelCount™ colony counter (Oxford Optronics, Oxfordshire, UK).

3.2.4 *In vitro* cell uptake of radioimmunoconjugates

Aliquots of 1 x 10^5 cells/well were plated in a 24 well plate cell culture dishes and incubated overnight for adherence. The culture medium was removed, wells were washed with sterile PBS and 500 µL of fresh media containing RICs (1.5 nM, 1 MBq/µg) and incubated at 37°C for a further 1 h. The supernatant containing unbound RICs was removed and collected, and the

cells washed 2x with PBS which was also added to the collected unbound RIC portion. Cells were incubated for 5 min with ice cold n 0.1 M glycine pH 2.5 solution to remove and collect membrane-bound RIC. Cells were then lysed with ice cold 0.1 M NaOH to collect the intracellular bound RIC portion. Relative amount of indium-111 activity in the unbound, membrane-bound, and intracellular bound RICs were determined using Wizard^2 2480 automated gamma counter (Perkin Elmer, USA).

3.2.5 *In vitro* retention of radioimmunoconjugates

Cellular retention of RICs was evaluated in MiaPaCa-2, HT1080 and H1299 cells. Aliquots of 1 x 10^5 cells/well were plated in 24 well plate cell culture dishes and incubated overnight to allow the cells to adhere. The culture medium was removed, the cells washed with sterile PBS and 500 µL of fresh media containing RICs (1.5 nM, 1 MBq/µg) added and incubated further at 37°C for 1 h. The unbound, membrane-bound, and intracellular bound RICs for initial time point (o h) were collected and indium-111 activity counted using the gamma counter. For incubation time points 15 min, 30 min, 1 h, 2 h, 4 and 6h, the media was removed, and cells washed with 500 µL PBS, and media replenished and further incubated. After every incubation, the unbound, membrane-bound, and intracellular bound RICs were collected and the amount of indium-111 activity determined as described above (**Section 3.2.4**).

3.2.6 Immunoreactivity of DTPA-Bn-49A1/H10-TAT

Western blot was performed as previously described (**Section 1.2.2**), on FAMPAC-1, HT1080 and H1299 lysates to determine effect of TAT and DTPA conjugation on the immunoreactivity of antip53 49A1/H10 mAb. The relative protein bands densities of DTPA-Bn-49A1/H10-TAT were compared to those produced by the non-modified anti-total p53 49A1/H10.

3.2.7 Cell-based competitive radioimmunoassay

Aliquots of 1 x 10^5 cells/well were plated in a 48 well plate cell culture dishes and incubated overnight to allow for cells adherence. The culture media was removed, cells washed with PBS and fixed with 4% (w/v) paraformaldehyde for 10 min at RT. Cells were washed again with PBS and then permeabilised with Triton X-100 in PBS (1% v/v) for 20 min. Non-specific binding was blocked with 250 µl RIA blocking buffer (RIA wash buffer (PBS + 0.05% Tween®-20) + 2% BSA) for 1 h at RT. The cells were washed again with 250 µl RIA washing buffer. Cells were incubated with increasing concentrations (0 - 75 nM) of native anti-total p53 49A1/H10 mAb or DTPA-Bn-49A1/H10-TAT in 250 µL RIA blocking buffer for 1 h at RT with gentle rocking. Cells were washed with 250 µl RIA washing buffer followed by addition of [^{111}In]-DTPA-49A1/H10-TAT (2 nM) in 250 µL RIA blocking buffer per well and incubated for 1 h. The solution containing unbound [^{111}In]-DTPA-49A1/H10-TAT was collected before washing again with PBS. The cells were incubated for 5 min with ice cold glycine solution (0.1 M, pH 2.5) to remove and collect the membrane-bound [^{111}In]-DTPA-49A1/H10-TAT. Cells were then lysed with 250 µL ice cold NaOH (0.1 M) to collect the intracellular bound [^{111}In]-DTPA-49A1/H10-TAT. The amount of [^{111}In]-DTPA-49A1/H10-TAT collected from each well was determined using the Wizard2 2480 automated gamma counter (Perkin Elmer, USA) and the IC50 for native anti-total p53 49A1/H10 mAb and DTPA-Bn-49A1/H10-TAT was calculated.

3.2.8 Statistical analysis

All experiments were carried out at least in triplicate and presented as mean ± one standard deviation unless otherwise stated. GraphPad Prism v8 (GraphPad Software, CA, USA) was utilised in statistical analysis of all data.

3.3 Results

3.3.1 Radioconjugation of Anti-total p53 (49A1/H10) and MIgG mAb with TAT and indium-111

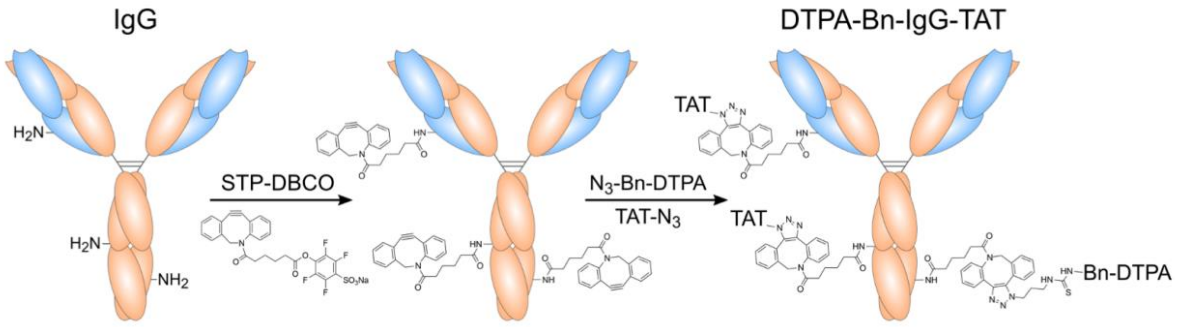


Figure 3:1) DBCO-N_3 monoclonal antibody radioconjugation method. The first reaction occurs at RT for 4 h followed by DTPA and CPP conjugation at 4°C overnight. The last reaction involves radiolabelling with indium-111 radionuclide at RT for 1 h.

The conjugation of TAT to Anti-total p53 (49A1/H12) and Mouse IgG nonspecific control, and subsequent radiolabelling with indium-111 was carried out using the strain promoted azide alkaline cycloaddition click reaction via DBCO-N_3 method (**Figure 3:1B**). The initial optimisation reaction aimed to achieve DBCO:IgG ratio of 4-5, which represent the number of STP-DBCO molecules attached to the mAb. Our data showed that we achieved a DBCO:IGG ratio of 5.0 ± 0.25 for DBCO-to-49A1/H10 and 4.87 ± 0.47 for DBCO-to-MIgG, with no statistical difference between the two antibodies p=0.5561 (**Figure 3:2B**). The radiolabelling efficiencies of the initial optimisation experiments was determined by ITLC with 98% and 99% radiochemical purity achieved for [^{111}In]-DTPA-MIgG-TAT and [^{111}In]-DTPA-49A1/H10-TAT, respectively (**Figure 3:2A**). For subsequent *in vitro* assays, a 95% radiochemical purity of either of the RIC was used without further purification. For *in vivo* applications, the radioconjugated antibodies were purified using centrifugal filtration in a 0.5 mL 100 kDa MWCO Zeba Spin desalting column to remove any residual indium-111 or [^{111}In]-DTPA molecules.

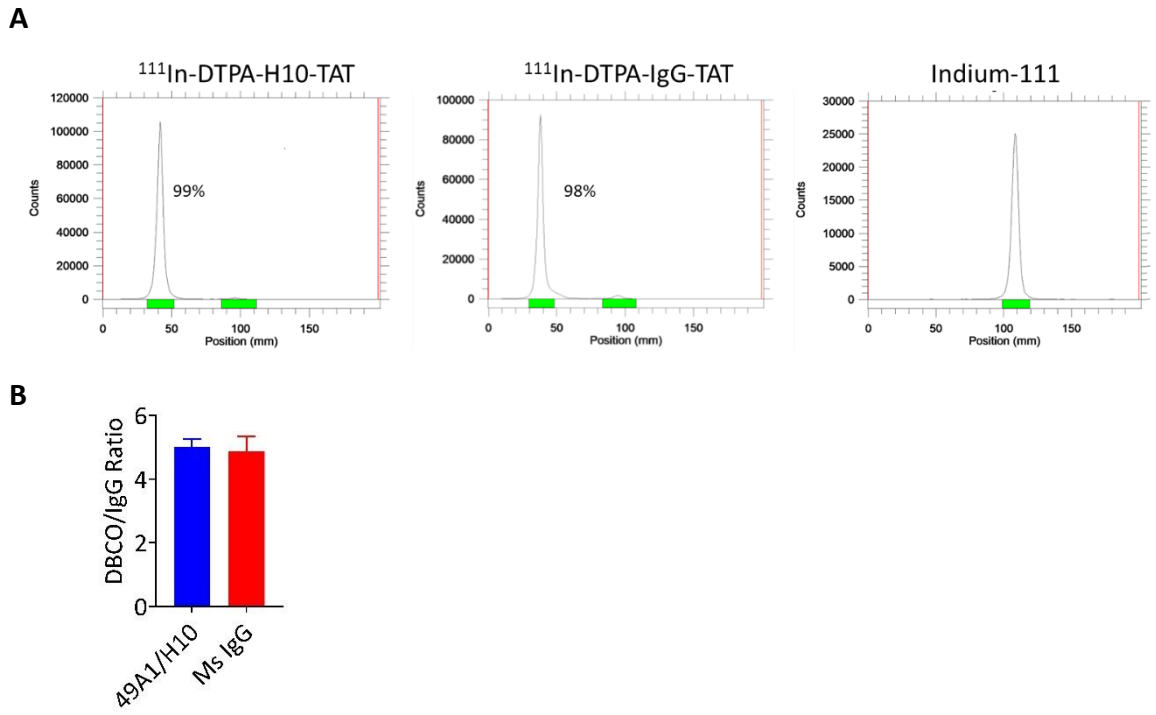


Figure 3:2) Radiochemical yield of RICs. A) ITLC of [^{111}In]-DTPA-49A1/H10-TAT and [^{111}In]-DTPA-MIgG-TAT and pure indium-111 after radiolabelling reactions. **B)** The DBCO/IgG ratios depicting the average number of DBCO attached to the antibody. Values and error bars are mean ± SD from 5 independent experiments.

3.3.2 *In vitro* stability of [^{111}In]-labelled antibodies

The stability of the newly synthesised RICs were evaluated in PBS (storage conditions) and in serum at 37°C (*in vivo* conditions). The [^{111}In]-DTPA-49A1/H10-TAT was incubated in PBS or mouse serum at 37°C for up to 72 h. The analysis of the samples after each incubation period by ITLC demonstrated that the stabilities of [^{111}In]-DTPA-49A1/H10-TAT in PBS and serum at 72 h were 82.5±0.98% and 79.2±1.2%, respectively (**Figure 3.3**). The rate of indium-111 loss from the antibody was 5.8%/day and 6.9%/day in PBS and serum, respectively. These results demonstrate that the indium-111 and DTPA chelator stay stably conjugated on the antibody across a 72-h period, which is sufficient to allow for tumour accumulation, clearance from non-target tissues and imaging using SPECT/CT.

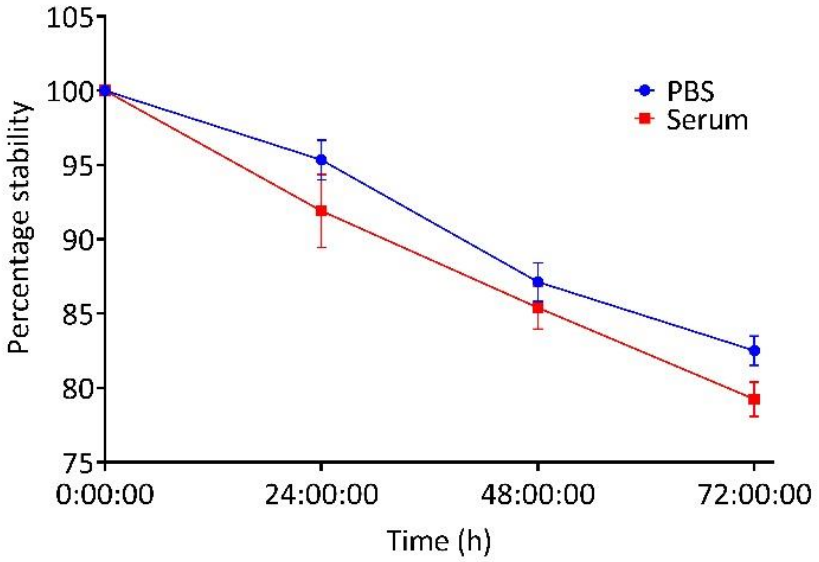


Figure 3:3) Stability of [^{111}In]-DTPA-49A1/H10 in PBS and serum. A) Graph showing percentage purities of the antibody in PBS or serum as a surrogate for stability in storage and *in vivo* conditions as determined by iTLC.

3.3.3 Immunoreactivity of [^{111}In]-labelled anti-total p53 (49A1/H12)

We compared the specificity of [^{111}In]-labelled anti-total p53 (49A1/H10) with its native counterpart anti-total p53 (49A1/H10) using Western blot on total p53 cell lysates: FAMPAC-1 (mutant p53), HT1080 (wild type p53) and H1299 (p53-null). As shown in (**Figure 3:4A**), both native and radioconjugated antibodies bound specifically to FAMPAC-1 and HT1080 lysates, with no non-specific signal observed in H1299 lysates. There was no statistical difference in the relative protein bands areas between the two antibodies in FAMPAC-1 and HT1080 lysates p values = 0.94 and 0.91, respectively (**Figure 3:4B**).

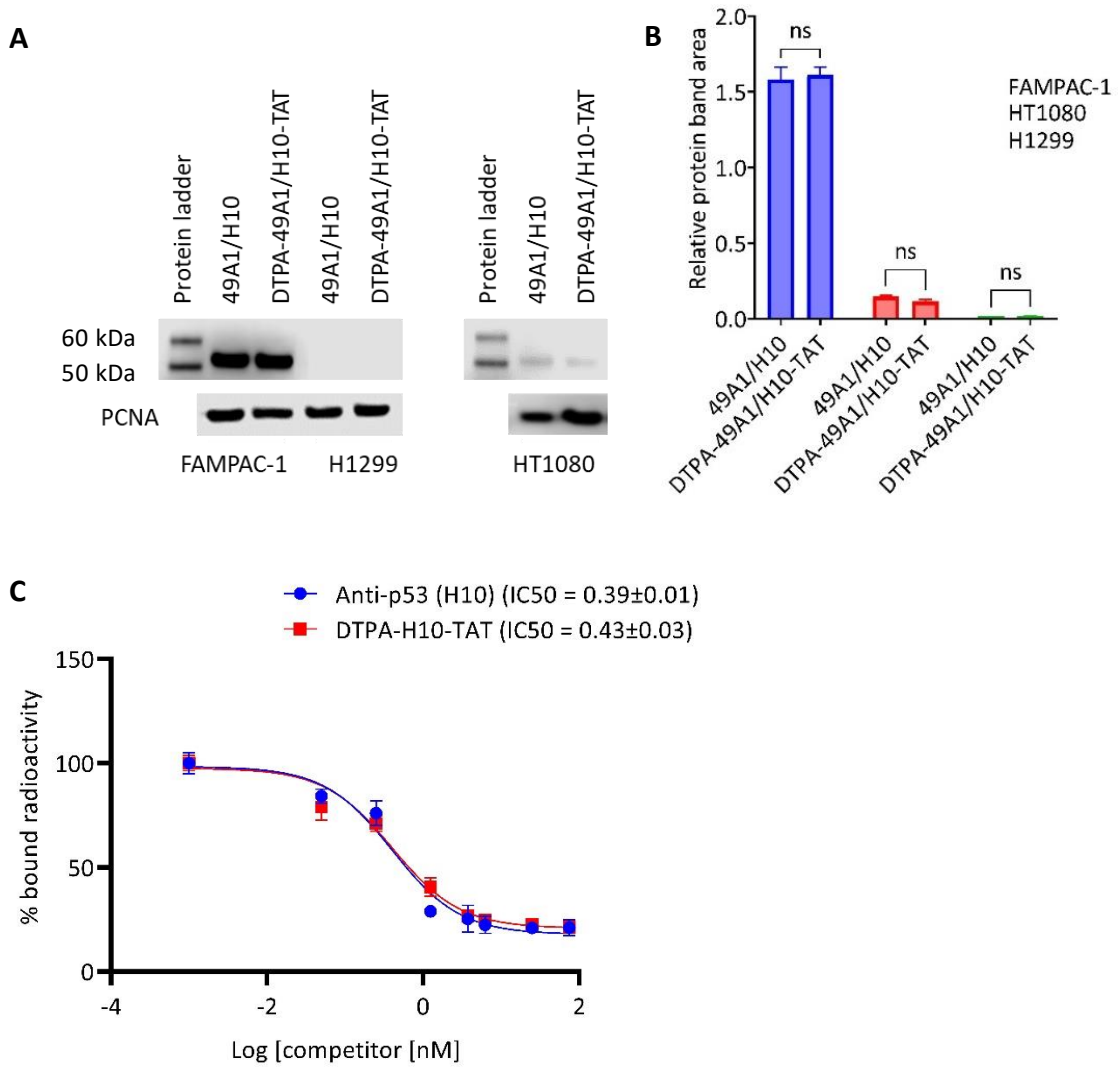


Figure 3:4 Immunoreactivity of [^{111}In]-DTPA-49A1/H10-TAT. A) Western blot analysis of the binding specificity of the antibody on mutant and wild type p53 cell extracts. **B)** protein band quantification relative to PCNA loading control. **C)** Radioimmunoassay blocking comparison of p53-based RICs. Values and error bars are mean ± SD from 3 independent experiments (ns – not significant).

3.3.4 Comparison of blocking properties of [^{111}In]-labelled Anti-total p53 (49A1/H12)

The effect of radioconjugation on the binding affinity of anti-total p53 (49A1/H10) was evaluated using a cell-based competitive radioimmunoassay (RIA) (**Figure 3:4C**). The RIA results showed that there was no statistically significant difference (p value = 0.98) between

the blocking potential of native anti-total p53 (49A1/H10) (IC_{50} = 0.39±0.01 nM) and DTPA-49A1/H10-TAT (IC_{50} = 0.42±0.03 nM).

3.3.5 *In vitro* cell toxicity of [^{111}In]-labelled antibodies

It is critical to evaluate the cytotoxic potential of the radioconjugated antibody before further *in vitro* and *in vivo* applications. We chose MTT assay to evaluate the effects of both radioconjugated anti-total p53 (49A1/H10) mAb and MIgG on MiaPaCa-2, HT1080 and H1299 cells after 72 h incubation with RICs. Both the [^{111}In]-DTPA-49A1/H10-TAT and [^{111}In]-DTPA-MIgG-TAT showed no statistically significant difference on the percentage cell viability in the three cell lines (**Figure 3:5A and B**).

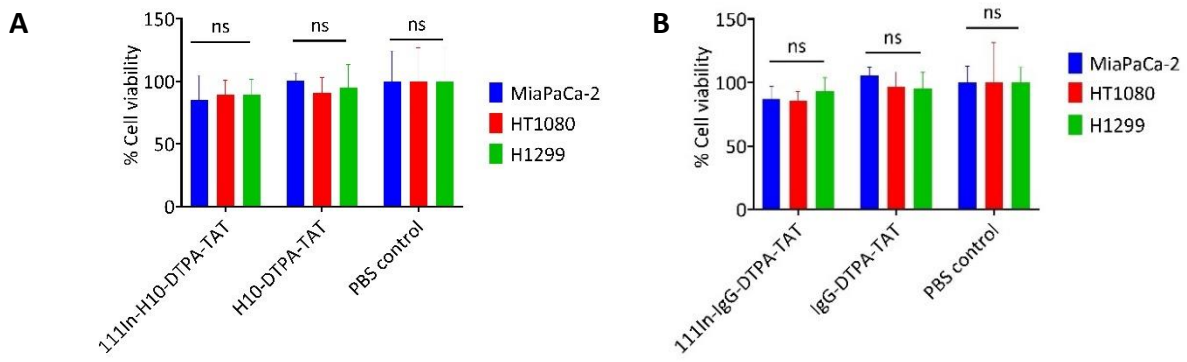


Figure 3:5) **MTT assay cell viability results after treatment with RICs and controls. A) and B)** Are [^{111}In]-DTPA-49A1/H10-TAT and [^{111}In]-DTPA-MIgG-TAT and their controls, respectively. Survival fractions compared to control wells (mean ± SD). Data analysis was performed using one-way ANOVA test in GraphPad prism (* $p < 0.05$, ** $p < 0.01$, *** $p < 0.001$).

MTT assay results were confirmed by clonogenic assay following treatment and incubation of cells with RICs for 12 days. There were no statistically significant differences in survival fractions in the three cell lines after treatment with either [^{111}In]-DTPA-49A1/H10-TAT or [^{111}In]-DTPA-MIgG-TAT (**Figure 3:6A and B**). These results confirmed the safety of the two RICs, making them potential therapeutics for further investigation and application *in vivo*.

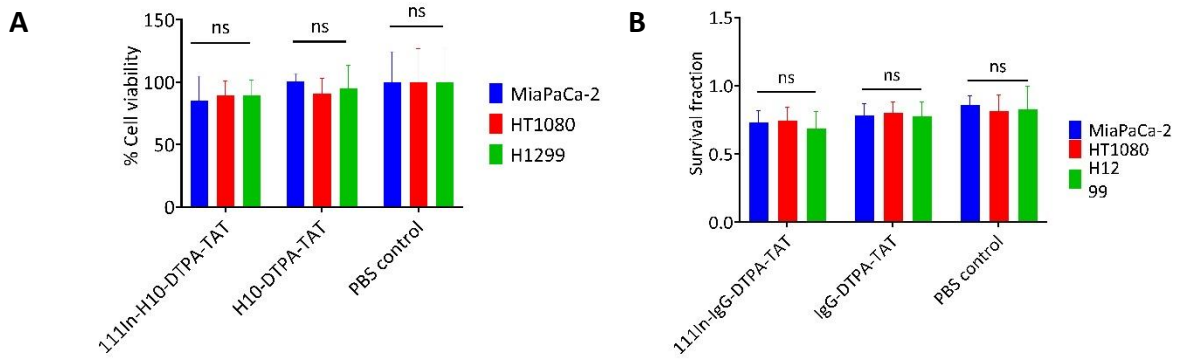


Figure 3:6) Clonogenic results after exposure to RICs treatment for 14 days. A) [^{111}In]-DTPA-49A1/H10-TAT. **B) [**^{111}In]-DTPA-MIgG-TAT. Bar graphs are represented as a mean ± SD. Data analysis was performed using one-way ANOVA test in GraphPad prism (ns – not significant).

3.3.6 *In vitro* uptake of [^{111}In]-labelled antibodies

In this work, we conjugated CPP HIV-1 TAT on both [^{111}In]-DTPA-49A1/H10-TAT or [^{111}In]-DTPA-MIgG-TAT to enhance translocation across the cell and nuclear membranes and engagement with p53. Cell based *in vitro* studies were used to evaluate the percentage of radioconjugated antibody that is delivered into the cells. Our results showed that after 1 h, the percentages of internalised RIC in MiaPaCa-2, HT1080 and H1299 cells were 2.7 $\pm$1.1%, 2.6 $\pm$0.8% and 3.5$\pm$1.0% for [^{111}In]-DTPA-49A1/H10-TAT, and 1.7 $\pm$0.8%, 1.5 $\pm$0.4% and 3.4$\pm$1.1% for [^{111}In]-DTPA-MIgG-TAT, respectively (**Figure 3:7**). There was a statistically significant difference in the percentage of internalised RICs between TAT-conjugated antibodies and non-TAT-conjugated ones. The difference in uptake of [^{111}In]-DTPA-49A1/H10-TAT and [^{111}In]-DTPA-MIgG-TAT in MiaPaCa-2 and HT1080 was statistically significant while in H1299 there was no difference in the percentage of intracellular [^{111}In]-DTPA-49A1/H10-TAT and [^{111}In]-DTPA-MIgG-TAT. Together, this data confirmed that CPP-TAT facilitates the intracellular uptake and selectivity of 49A1/H10 mAb.

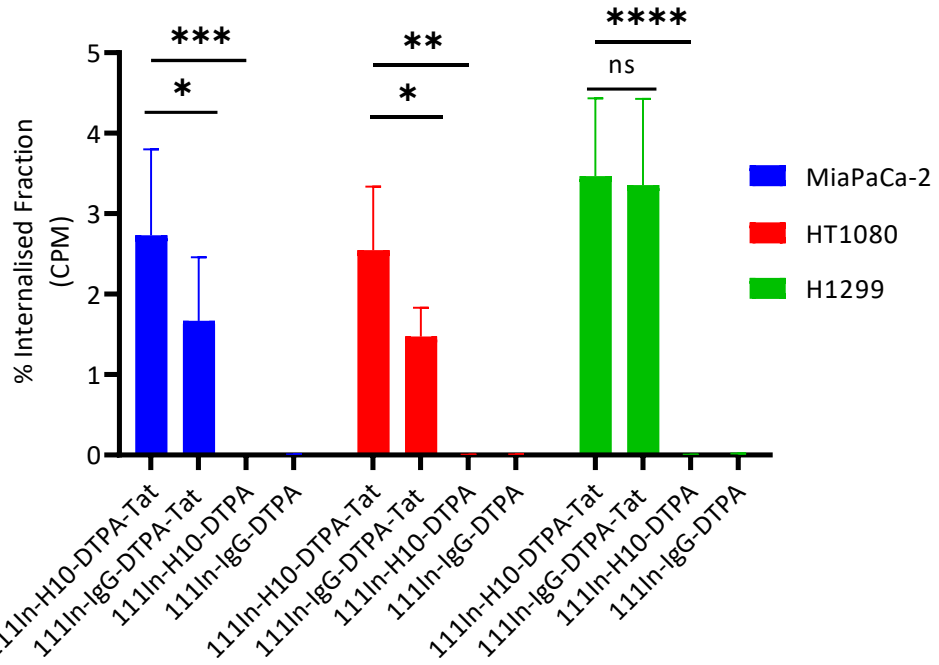


Figure 3:7) Cellular uptake of TAT conjugated and non-TAT conjugated RICs. There was a statistically significant uptake of TAT conjugated antibodies. Bar graphs are mean ± SD from 3 independent experiments in triplicates (ns – not significant, * $p < 0.05$, ** $p < 0.01$, *** $p < 0.001$, **** $p < 0.0001$).

3.3.7 *In vitro* retention of [^{111}In]-labelled antibodies

In vitro retention studies can provide preliminary evidence of the targeting specificity of radioconjugated antibodies before proceeding to *in vivo* studies. We hypothesised that a difference in retention of [^{111}In]-DTPA-49A1/H10-TAT over [^{111}In]-DTPA-MIgG-TAT in MiaPaCa-2 (high mutant p53 levels) and HT1080 (low p53 levels) and not in H1299 9 (p53 null) cells could account for p53 specificity and selectivity of [^{111}In]-DTPA-49A1/H10-TAT. As shown in **Figure 3:8A**, there was a statistically significant difference in the percentage of retained [^{111}In]-DTPA-49A1/H10-TAT in MiaPaCa-2 cells across all the time points: 0, 0.25, 0.5, 1, 2, 4 and 6 h, (p values of 0.0097, 0.005, 0.007, 0.015, 0.011, 0.0008, and 0,047, respectively). The same results were reflected in HT1080 cells except time point 4 h where the difference in amount of [^{111}In]-DTPA-49A1/H10-TAT retained was not statistically significant (p values: 0.01

(0 h), <0.0001 (0.25 h), 0.002 (0.5 h), 0.04 (1 h), 0.03 (2 h), 0.06 (4 h) and 0.01 (6 h) (**Figure 3:8B**).

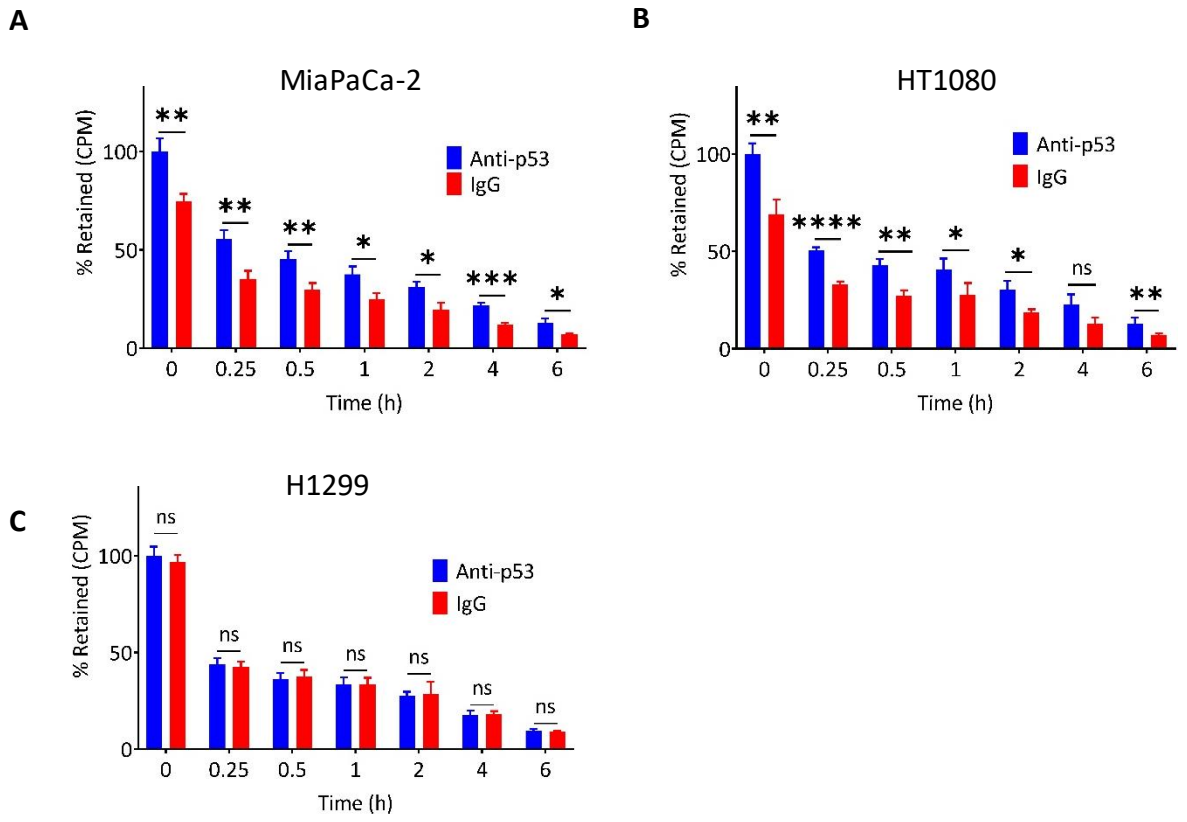


Figure 3:8) Cellular retention of Anti-p53 and MIgG RICs. A) MiaPaCa-2, **B)** HT1080 and **C)** H1299. There was a statistically significant timed-depedent retention of [^{111}In]-DTPA-49A1/H10-TAT (anti-p53) compared to [^{111}In]-DTPA-MIgG-TAT (IgG). Bar graphs are mean ± SD from 3 independent experiments in triplicates (* $p < 0.05$, ** $p < 0.01$, *** $p < 0.001$, ****$p<0.0001$, ns – not significant).

Conversely, in H1299, there was no statistically significant difference between the amount of [^{111}In]-DTPA-49A1/H10-TAT retained compared to [^{111}In]-DTPA-MIgG-TAT across all the seven time points (p values: 0.39 (0 h), 0. 59(0.25 h), 0.64 (0.5 h), 0.94 (1 h), 0.86(2 h), 0.67 (4 h) and 0.36 (6 h) (**Figure 3:8C**).

3.4 Discussion

The synthesis and validation of monoclonal antibody radioimmunoconjugates (mAb RICs) are the first crucial steps towards *in vivo* imaging using Immuno-PET/SPECT. Preceding preclinical *in vivo* application are the go/no go *in vitro* assays to evaluate the purity, binding properties, toxicity potential and stability of mAb RICs. This work focused on synthesising and *in vitro* characterisation anti-total p53 49A1/H10 mAb RICs. The SPAAC click chemistry DBCO-N_3 conjugation method was chosen because it is more quantitative than the EDC/NHS carbodiimide crosslinking method. The DBCO group can be detected at 309 nm by UV-Vis spectroscopy enabling the quantification of the relative amount of DBCO molecules attached per monoclonal antibody (A_{max} = 280 nm). In addition, this method reduces the heterogeneity of mAb RICs as the DBCO-modified mAb react specifically CPP TAT-azide and DTPA-azide, negating the possibility of antibody-to-antibody, TAT-to-TAT or DTPA-to-TAT conjugation that are common with the EDC/NHS radioconjugation method. However, better quantification of the RICs and determination number of TAT and DPTA molecules per antibody and site of antibody conjugation remains to be done using highly advanced techniques such mass spectrometry and x-ray crystallography.

Successful targeting and SPECT imaging of an intracellular protein target is dependent on effective conjugation of CPP TAT and DTPA on the mAb. The number of DBCO molecules attached to the mAb should be sufficient to enable both CPP-TAT and DPTA conjugation and not in excess to alter the binding properties of the mAb. The work by a senior PhD in student in our lab, Mathew Veal previously demonstrated that a 7-fold excess molar of DBCO-STP was sufficient to achieve a DBCO/IgG molar ratio of approximately 5 and provided the best results for subsequent CPP-TAT and DTPA conjugation (Veal et al., 2021). Our results (**Figure 3:2B**)

showed that this molar ratio could be consistently achieved in all our experiments for both [^{111}In]-DTPA-49A1/H10-TAT and [^{111}In]-DTPA-MIgG-TAT, confirming the robustness and reproducibility of the DBCO-N_3 radioconjugation method. The radiolabelling reactions were highly efficient achieving >98% radiochemical purity without purification (**Figure 3:2B**). The high radiolabelling efficiency of the DBCO-N_3 method is one of the additional advantages over the EDC/NHS method which has a maximum radiolabelling efficiency of ~80%, necessitating further purification and antibody loss.

The radioconjugation of TAT and indium-111-DTPA occur via lysine residues distributed across the antibody molecules, with some potentially found on the antigen binding region. As the DBCO-N_3 method is non-site specific, it is difficult to control the antibody conjugation site. We evaluated both the immunoreactivity and the blocking capacity of [^{111}In]-DTPA-49A1/H10-TAT as indicators of the effect of conjugation on the binding kinetics of 49A1/H10. Our results (**Figure 3:4A¬C**) confirmed that there was no effect on both the specificity and binding affinity of the antibody on total p53. This implied that the number of DBCO molecules tagged on the antibody are sufficient to allow for CPP-TAT and DTPA conjugation without altering its properties. Similar results were obtained by Mathew Veal using different antibodies (Veal et al., 2021). Even though this radioconjugation method do not alter the binding properties of the antibody, it is worth noting that the conjugation on lysine residues is non-site specific. It is also not clear whether the distribution of the conjugates per antibody is homogeneous. Such complex analyses will require advanced methods such as Liquid chromatography–mass spectrometry analysis and x-ray crystallography (Dai et al., 2020; Tang et al., 2017).

Therapeutics compounds are prone to proteolytic degradation by enzymes in the blood, plasma and serum which affects their performance bioavailability. While antibodies are

considerably stable *in vivo* for several days, radiolabelled antibodies are subject to loss the radionuclide due to transchelation to endogenous proteins albumin, superoxide dismutase and ceruloplasmin (Wållberg & Ståhl, 2013). A good chelator must stay stable and intact on the antibody without releasing the radionuclide. We evaluated the ability of [^{111}In]-DTPA to stay attached on the [^{111}In]-DTPA-49A1/H10-TAT under storage medium (PBS) and *in vivo* conditions (serum) across 72-h period. The radiolabelling efficiency of [^{111}In]-DTPA-49A1/H10-TAT remained sufficiently stable in serum to allow for *in vivo* studies. However, our indium-111 decomposition rate of 6.92%/day in serum was quite fast compared to 0.39%/day obtained by Dijkers and colleagues (Dijkers et al., 2009). Dijkers' team used the EDC/NHS radioconjugation method without CPP TAT conjugation on the trastuzumab antibody that targets an extracellular epitope, which could account for the difference in the stabilities of the antibodies. In addition, Veal et al work revealed that the stability of mAb antibody radioconjugated to TAT and [^{111}In]-DTPA using EDC/NHS method was higher compared to DBCO-N_3 method (Veal et al., 2021). It therefore calls for further research on the effect of EDC/NHS and DBCO-N_3 radioconjugation methods involving a CPP-TAT on the stability of synthesised mAb RICs.

The delivery of therapeutics into the cells presents an opportunity to expand the scope of cancer imaging as several potential cancer biomarkers are expressed inside the cell. Several methods have been employed to aid the intracellular delivery of drugs, with the most promising ones involving the use of CPPs such HIV-1 TAT and penetratin. HIV-1 TAT peptide is the most used and well characterised CPP for intracellular antibody delivery. Several intracellular proteins have been successfully targeted with a mAb antibody conjugated to HIV-1 TAT peptide including γH2AX (J. C. Knight et al., 2015). Our results suggested that TAT promotes differential uptake and retention of the mAb RICs (**Figure 3:8A¬C**).These results are

comparable to (Veal et al., 2021) who demonstrated that the DBCO-N_3 methods improves the percentage of intracellular RIC to approximately 3% from >1% seen with EDC/NHS method. There was a statistically significant between the percentage of [^{111}In]-DTPA-49A1/H10-TAT retained after 1 h compared to [^{111}In]-DTPA-MIgG-TAT in MiaPaCa-2 and HT1080 cell. This means that the clearance of TAT-conjugated antibody occurs within minutes after entrance, especially for non-specific antibody. The intracellular entry of TAT remains an unresolved puzzle, with macropinocytosis process suggested as the main method of cell membrane translocation (Kaplan et al., 2005). The mechanism of entry is influenced by several factors including cell type, cargo type/size and presence or absence of cell membrane heparan sulfate proteoglycans (Mishra et al., 2011). One of the limitations of the method we used to evaluate the amount of intracellular delivered TAT-conjugated antibodies is that it does not provide data on intracellular distribution of the RICs in the cytoplasm or nucleus. This can be achieved using a confocal microscopy to confirm the cellular distribution of a TAT-Conjugated antibody labelled with a fluorescent molecule (Patel et al., 2019). Clarification and quantification of cytoplasmic and nuclear fraction of the radioconjugated mAb can also help to evaluate the percentage of the antibody in the cytoplasm and nucleus. The retention of [^{111}In]-DTPA-49A1/H10-TAT was significantly higher than [^{111}In]-DTPA-MIgG-TAT in MiaPaCa-2 and HT1080 and similar in H1299 cells (**Figure 3:8 A¬C**). This means that the retention of the anti-p53 mAb in MiaPaCa-2 and HT1080 cells was potentially due to the presence of p53 protein validating the targeting specificity and binding properties of the [^{111}In]-DTPA-49A1/H10-TAT. In addition, the cellular uptake of TAT peptide is affected by heparan sulfate proteoglycans that form part of the extracellular matrix. While all tissues express proteoglycans, the levels of expression vary with cell type. As a result, different cell type can experience variable TAT uptake profile which in effect can influence the amount of intracellular TAT (Ruseska &

Zimmer, 2020). Even though we have no data on the expression levels of heparan sulfate proteoglycans on MiaPaCa-2, HT1080 and H1299, and whether that played a role in the variable amount TAT-mAb delivered in these cells, we believe these assays could be improved by using isogenic cell lines. The use of MiaPaCa-2 or HT1080 isogenic cell lines with different p53 levels based on siRNA or CRISPR gene editing would have been the suitable models for evaluating amount of TAT uptake as it removes the cell type and heparan sulfate proteoglycans expression levels as confounding variables. We propose this models in the future experiments.

Finally, the effect of addition of CPP-TAT and indium-111 radionuclide on mAb on cell viability was evaluated. Both CPP-TAT and indium-111 can lead to cell poisoning as well as alter the pharmacokinetics profile of the antibody leading to increased non-specific tissue accumulation and unwarranted sides effects. Higher concentrations of CPP-TAT (>100 µM) can be toxic to the cells, while the Auger electron emitting indium-111 radionuclide can induce DNA damage when delivered to the nucleus where p53 is expressed (Cardozo et al., 2007; Cornelissen et al., 2012). Both MTT assay (**Figure 3:5**)and clonogenic survival assay results (**Figure 3:6**) confirmed that there was no significant cytotoxic effect on MiaPaCa-2, HT1080 and H1299 cell viability. Similar results were obtained by Cornelissen et al. who confirmed that [^{111}In]-anti-γH2AX-TAT or [^{111}In]-rIgG-TAT did not cause any significant increase in γH2AX foci in treated cell versus controls. There was also no noticeable effect on tumour growth (Cornelissen et al., 2014). Therefore, small amounts of both CPP-TAT and indium-111 radionuclide can be used for imaging intracellular protein targets without resulting in any pronounced cellular toxicity.

3.5 Conclusion

This chapter aimed to synthesis anti-total p53 mAb RICs and validate their *in vitro* binding properties, cellular toxicities, uptake, and retention. Our results demonstrate that [^{111}In]-DTPA-49A1/H10-TAT maintains immunoreactivity towards total p53 protein with similar binding affinity as its native parent. The addition of CPP TAT on the mAbs facilitates intracellular delivery, and [^{111}In]-DTPA-49A1/H10-TAT is retained significantly higher in p53 expressing cells compared to H1299 p53 null cells. The addition of both CPP-TAT and indium-111 radionuclide to the anti-total p53 mAb did not result in significant cellular toxicities. Taken together, this work established sufficient evidence of the *in vitro* safety and binding properties of the [^{111}In]-DTPA-49A1/H10-TAT, qualifying it as a good candidate for *in vivo* interrogation of p53 in mouse xenografts using immuno-SPECT-CT. The work in the ensuing chapter focused on preclinical imaging of p53 protein *in vivo* using the [^{111}In]-DTPA-49A1/H10-TAT.

4 Chapter 4 – Immuno-SPECT imaging of p53 in subcutaneous mouse xenografts

4.1 Introduction

This work focused on evaluating the ability of [^{111}In]-DTPA-49A1/H10-TAT to interrogate p53 protein levels in subcutaneous mouse xenografts using preclinical SPECT/CT imaging modality.

Molecular imaging (MI) of cellular abnormalities preceding invasive cancer development hold a great potential to aid in cancer early detection and improvement of overall survival rates. MI offer exceptional advantages over anatomical imaging modalities such as MRI, CT scan and EUS that lack the required sensitivity and specificity to detect precancerous lesions before becoming invasive and metastatic. PET and SPECT which epitomise molecular imaging modalities are exquisitely sensitive enabling detection of biomarkers up to picomolar concentration, are non-invasive and allow for whole body imaging enabling the detection of primary tumours, and regional and distant metastases. MI of cancer biomarkers can provide patient-specific molecular and pathogenic information aiding in cancer detection, patients' treatment stratification and assessment of response to treatment (James & Gambhir, 2012). Despite their huge potential, PET and SPECT remain underutilised in cancer imaging due to lack of specific and sensitive biomarkers, logistical issues, and high cost. The use of PET or SPECT for cancer imaging require the validation of cancer specific biomarkers in a representable population of patients. In addition, MI require the synthesis and validation of a molecular imaging agent specifically targeting the biomarker of interest. An imaging agent is composed of (a) targeting moiety such as a mAb, small peptide, small molecule, or nanoparticle, (b) detectable radionuclide component such as indium-111 or zirconium 89 and (c) and linker to connect the targeting and detectable components e.g., DTPA or DOTA chelator (Wållberg & Ståhl, 2013).

In this work, I set to exploit the advantages of SPECT imaging to interrogate p53 protein in PDAC xenografts. In chapter 2, it was confirmed that mutant p53 is overexpressed in four PDAC cell lines (MiaPaCa-2, BxPc-3, PANC-1, and FAMPAC-1) expressing p53 hotspot mutants. In chapter 3, we synthesised and validated [^{111}In]-DTPA-49A1/H10-TAT SPECT imaging agent targeting total p53 protein with high specificity, nanomolar binding affinity and no unwarranted cellular toxicities. Groups of mice were inoculated with MiaPaCa-2 (high mutant p53 expression), HT1080 (low wild type p53 expression) and H1299 (no p53 expression) tumour xenografts were developed. The mice xenografts were randomised to [^{111}In]-DTPA-49A1/H10-TAT or [^{111}In]-DTPA-MIgG-TAT injections and evaluated for tumour uptake and specificity using preclinical SPECT/CT.

4.2 Material and methods

4.2.1 Mouse models

All mice (Charles River, UK) experiments were carried out as per the UK Animals (Scientific Procedures) Act 1986 and local ethical committee approval. Mice (female) were housed in IVC cages in groups of four or five, in an artificial day-night cycle facility with ad libitum access to food and water. Three cell lines with different p53 expression status were used to grow tumours: MiaPaCa-2 (derived from pancreatic cancer overexpressing p53 mutant R248W), HT1080 (derived from fibrosarcoma tissue and express wild-type p53) and H1299 (derived from non-small cell lung carcinoma tissue and are p53 null).

4.2.2 Cell preparation for inoculations

Cells were cultured to 60-70% confluence and harvested by trypsinisation as described previously. The cells were washed in sterile cold PBS by centrifuging at 200 × g. Cells were counted using an automated cell counter and resuspended in cold PBS at a concentration of

2×10^6 cell per 100 µL. For MiaPaCa-2 and H1299 cells, cell suspension was made in a 50:50 solution of PBS and phenol red free high concentration matrigel (Corning, NY, USA). HT1080 cells (2×10^6 cell) were prepared in 100 µL cold PBS. Cells were inoculated into the right flanks of the mice via subcutaneous injection, 10 mice per each cell line. Tumours were allowed to grow for four weeks to an approximate volume of 125-200 mm^3.

4.2.3 Radiolabelling of DTPA-Bn-49A1/H10-TAT conjugates with $[^{111}In]Cl_3$

The $[^{111}In]$-DTPA-49A1/H10-TAT and $[^{111}In]$-DTPA-MIgG-TAT were prepared and purified to >95% radiochemical purity as described in sections **3.2.1**, **3.2.2** and **3.2.3**.

4.2.4 SPECT/CT acquisition and image analysis

Mice were anaesthetised by inhalation of 4% isoflurane and randomised to 3-5 MBq/5µg of either $[^{111}In]$-DTPA-49A1/H10-TAT or $[^{111}In]$-DTPA-MIgG-TAT via the lateral tail vein (5 mice per antibody per group). After 24 h, 48 h and 72 h, each mouse was subjected to a 15-min SPECT/CT (VECTor4 CT, MILabs) (Utrecht, Netherlands) image acquisition under 2% isoflurane and oxygen (80%/20% v/v; flow rate 1 L/min) anaesthetic conditions, which was carefully monitored based on the animal's respiration rate (maintained at 50 – 60 breaths per minute). Mice were first imaged with CT (55 kV, 19 mA) and immediately followed by SPECT image acquisition at 24, 48, and 72 h post injection (p.i.) of the RICs. After the acquisition at the 72 h, mice were culled and samples of blood, eight other vital organs (spleen, pancreas, kidneys, liver, heart, lungs, muscle, bone) and tumour collected. The weight of organs and the amount of radioactivity was determined using a Hidex Automatic Gamma Counter (Hidex Oy, Turku, Finland) and used to calculate the percentage injected dose per gram (%ID/g) of tissue. The radioactivity counts were decay corrected to the amount of injected dose for each mouse. Immediately after radioactivity counting, tumours were flash frozen using liquid nitrogen and

stored at -80°C and kept for histological analysis. Images were reconstructed, calibrated, and registered with MILabs reconstruction software v11.0. The images were viewed and analysed using PMOD v.3.37 (PMOD Technologies, Switzerland).

4.2.5 Image analysis

CT and SPECT images were reconstructed with MILabs reconstruction software REC-11.00; SPECT images were reconstructed at the energy windows indium-111 energy windows: (160.5 – 196.9 keV and 225.3 – 275.9 keV) with a 0.600 mm voxel size, eight subsets and four iterations using similarly regulated ordered-subset expectation maximisation (SROSEM). Both reconstructed CT and SPECT images were co-registered to equivalent 200 µm voxel sizes. A phantom was used to determine the calibration factor which was applied during quantification of SPECT images for accurate scaling using known activity of indium-111. Image processing and volume of interest (VOI) analysis was carried out using the PMOD software v.3.37 (PMOD Technologies, Zurich, Switzerland).

4.2.6 Histological analysis of tumour xenografts

Histological analysis of mice tumours was performed to confirm p53 expression status and to evaluate the targeting efficiency of the radiolabelled antibodies. Tumours were embedded in optimal cutting temperature (OCT, Fisher Scientific, USA) solution and placed in a cryostat microtome (HM 520; Microm International GmbH) set to -20°C. Sections of 10-15 µm were cut and transferred to a glass slides and stored at -80% before immunohistochemistry staining and autoradiography.

4.2.6.1 Immunohistochemical staining

Frozen glass slides with tumour sections were air dried for 10 min at RT, rehydrated by washing with PBS for 3 x 5 min. Slides were dipped in 99 mL MeOH 1 mL 30% H_2O_2 for 20 min

to quench the endogenous peroxidase and again washed in a bucket of PBS for 2 x 5 min and then for 5 min in 0.1% PBS Tween (PBST). Slides were then blocked with 10% goat serum in PBST for 1 h at RT. Slides were washed 3 x 5 min in PBST and incubated overnight at 4˚C with rabbit-anti-p53 antibody (PA5-27822, Thermo Fisher Scientific, USA) prepared in 10% goat serum PBST. Slides were washed 3 x 5 min in PBST and incubated for 1 h at RT with mouse IgG (H+L) PA1-28567 secondary antibody (Thermo Fisher Scientific, USA) prepared in 10 % goat serum PBST. Slides were washed 3 x 5 min in PBS and dipped in a bucket of 300 mL 0.1 M phosphate buffer 30% H_2O_2, 3,3'-Diaminobenzidine (DAB) for up to 5 min until DAB staining development was observed. Slides were then dipped in acidified water for 30 seconds, then crystal violate for 1 min and dehydrated by rinsing in distilled water, 75% ethanol, 90% ethanol and 100 % ethanol each for 1 min. Finally, slides were washed 3 x 20 min in fresh xylene. Slides were then mounted with DPX Mountant (Abcam, UK) and airdried for 24 h before scrubbing using a scalpel and wiped with 70% ethanol to remove residual and excess mountant. Slide imaging was done using Aperio CS2 image capture (Leica Biosystems, USA) and images analysed using Aperio ImageScope software v. 12.4.6 (Leica Biosystems, USA).

4.2.6.2 Autoradiography

Frozen glass slides with tumours were air dried for 30 min at RT and then washed with cold PBS for 3 x 3 min to remove residual OCT and air dried for 30 min. The sections were placed over phosphor films (EJ-440, Eljen Technology), made of a sliver-activated zinc sulphide phosphor on the scintillation side. The film was exposed to tissue section radioactivity for 24 h and then scanned on a PhosphorImager Cyclone Plus Storage Phosphor System (PerkinElmer Inc, USA). The images taken were viewed and analysed using ImageJ software (National Institutes of Health, USA).

4.2.7 Statistical analysis

One-way ANOVA with Turkey's post hoc test or 2-way ANOVA were used to analyse group data and to determine any difference between individual group means. GraphPad Prism v8 (GraphPad Software, CA, USA) was utilised in statistical analysis of all data. All animal experiments were carried out in groups of five and presented as mean ± one standard deviation unless otherwise stated.

4.3 Results

4.3.1 Biodistribution of Anti-p53 (49A1/H12) and MIgG RICs in p53 xenograft models

After the terminal SPECT/CT image acquisition at time point 72 h, mice were euthanised via cervical dislocation and organs of interest plus tumours were harvested for weighing and radioactivity counting. Analysis of MiaPaCa-2 and HT1080 tumours revealed a statistically significant difference in the uptake of [^{111}In]-Anti-p53 (49A1/H10)-TAT compared to [^{111}In]-MIgG-TAT as defined at the percentage of injected dose per gram (%ID/g) (**Figure 4:1**). In MiaPaCa-2, the tumour uptake of 49A1/H10 was 4.1$\pm$1.0 %ID/g and was significantly higher than the uptake of MIgG 1.5$\pm$0.7 % ID/g, ($p = 0.0097$). HT1080 tumours revealed a similar tumour uptake pattern for [^{111}In]-49A1/H10-TAT (5.6$\pm$0.4 %ID/g) and [^{111}In]-MIgG-TAT (2.9$\pm$0.5 %ID/g), $p = 0.005$. In H1299 tumours, there was lower tumour uptake but no statistically significant difference between 49A1/H10 (3.4$\pm$0.7 %ID/g) and MIgG (4.2$\pm$0.3), $p = 0.1544$.

Tumour uptake ratios of anti-p53 to MIgG (A/M) were calculated (**Figure 4:2A**). MiaPaCa-2 and HT1080 tumours had a statistically significant higher A/M ratios of 2.2±0.4 ($p=0.0027$) and 2.0±0.3 ($p=0.0023$) compared to H1299 A/M of 0.8±0.1. The-tumour to-blood ratios (T/B) for 49A1/H10 were higher but not statistically significant from MIgG. In MiaPaCa-2 the T/B

ratio was 0.6±0.2 vs 0.4±0.1 while for HT1080 0.6±0.1 vs 0.5±0.1. However, this was not statistically significant (**Figure 4:2C**). H1299 tumours displayed similar tumour-to-blood ratios for 49A1/H10 (0.4±0.1) and MIgG (0.4±0.1). Similarly, the tumour-to-muscle ratios for 49A1/H10 were higher in MiaPaCa-2 (5.4±1.4) and HT1080 (5.4±1.2) compared to MIgG in MiaPaCa-2 (3.1±0.8) and HT1080 (3.7±0.4), although these were not statistically significant. H1299 tumours had comparable tumour-to-muscle ratios for 49A1/H10 (3.5±0.7) and MIgG (4.0±0.3) (**Figure 4:2B**).

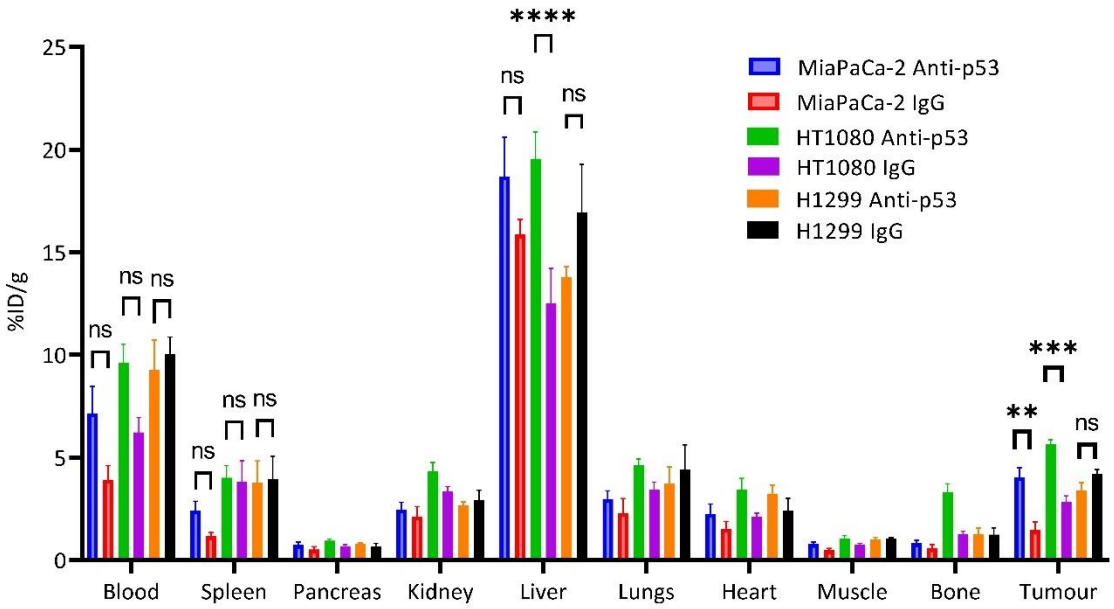


Figure 4:1) Ex vivo biodistribution and uptake of Anti-p53 and MIgG RICs. Percentage of the injected dose per gram of the two RICs in the selected organs were counted after 72 h intravenous administration. Bar graphs are mean ± SD, n=5 (ns – not significant, * $p < 0.05$, ** $p < 0.01$, *** $p < 0.001$, **** $p < 0.0001$).

The amount of radioactivity of the two RICs remained high in the blood and liver, and was statistically similar among the three xenografts except for HT1080 mice where liver 49A1/H10 uptake was significantly higher than MIgG. In addition, 49A1/H10 displayed higher uptake

compared to MIgG in MiaPaCa-2 and HT1080 organs, even though this was not statistically significant apart from the tumours.

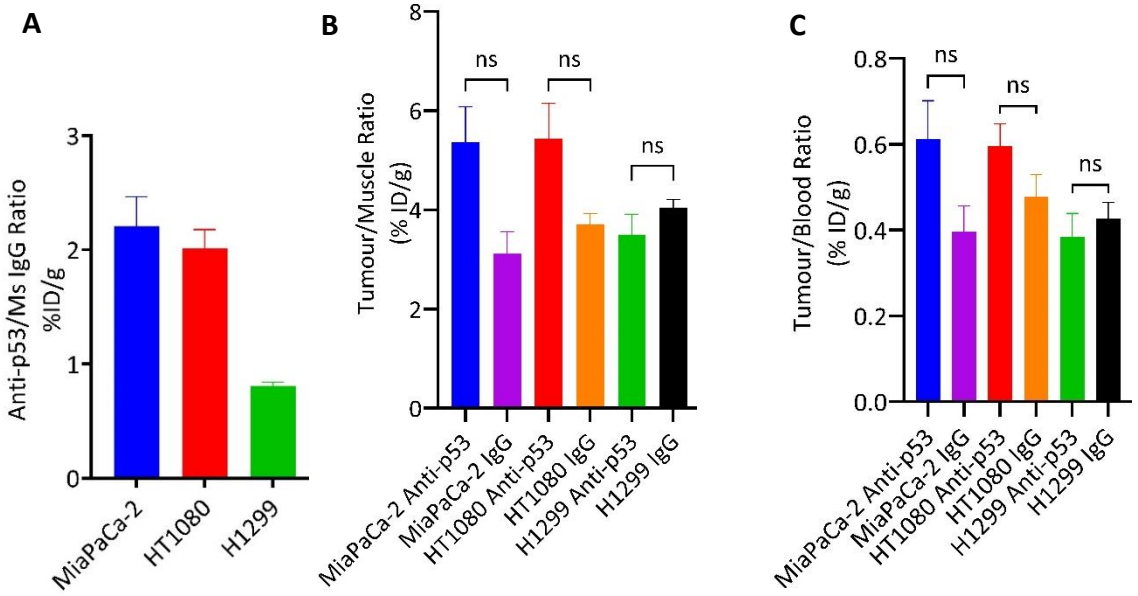


Figure 4:2) Ex vivo tumour uptake ratios. A) Anti-p53 to MIgG ratios. **B)** Tumour-to-muscle uptake ratios and **C)** tumour-to-muscle ratios. Bar graphs represent mean ± SD (n= 3 or 4 animals, ns - not significant).

4.3.2 *In vivo* SPECT imaging of p53 xenografts

Image quantification was performed to evaluate the distribution of [^{111}In]-DTPA-49A1/H10-TAT and [^{111}In]-DTPA-MIgG-TAT at 24 h, 48 h and 72 h (**Figure 4:3**). In MiaPaCa-2 xenografts, there was a steady increase in the amount of 49A1/H10 uptake, which was significantly higher compared to the MIgG uptake at time points 46 h and 72 h: 24 h (1.48±0.29 vs 0.62±0.23, p = 0.37), 48 h (2.05±0.85 vs 0.66±0.47, p=0.048) and 72 h (2.07±0.69 vs 0.65±0.35, p=0.004). The radioactivity of MIgG in the tumours remained significantly low and comparable across the three timepoints (**Figure 4:4A**). In addition, there was a sharp decline in the amount of radioactivity in the heart for both 49A1/H10: 24 h (3.56±0.92), 48 h (2.66±0.78), 72 h (1.65±0.68) and MIgG: 24 h (1.89±0.50), 48 h (1.56±0.37), 72 h (1.21±0.42). There was no

statistical difference in the amount of MIgG radioactivity retained in the heart across the three time points (**Figure 4:4A**).

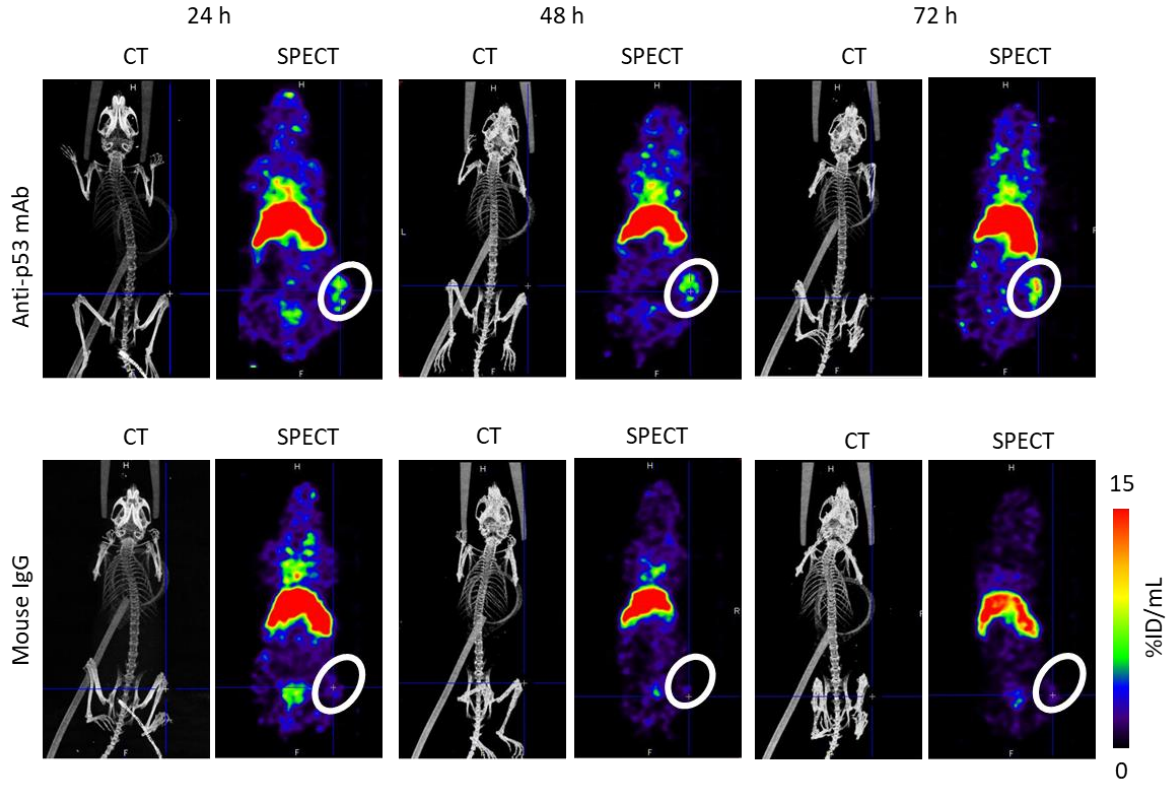


Figure 4:3) ***In vivo*** **imaging of RICs in MiaPaCa-2 tumours.** Representative CT and SPECT images showing distribution of Anti-p53 mAb and MIgG RICs in MiaPaCa-2 mice xenografts, 24 h, 48 h and 72 h after intravenous administration.

The tumour-to-blood (T/B), tumour-to-muscle (T/M) and Anti-p53 to IgG (A/M) ratios were determined as shown in **Figure 4:4B¬D**, respectively. Generally, [^{111}In]-DTPA-49A1/H10-TAT displayed a time dependent increase in T/B and T/M ratios reaching the highest at 72 h (1.7$\pm$0.5 and 7.0$\pm$1.9, respectively). The T/B and T/M for MIgG were comparatively low across the 72 h and lower compared to 49A1/H10 (**Figure 4:4C** and **D**). The A/M ratios increased from 2.7±1.2 at 24 h to 4.8$\pm$2.4 at 72 h, even though this was not statistically significant. (**Figure 4:4B)**.

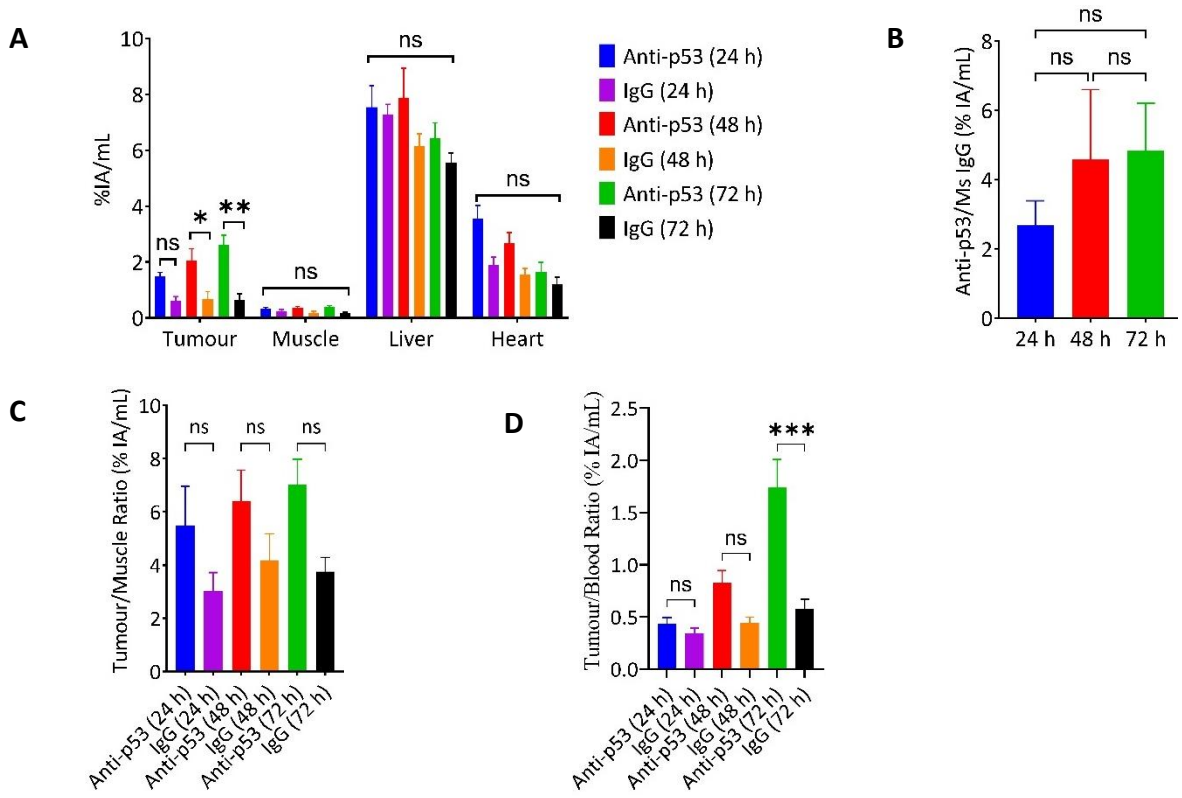


Figure 4:4) VOI analysis of MiaPaCa-2 SPECT images. A) Tumour uptake (%ID/mL) in selected tissues at 24 h, 48 h and 72 h p.i. B), C) and D) Anti-p53 to MIgG, tumour-to-muscle, and tumour-to-blood tumour uptakes ratios, respectively. Bar graphs represent mean ± SD (n= 3 or 4 animals, ns - not significant, * $p < 0.05$, ** $p < 0.01$, *** $p < 0.001$).

Similarly, HT1080 displayed a comparable radioactivity distribution profile as MiaPaCa-2 xenografts (**Figure 4:5**). There was a time-dependent increase in tumour uptake of [^{111}In]-DTPA-49A1/H10-TAT (2.99±0.09 at 24 h, 3.56±0.10 at 48 h and 4.73±0.12 at 72 h), which were statistically significant compared to MIgG ($p<0.0001$). The tumour uptake of MIgG remained low and constant across the selected timepoints (**Figure 4:6A**). The T/B and T/M ratio revealed a statistically significant increasing trending compared to MIgG, with the highest achieved at 72 h (1.65±0.13 and 11.77±3.25 respectively). Similarly, A/M ratios increased over 72 h reaching 7.83±4.23 (**Figure 4:6 B¬D**).

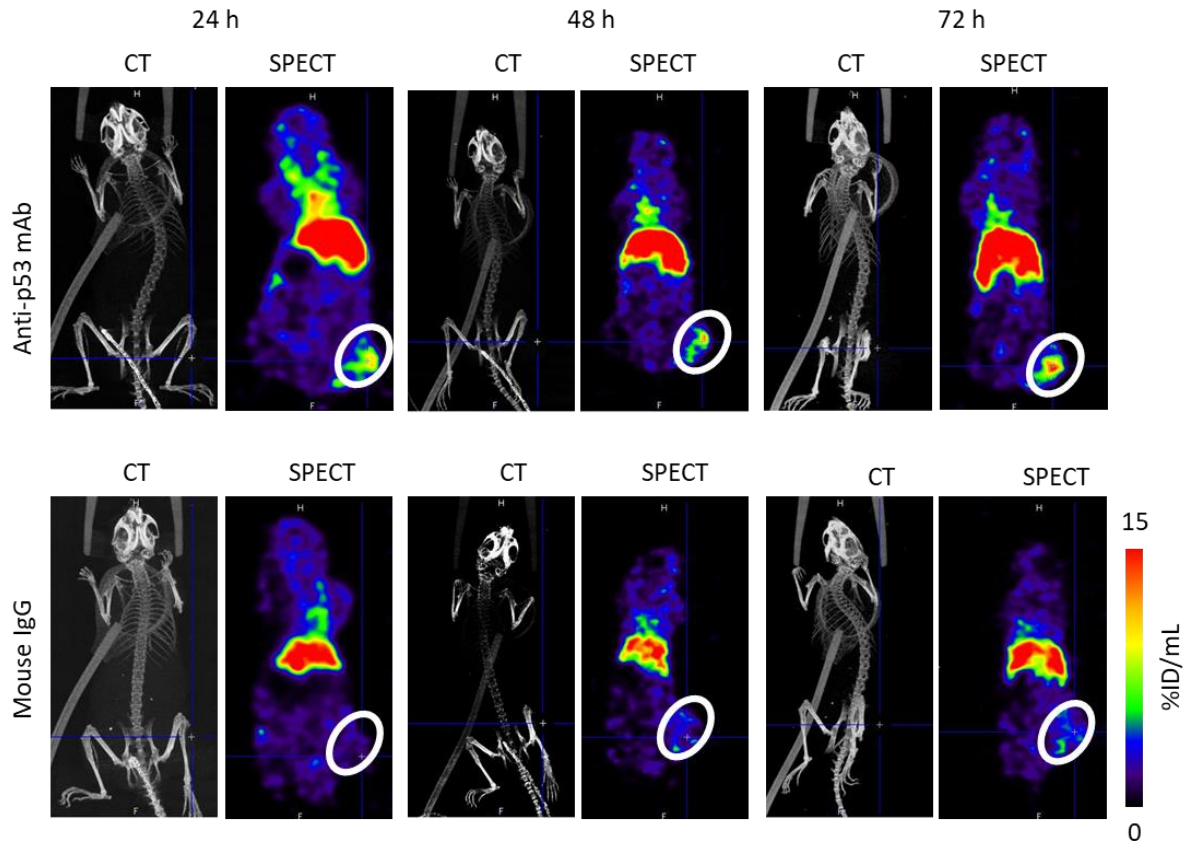


Figure 4:5) ***In vivo*** **imaging of RICs in HT1080 tumours.** Representative CT and SPECT images showing distribution of Anti-p53 mAb and MIgG RICs in HT1080 mice xenografts, 24 h, 48 h and 72 h after intravenous administration.

In addition, the H1299 xenografts were used as negative controls as they lack p53 due to the deletion of both alleles of p53 gene. We evaluated the uptake and biodistribution of [^{111}In]-DTPA-49A1/H10-TAT and [^{111}In]-DTPA-MIgG-TAT in these tumours (**Figure 4:7**). There were no statistically significant differences in uptake of both 49A1/H10 and MIgG in H1299 tumours across the 24 h, 48 h and 72 h time points (**Figure 4:8A)**. Compared to MiaPaCa-2 and HT1080 tumours, the %ID/g of 49A1/H10 in H1299 tumours was significantly lower at 72 h (p values = 0.0172 and <0.001 respectively). In contrast, the uptake of MIgG was comparable across the three xenografts (**Figure 4:6E**). There was no observed time dependent increase or differences in T/B, T/M and A/M ratios for %ID/g between 49A1/H10 and MIgG (**Figure 4:8B¬D**)

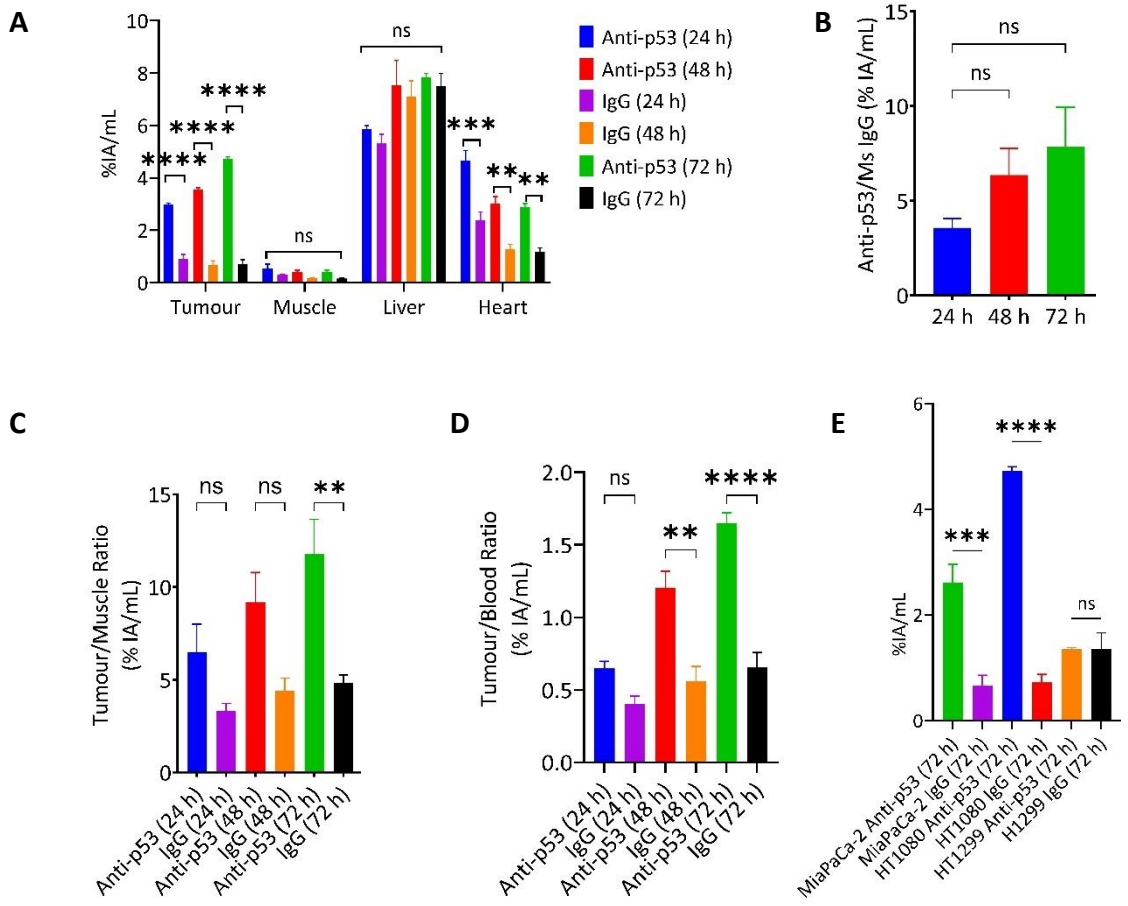


Figure 4:6) VOI analysis of HT1080 SPECT images. A) Tumour uptake (%ID/mL) in selected tissues after 24 h, 48 h and 72 h. **B), C) and D),** Anti-p53 to MIgG, tumour-to-muscle, and tumour-to-blood tumour uptake ratios. **E)** MiaPaCa-2, HT1080 and H1299 SPECT images VOI quantification analysis of Anti-p53 and MIgG RICs biodistribution *in vivo* at 72 h. Bar graphs represent mean ± SD (n= 3 or 4 animals, ns - not significant, * $p < 0.05$, ** $p < 0.01$, *** $p < 0.001$, **** $p<0.0001$).

4.3.3 Histological analysis of xenografts

MiaPaCa-2, HT1080 and H1299 were analysed for p53 expression and [^{111}In]-DTPA-49A1/H10-TAT targeting efficiency using IHC and autoradiography, respectively. IHC staining revealed heterogeneous p53 expression in MiaPaCa-2 and HT1080 xenografts (**Figure 4:9A and B**). p53 signal was stronger in MiaPaCa-2 than HT1080, confirming the *in vitro* data (**Figure 2:7**) which

showed that mutant p53 levels in MiaPaCa-2 were significantly higher than in the HT1080 wild type p53. No p53 staining was observed in H1299 xenografts **(Figure 4:9C)**.

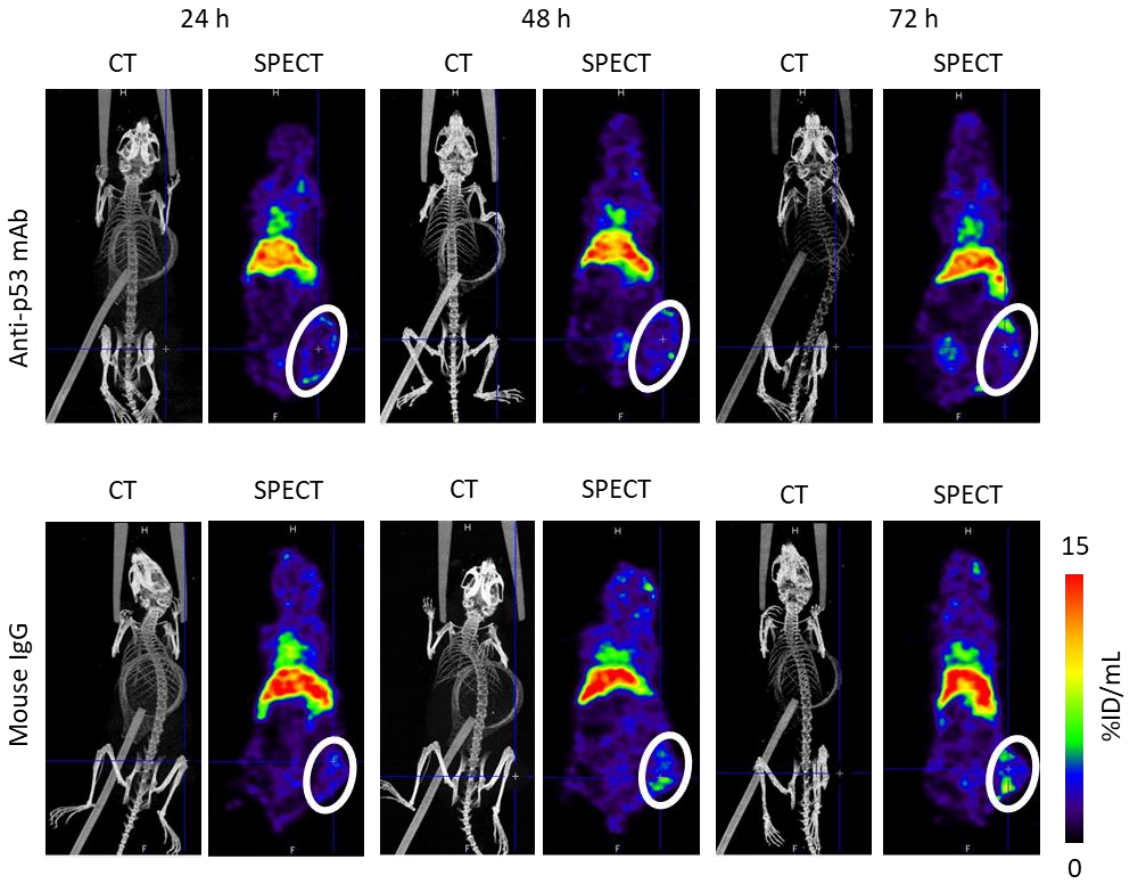


Figure 4:7) ***In vivo*** **imaging of Anti-p53 and MIgG RICs in H1299 tumours.** Representative CT and SPECT images showing distribution of Anti-p53 mAb and MIgG RICs in H1299 mice xenografts, 24 h, 48 h and 72 h after intravenous administration.

The uptake and distribution of [^{111}In]-DTPA-49A1/H10-TAT exhibited heterogenous distribution in MiaPaCa-2, HT1080 and H1299 tumours, with regions of both focal (green arrow) and diffuse (black arrow) distribution revealed (**Figure 4:10**). The quality of HT1080 and H1299 tumours was suboptimal due to damage caused by poor storage conditions during processing. It was, therefore, difficult to correlate p53 staining from IHC images with autoradiography images.

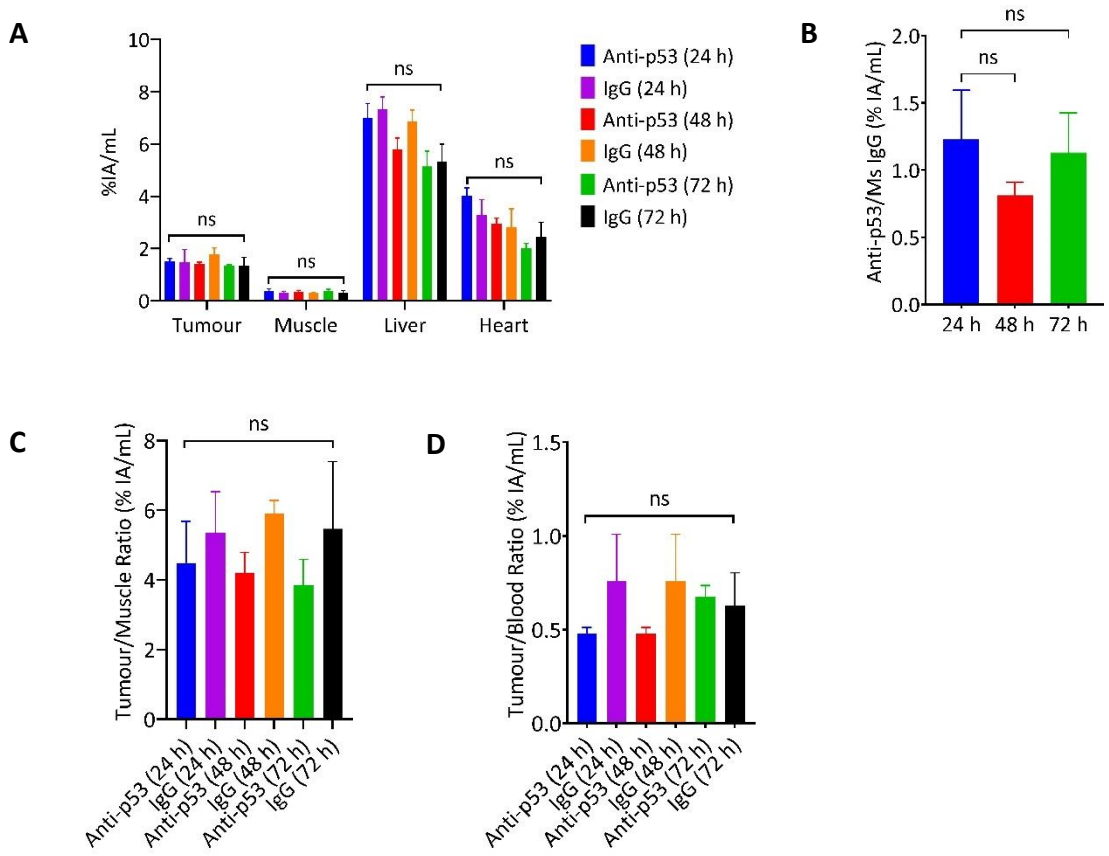


Figure 4:8) VOI analysis of H1299 SPECT images. A) Tumour uptake (%IA/mL) in selected tissues after 24 h, 48 h and 72 h. **B), C)** and **D),** Anti-p53/MIgG, tumour-to-muscle, and tumour-to-blood tumour uptake ratios. Graphs represent mean ± SD (n= 3 or 4 animals, ns - not significant).

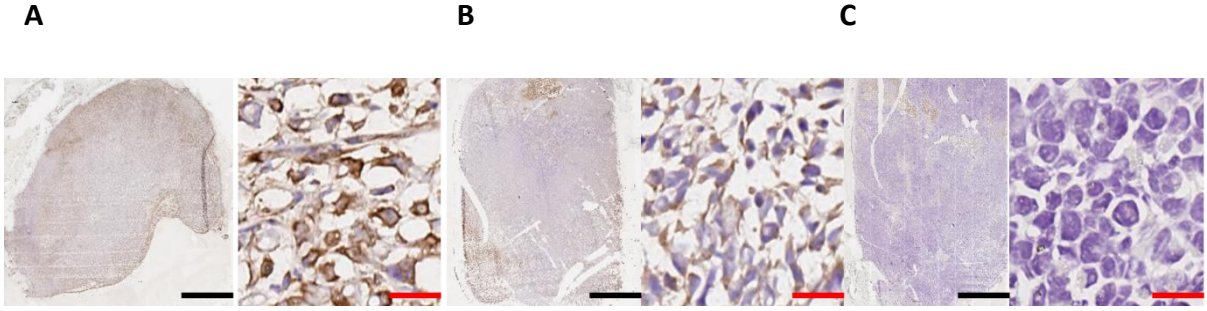


Figure 4:9) Immunohistochemistry analysis of xenograft tumour sections. IHC images showing staining and levels of p53 in **A)** MiaPaCa-2**, B)** HT1080 and **C)** H1299 tumours. Black scale bars: 2 mm; red: 200 µm.

4.4 Discussion

In this work, we have demonstrated the feasibility of SPECT imaging of p53 in subcutaneous mouse xenografts using a TAT-conjugated radiolabelled mAb. p53 is the most frequently mutated gene in cancer occurring in more than half of human malignancies. Several cancers have very high penetrance of p53 mutations including ovarian serous carcinoma (96%), small cell lung cancer (85%) and pancreatic ductal adenocarcinoma (75%) (Blandino & di Agostino, 2018). In PDAC, it has been revealed that p53 mutants are overexpressed in invasive precancerous lesions and tumours and are associated with chemo/radioresistance and overall poor prognosis (Koorstra et al., 2009). Therefore, *in vivo* interrogation of p53 expression status could serve as an early diagnostic marker among enriched high risk PDAC populations.

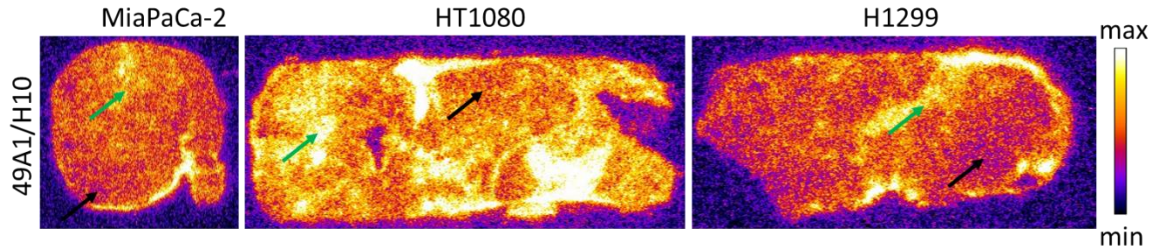


Figure 4:10) Autoradiography of xenograft tumour sections. Autoradiography images showing uptake and distributions of [^{111}In]-DTPA-49A1/H10-TAT in MiaPaCa-2, HT1080 and H1299 xenografts. Green arrows indicate regions of high RICs uptake while black arrows indicate tumour regions with low uptake.

Mutant p53 imaging could also aid in patients' treatment stratification and better therapeutic decision making. Here, the total p53 monoclonal antibody imaging agent [^{111}In]-DTPA-49A1/H10-TAT was employed to image p53 mouse xenografts. The tumour uptake and biodistribution of the imaging agent was evaluated in MiaPaCa-2, HT1080 and H1299 tumour mouse models.

Our data show that *in vivo* imaging of both mutant and wild type p53 using a monoclonal antibody could help differentiate p53 expressing tumours from p53 null type tumours. Both biodistribution and SPECT VOI data of MiaPaCa-2 and HT1080 xenografts revealed increased tumour uptake compared to H1299 (**Figure 4:1**). However, the amount of [^{111}In]-49A1/H10-TAT uptake in MiaPaCa-2 was lower compared HT1080, which did not correlate with p53 protein levels as demonstrated by *in vitro* data (**Figure 4:6E**). The enhanced uptake in HT1080 tumours could be due to pronounced enhanced permeability and retention effect (EPR) in these tumours which also displayed higher MIgG uptake compared to MiaPaCa-2 tumours **Figure 4:1**. The HT1080 mice xenografts are characterised by a higher density of microvessel clusters and increased tumour vasculature that are known to enhance EPR (Hanyu et al., 2009). Another plausible reason for lower tumour uptake in MiaPaCa-2 xenografts is because they form less vascularised and low perfused tumours that can attenuate efficient drug delivery (Kano et al., 2007; Otowa et al., 2022). However, the significant differential tumour uptake between 49A1/H10 and MIgG in these tumours has established a preliminary evidence of targeting MiaPaCa-2 tumours using monoclonal antibody therapeutics. Evaluation of H1299 SPECT VOIs and biodistribution data showed high but comparable tumour uptake of both 49A1/H10 and MIgG (**Figure 4:8**). The enhanced uptake could result from the EPR effect because of the angiogenic and highly perfused nature of H1299 tumours (Singla et al., 2015).

Autoradiography results provided insights into the targeting efficiency of the anti-p53 (49A1/H10) RIC. The radiolabelled anti-p53 was heterogeneously distributed across the tumour tissues as revealed by regions of high (green arrows) and low (black arrows) radioactivity (**Figure 4:10**). This could result from both heterogenous expression of p53 or the inherent heterogeneous nature of cancer which affects perfusion and thus tumour drug delivery and distribution. This conclusion was corroborated by our IHC data which revealed a

heterogeneous p53 expression pattern in both MiaPaCa-2 and HT1080 tumours. Genomic and intra/intertumoral heterogeneity is a common feature of many cancers including PDAC, NSCLC and soft tissues sarcomas and influence both patient prognosis and treatment response (Z. Chen et al., 2014; Connor & Gallinger, 2021; Du et al., 2020). The amount of radioactivity for Anti-p53 RICs was higher but not statistically significant compared to MIgG RICs in all MiaPaCa-2 and HT1080 organs. This could result from the binding of 49A1/H10 p53 mAb and not the MIgG nonspecific to endogenous p53.

A major obstacle impeding radiolabelled antibody clinical translation is the high liver uptake and long blood residence time which lead to hepatic and red marrow toxicities (Parakh et al., 2022). The antibody fragment crystallisable domain (Fc domain) prevents the antibody degradation through neonatal Fc receptor (FcRn) mediated recycling (Fcyn) (Pyzik et al., 2015). The large size of the monoclonal antibody (150 kDa) contributes to slow pharmacokinetics and hepatic metabolism and clearance (Zhao et al., 2012). In addition, the long circulation means the patient must wait 3 days or longer before being imaged, which can reduce screening compliance. A number of strategies have been developed and utilised to reduce monoclonal antibodies slow pharmacokinetics and high liver uptake. Firstly, the use of small antibody fragments such as Fab fragment (48 kDa), a single chain Fv (scFv; 24 kDa) have proven to decrease blood residence time, enhance tumour penetration and clearance via the renal metabolism (Kholodenko et al., 2019). Secondly, small peptides and affibodies have risen as potential cancer imaging agents because of their small size, faster pharmacokinetics and tumour accumulation and clearance from target tissues (Frejd & Kim, 2017; Sun et al., 2017). In addition, Fc domain engineering and deglycosylation have been employed to reduce FcRn recycling and high liver uptake (Delidakis et al., 2022; Vivier et al., 2019).

Monoclonal antibody-based cancer imaging can be an obstacle for PDAC imaging due to the dense stromal tissue that surrounds the cherry-sized PDAC tumours. This desmoplasia may impede delivery of both conventional chemotherapies and the large-sized monoclonal antibody-based therapeutics. In addition, the proximity of the pancreas to the liver will result in a high liver signal, potentially obscuring the pancreatic tumour signal. Finally, PDAC tumours have a higher tendency to metastasise to the liver, thus the detection of these tumours might be masked by the high liver radioactivity resulting from enhanced hepatic uptake of monoclonal antibodies. While our work has established the first proof-of-concept of feasibility of imaging aberrant p53 in mouse xenografts, we acknowledge the challenges facing the translation of SPECT imaging agent [^{111}In]-DTPA-49A1/H10-TAT to image both enriched high risk PDAC population and patients. This work opens an opportunity to further explore the potential of using small biologics such as cell penetrating peptides, affibodies and small antibody fragments to image p53 abnormal expression in cancer.

We propose the following recommendation could have been included in our *in vivo* experiments. First, since CPP-TAT was conjugated to both the p53 antibody 49A1/H10 and MIgG non-specific control to facilitate cell and nuclear membranes translocation, the inclusion of antibodies without TAT in our *in vivo* experiments could have served as better control for non-specific tumour uptake. Secondly, HT1080 cells express low levels of wild type p53. Wild type p53 levels can be elevated by exposing these cells to DNA damaging agents such as irradiation. The irradiation of HT1080 xenografts expressing wild type p53 would lead to overaccumulation of p53 compared to non-irradiated counterparts. As such, the uptake of [^{111}In]-DTPA-49A1/H10-TAT in irradiated tumours would be expected to be higher than non-irradiated ones, corresponding to p53 levels. This could have provided further evidence of the antibody specificity. Lastly, further validation of [^{111}In]-DTPA-49A1/H10-TAT SPECT imaging of

KPC mice, genetically engineered mouse models of PDAC could have provided robust evidence of the feasibility of imaging p53 in PDAC tumours using radiolabelled monoclonal antibody. KPC mouse models recapitulate the genetics and biology of human cancer making them ideal for preclinical evaluation and testing of new PDAC therapeutics. The emergence of organoid models of human and mouse PDAC has paved way for the robust and accurate means to study the genetics and biology of PDAC and test new drugs (Lee et al., 2016). We propose them as the ideal models for *in vivo* PDAC studies as they fully recapitulate the molecular biology genetics of human PDAC tumours (Boj et al., 2015).

4.5 Conclusion

In this study, we have demonstrated the feasibility of imaging p53 in various cancer mouse xenografts. Our work has shown that [^{111}In]-DTPA-49A1/H10-TAT can accumulate specifically in tumours expressing mutant or wild type p53. Radiolabelled mAbs have already been employed to image intranuclear cancer biomarkers such as p21, p27 and γH2Ax using either PET or SPECT (Cornelissen et al., 2007; J. Knight et al., 2015; J. C. Knight et al., 2017). Hitherto, we note that no other research group has published work on successfully imaging of p53 in cancer using PET or SPECT. We believe that our study has provided a first proof-of-concept methodology to interrogate abnormal p53 expression in cancer using radionuclide molecular imaging modalities. While p53 overexpression in early precancerous lesions and invasive cancer can be targeted for early cancer diagnosis and prognosis evaluation among several cancers, the current p53-based examinations involve ex vivo IHC analysis of biopsy samples are invasive and suboptimal for patient examination. This work provides a solid foundation for molecular imaging of p53 in PDAC and other cancers and should be investigated further and optimised for potential clinical translation to benefit patients.

5 Chapter 5 – *In vitro* screening and validation of p53-targeting small peptides

5.1 Introduction

Peptide-based imaging probes are growingly investigated as potential alternatives to mAb RICs. Peptides possess favourable pharmacokinetics properties because of their small size, which enhance faster blood circulation, higher tissue penetration rates and accumulation in tumours, and faster clearance from nontarget tissues providing high contrast images within hours of *in vivo* administration. Peptides are also less costly to synthesize by solid-phase peptide synthesis (Ducharme & Lapi, 2020). Small peptides have already been used to image several cancer targets using molecular PET and SPECT including HER2, integrin $\alpha_v\beta_3$, and somatostatin receptors (Ducharme et al., 2022; Fani et al., 2012c; Shi et al., 2016).

The use of peptides as cancer imaging agents is beset with the challenge of poor *in vivo* stability due to proteolytic cleavage causing degradation of the peptide, loss of the radionuclide and poor bioavailability (Diao & Meibohm, 2013). Several methods have been developed and successfully used to overcome peptide degradation by proteolytic enzymes and improve *in vivo* stability including incorporation of D-Amino Acids analogues in the peptide sequence, peptide cyclization to protect the N- and C-terminal and PEGylation (Evans et al., 2020). Such modifications have made peptides attractive candidates as cancer therapeutics and molecular imaging.

This chapter aimed to select potential p53-targeting lead peptides for use as SPECT imaging agents to interrogate mutant p53 status in mouse xenografts. We synthesised two peptides based on original sequences from Tal and colleagues' work (**.**

Table *5.1*). The team used phage display technology to screen for mutant p53 targeting reactivating therapeutic peptides. Their lead peptides demonstrated to restore mutant p53 wild type function resulting in dramatic tumour regression in mutant p53 expressing tumour xenografts (Tal et al., 2016). This work aimed to validate the p53-targeting specificity of the two Tal et al lead peptides and use them as alternative p53 SPECT imaging agents. I present in this work the validation of the p53-targeting specificity of the two peptides.

5.2 Material and methods

5.2.1 Cell lines

MiaPaCa-2, HT1080 and H1299 cells were cultured in Dulbecco's Modified Eagle Medium (DMEM) (Thermo Fisher Scientific, UK), supplemented with 10% (v/v) of foetal bovine serum (FBS) (Gibco, USA), 100 units/mL penicillin, 100 ug/mL streptomycin, and 2 mM L-glutamine (Thermo Fisher Scientific, UK). FAMPAC-1 cells were grown in RPMI 1640 Medium (Thermo Fisher Scientific, UK). Cells were maintained in a 5% CO_2 humidified chamber at 37°C. The cells were grown in T-175 flasks (Greiner Bio-One, UK) and passaged when they reached 70 – 80% confluence.

5.2.2 Peptides

The two (Tal et al., 2016) peptides were pCAP 250 (RRHSTPHPD) and pCAP 251 (RRKHNKHRPEPDSDER) here in referred to as Peptide 1 and peptide 2, respectively. The peptides (**Table 5.1**) were commercially synthesised by Cambridge Peptides Limited, UK. For immunofluorescence microscopy, peptides were manufactured with a non-sulfonated Cy5 conjugated to the N-terminal. A GGG linker was added to the peptide N-terminal sequence before Cy5 conjugation.

Table 5.1) p53 targeting peptides. Where Cy5 DBCO (non-sulfonated) is attached to azidohexanoic acid (Azhx) via copper-free click chemistry.

Tal et al Reference	Tal et al Sequence	BC Reference	BC Sequence
pCAP-250	myr-RRHSTPHPD	Peptide 1	Cy5 DBCO]-[Azhx]-[Cys]-GGG-RHSTPHPD-acid
pCAP-221	myr-RRKHNKHRPEPDSDER	Peptide 2	Cy5 DBCO]-[Azhx]-[Cys]-GGG-RRKHNKHRPEPDSDER-acid

5.2.3 Immunofluorescence microscopy

Fluorescent microscopy was employed to determine the localisation of the peptides in the cells in conjunction with anti-total p53 (49A1/H10) monoclonal antibody. The peptide sequences conjugated with Cy5 were peptide 1(Cy5 DBCO]-[Azhx]-[Cys]-GGG-RHSTPHPD-acid) and peptide 2 (Cy5 DBCO]-[Azhx]-[Cys]-GGG-RRKHNKHRPEPDSDER-acid); where Cy5 DBCO (non-sulfonated) is attached to azidohexanoic acid (Azhx) via copper-free click chemistry. Cells (2×10^4) were seeded in 200 µL media in a Falcon 8 well chamber slides and incubated overnight for attachment in a 5% CO_2 humidified chamber at 37°C. The medium was removed, and the chamber washed 1x with sterile PBS before fresh media containing 10 µM of peptide 1 or 2 was added. The peptide treated cells were returned to the incubator and incubated further for 2 h. The medium was removed, and cells were washed with PBS and fixed with 4% (w/v) paraformaldehyde for 10 min. Cells were washed again with PBS and permeabilised with 1% (v/v) Triton X-100 in PBS for 20 min at RT. Non-specific binding was blocked with 2% (w/v) BSA, 5% (v/v) goat serum, 0.3 M glycine in 0.1% (v/v) Triton X-100 in PBST for 1 h at RT. The anti-total p53 antibody (49A1/H10) monoclonal antibody in 100 µL blocking buffer was added to each chamber at a concentration of 10 µg/mL and incubated for 2 h at RT. Cells were washed with PBST for 3 x 5 min. Fluorescently labelled secondary

antibody (goat-anti-mouse H + L Alexa Fluor® 488, 1:1000) diluted in blocking buffer was applied and incubated for 1 h at RT. The chambers were washed again with PBST for 3 x 5 min and a coverslip was mounted using ProLong™ Glass Antifade Mountant with NucBlue™ Stain before imaging. The slides were kept for 24 h to allow drying and then imaged using a Leica SP8 confocal microscope (Leica microsystems, UK) equipped with 63x oil immersion objective lenses and excitation maximum wavelength of 358 nm for DAPI, 499 nm for Alexa Fluor® 488 and 683 nm for Cy5. Images were analysed using ImageJ software where coloc2 analysis was used to obtain the Pearson correlation coefficient R.

5.2.4 Biotin-Peptide pull-down assay

The peptide pull-down assay was performed to confirm the binding of the peptides to mutant and wild type p53 protein. The peptides were manufactured by Cambridge Peptides Limited, UK with a biotin molecule conjugated to the N-terminal as follows: peptide 1 (Biotin-[Cys]-GGG-RRHSTPHPD-COOH) and peptide 2 (Biotin-[Cys]-GGG-RRKHNKHRPEPDSDER-COOH). A GGG spacer was added to the N-terminal of each peptide.

5.2.4.1 Anti-total p53 (49A1/H10) mAb biotinylation

The biotinylation of anti-total p53 (49A1/H10) mAb was carried out using the EZ-Link NHS-PEG_4-Biotinylation kit according to manufacturer's protocol. Anti-total-p53 (49A1/H10) mAb (200 ug) in PBS was reacted with 10-fold molar excess millimoles of NHS-PEG_4-Biotin at RT for 1 h. The reaction products were purified, and buffer exchanged in PBS by centrifuging at 1000 x g for 2 min in a Zeba Spin Desalting Column (5 mL, 7,000 MWCO). The number of biotin moles incorporated on Anti-total p53 (49A1/H10) mAb was determined using HABA assay as directed by the manufacturer's protocol.

5.2.4.2 Assay protocol

The assay was carried using the Pierce™ Biotinylated Protein Interaction Pull-Down Kit (Thermo Fisher Scientific, UK) according to the manufacturers protocol. The streptavidin-coated beads in 50 µL gel slurry were immobilised into spin columns using 250 µL of binding buffer (TBS). 100 µg/100 µL of biotinylated peptide were added to the spin columns with immobilised streptavidin-coated beads. For positive and negative controls, 50 µg of biotinylated anti-total p53 (49A1/H10) monoclonal antibody and 100 µg/100 µL of non-biotinylated anti-total p53 (49A1/H10) monoclonal antibody were added to spin columns, respectively. The spin columns were incubated at 4°C for 4 h with gentle rocking motion on a PCMT Thermoshaker (Gem Scientific, UK). The columns were centrifuged at 1250 × g for 60 seconds to remove the unbound peptide/antibody and then blocked with 250 µL of biotin blocking solution for 30 min at RT. The columns were incubated with 50 µg/100µL of cell lysates at 4°C for 4 h with gentle rocking motion on a PCMT Thermoshaker. After incubation, the columns were centrifuged at 1250 × g for 60 seconds to remove and collect the unbound cell lysate material (flowthrough). The columns were washed with 250µL of wash buffer by centrifuging at 1250 × g for 30 seconds for 5x. The captured protein was eluted by centrifuging at 1250 × g for 60 seconds and collected in collection tubes containing neutralisation buffer. The input lysates, flowthroughs and eluted fractions were analysed by SDS-PAGE followed by immunoblotting with anti-total p53 (49A1/H10) monoclonal primary antibody.

5.2.4.3 SDS-PAGE & western blot

The input lysates, flowthroughs and eluted proteins were fractionated by SDS-PAGE midi-gel electrophoresis XCell4 SureLock™ Midi-Cell system (Thermo Fisher Scientific, UK). The proteins were reduced and linearised by addition of 4x Laemmli SDS Protein Loading Buffer (Thermo Fisher Scientific, UK). The samples were heated at 90°C for 5 min, and 15 uL of 30 µg

of each sample loaded onto a pre-cast 4-12% NuPAGE Bis-Tris gels (Thermo Fisher Scientific, UK). Proteins were separated in NuPAGE MES SDS Running Buffer (20X) (Thermo Fisher Scientific, UK) for 45 min at 200 V. The fractionated proteins were transferred to a pre-activated PVDF membrane using an iBlot 2 Dry Blotting System (Thermo Fisher Scientific, UK), and rinsed in PBS pH 7.4 for five min. The membranes were blocked with 5% (w/v) skim milk powder solution (Sigma-Aldrich, UK) for 1 h at RT and then washed 3 x 5 min with PBST (PBS + 0.1% Tween). The blocked membranes were incubated with the anti-total p53 (49A1/H10) monoclonal antibody (dilution 1:1000) for 2 h at RT, washed 3 x 5 min with PBST and then incubated with Goat anti-Mouse IgG (H+L) Secondary Antibody, HRP (dilution 1:5000) for 1 h. The immunoblots were washed 3 x 5 min in PBS and then developed by addition of chemiluminescent substrate (1:1 solution of Luminol/Enhancer solution and stable peroxidase solution) (Thermo Fisher scientific, UK) for 5 min. The protein bands images were acquired using the C-DiGit Chemiluminescent Western Blot Scanner (LI-COR Biosciences, USA).

5.2.5 MTT Assay to investigate the cytotoxicity of peptides

For each cell line, cells were seeded in triplicates in 100 µL media on a 96-well F-bottom plate and incubated at 37°C, 5% CO_2 overnight. The media were removed and refreshed with 100 µL of increasing peptide concentrations (0 µM, 2.5 µM, 5 µM, 10 µM and 20 µM). Control wells were treated with equivalent concentrations of DMSO as the peptides were dissolved in it. The plates were incubated for 1 h, media refreshed and further incubated for 72 h in a 5% CO_2 incubator at 37°C. The culture media was removed and refreshed with 100 µL fresh media containing 0.5 mg/mL MTT reagent. The plates were incubated in the CO_2 incubator at 37°C for 3 h. The MTT solution was discarded and 200 µL of DMSO added, followed by further incubation in the CO_2 incubator at 37°C for 2 h. The plates were placed in the Tecan infinite

M200 pro plate reader, shaken for 3 min to solubilize the formed purple crystals and absorbances read at a wavelength of 565 nm. The results were used to compute the percentage cell viabilities which were plotted against peptide concentrations.

5.2.6 Statistical analysis

GraphPad Prism v8 (GraphPad Software, CA, USA) was utilised in statistical analysis of MTT data. One way ANOVA was used to find statistical significance between treated and control groups. $P<0.05$ was considered to indicate a statistically significant difference. All experiments were carried out at least in triplicate and presented as mean ± one standard deviation unless otherwise stated.

5.3 Results

5.3.1 Anti-total p53 (49A1/H10) mAb – peptide colocalization assay

Immunofluorescence and peptides staining of cells with different p53 status was carried out to colocalise anti-total p53 (49A1/H10) mAb signal with peptides 1 and 2 signal. HT1080 express wild type p53 while H1299 is a p53 null cell. FAMPAC-1 and MiaPaCa-2 express a structural mutant and contact mutant of p53, respectively. Intensity colocalization analysis was performed to assess the degree of colocalization between the Alexa Flour 488 dye green signal (anti-p53) and Cy5 dye red signal (peptide). The merged confocal laser images of the anti-p53 and peptide Cy5 signal indicated that they exhibited different levels of colocalization strengths across the four cell lines. Pearson's correlation coefficients (R) were obtained to indicate the degree of colocalization. High degree of colocalization had R values of 0.60 to 0.80, while medium level colocalization had R= 0.40 to 0.60 and weak colocalization had R = 0.20 t0 0.40. In FAMPAC-1 cells, peptide 1 and 2 exhibited medium degree of colocalization with anti-total (49A1/H10) mAb, with R values of 0.59 and 0.56, respectively. The R values for

intensity colocalization of the DAPI dye (blue) and anti-total (49A1/H10) mAb (green) were 0.69 (Peptide 1 cells) and 0.75 (peptide 2 cells), respectively (**Figure 5:1**).

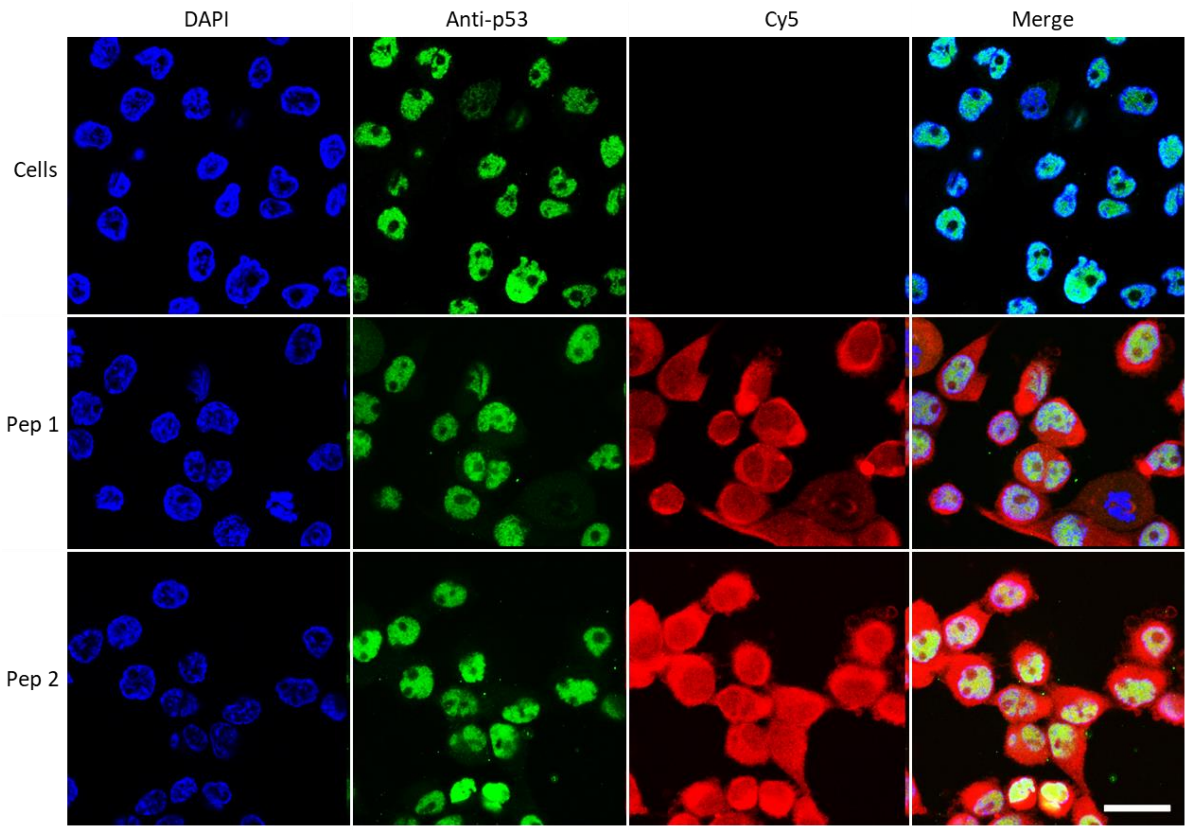


Figure 5:1) FAMPAC-1 cells Immunofluorescence confocal microscopy. Colocalization of anti-total-p53 (49A1/H10) mAb (green) with peptide 1 and 2 (red). DAPI was used to stain the nucleus. Scale bars indicate 20 µm.

In MiaPaCa-2 cells, the colocalization of peptide 1 and 2 revealed weak degree of colocalization with R values of 0.38 and 0.36, respectively. In the same cells, the DAPI dye and anti-total (49A1/H10) mAb colocalization had R values of 0.69 and 0.68, respectively (**Figure 5:2**). In HT1080 cells, both peptide 1 and 2 red signal demonstrated a strong level of colocalization with the green signal with R values of 0.67 and 0.75, respectively, while DAPI and Alexa Fluor 488 had R values of 0.62 and 0.75, respectively (**Figure 5:3**).

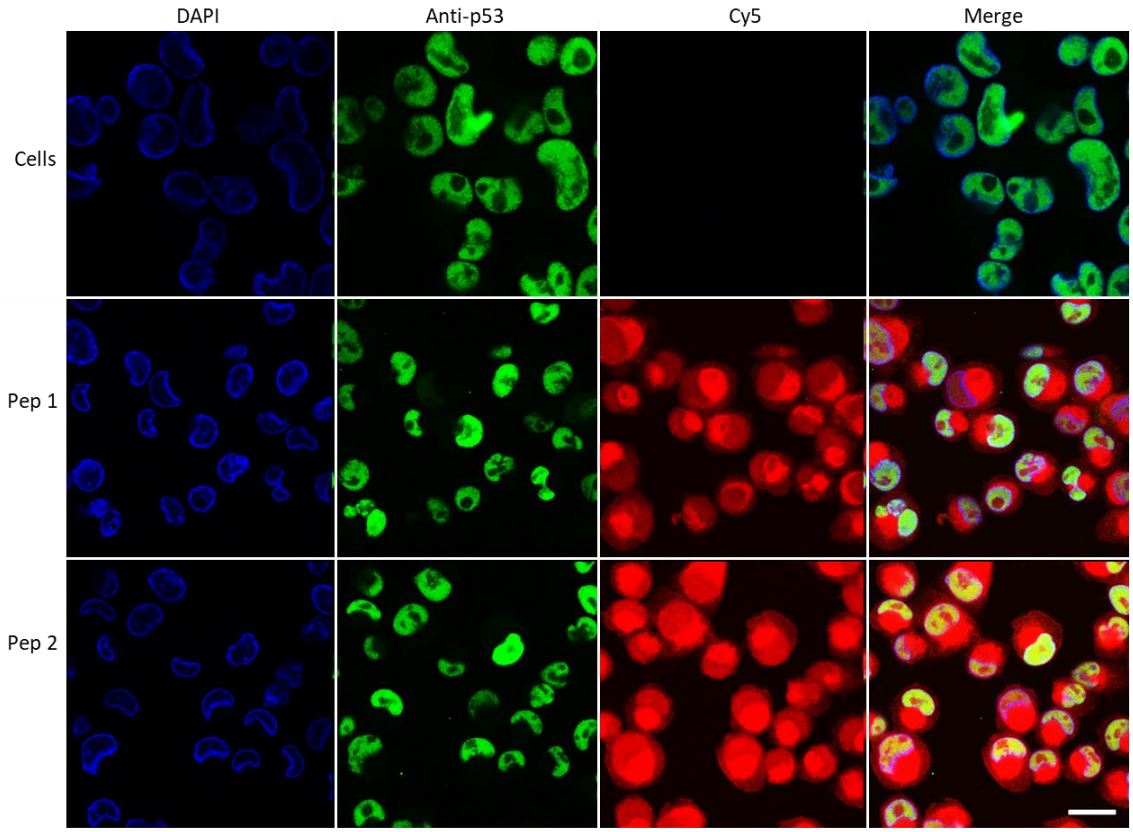


Figure 5:2) MiaPaCa-2 cells Immunofluorescence confocal microscopy. Colocalization of anti-total-p53 (49A1/H10) mAb (green) with peptide 1 and 2 (red). DAPI was used to stain the nucleus. Scale bars indicate 20 µm.

In H1299, which lack p53, the colocalization analysis was performed between DAPI and the peptide signals. Peptide 1 and DAPI had an R value of 0.47 while peptide 2 resulted in an R value of 0.52 (**Figure 5:4A**). The immunofluorescence microscopy colocalization results were confirmed using peptide pulldown assays.

5.3.2 Analysis of peptides interaction with mutant p53 protein by pulldown assay

To fully explore the interaction between total p53 protein and peptides 1 and 2, the biotin-conjugated peptides bound to streptavidin beads coated column were incubated with FAMPAC-1, MiaPaCa-2, HT1080 and H1299 lysates, followed by analysis of the eluted fraction by SDS-PAGE and Western blotting chemiluminescent detection. Anti-total p53 (49A1/H10) mAb was successfully biotinylated with NHS-PEG4-Biotin achieving an average of 2.7 ± 0.73

mmol of biotin molecules per antibody and was used at a positive control. Our data indicated that the biotinylated anti-total p53 (49A1/H10) mAb was able to pull down mutant p53 R175 (FAMPAC-1) and R248W (MiaPaCa-2) and wild type p53 (HT1080).

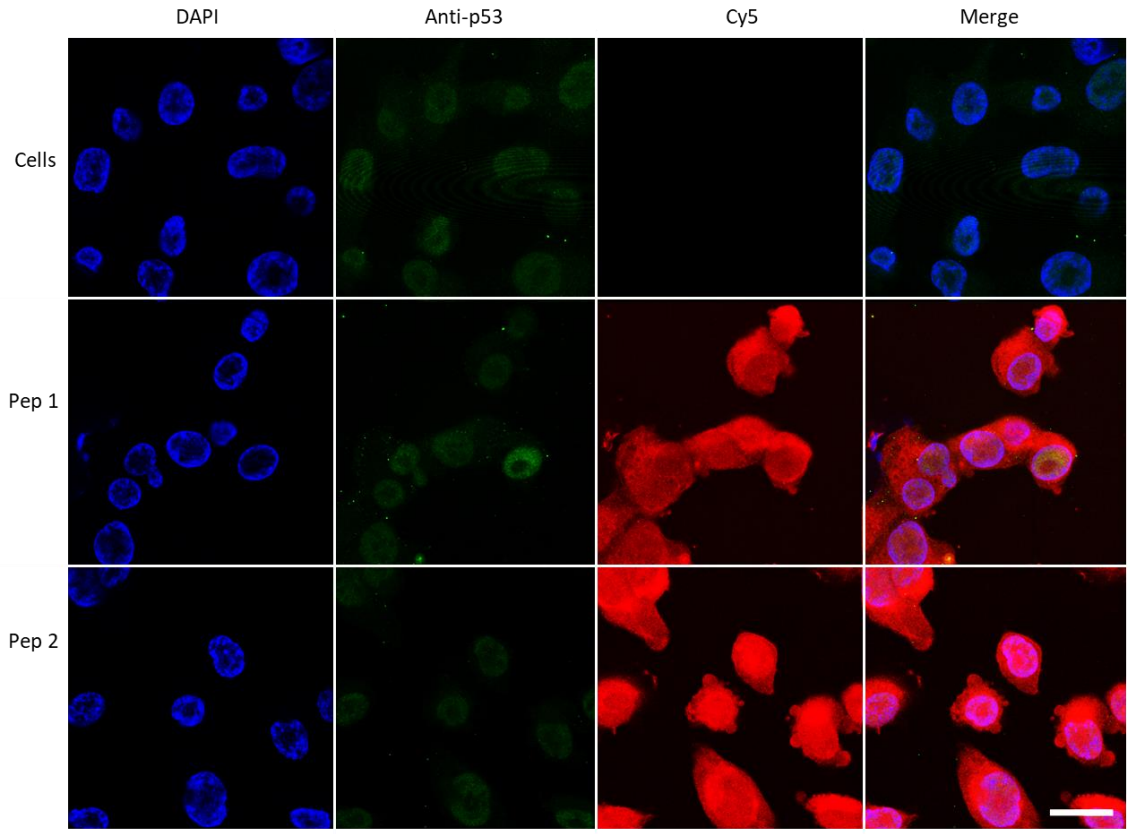


Figure 5:3) HT1080 cells immunofluorescence confocal microscopy. Colocalization of anti-total-p53 (49A1/H10) mAb (green) with peptide 1 and 2 (red). DAPI was used to stain the nucleus. Scale bars indicate 20 µm.

A single protein band with a of molecular weight of approximately 50 kDa was observed in the three pulldowns, however its identity was not confirmed as we did not further analyse by mass spectrometry. Both peptides 1 and 2 and the negative control (non-biotinylated Anti-total p53 (49A1/H10)) did not pulldown p53 protein from FAMPAC-1, MiaPaCa-2 and HT1080 lysates at any detectable levels (**Figure 5:5**).

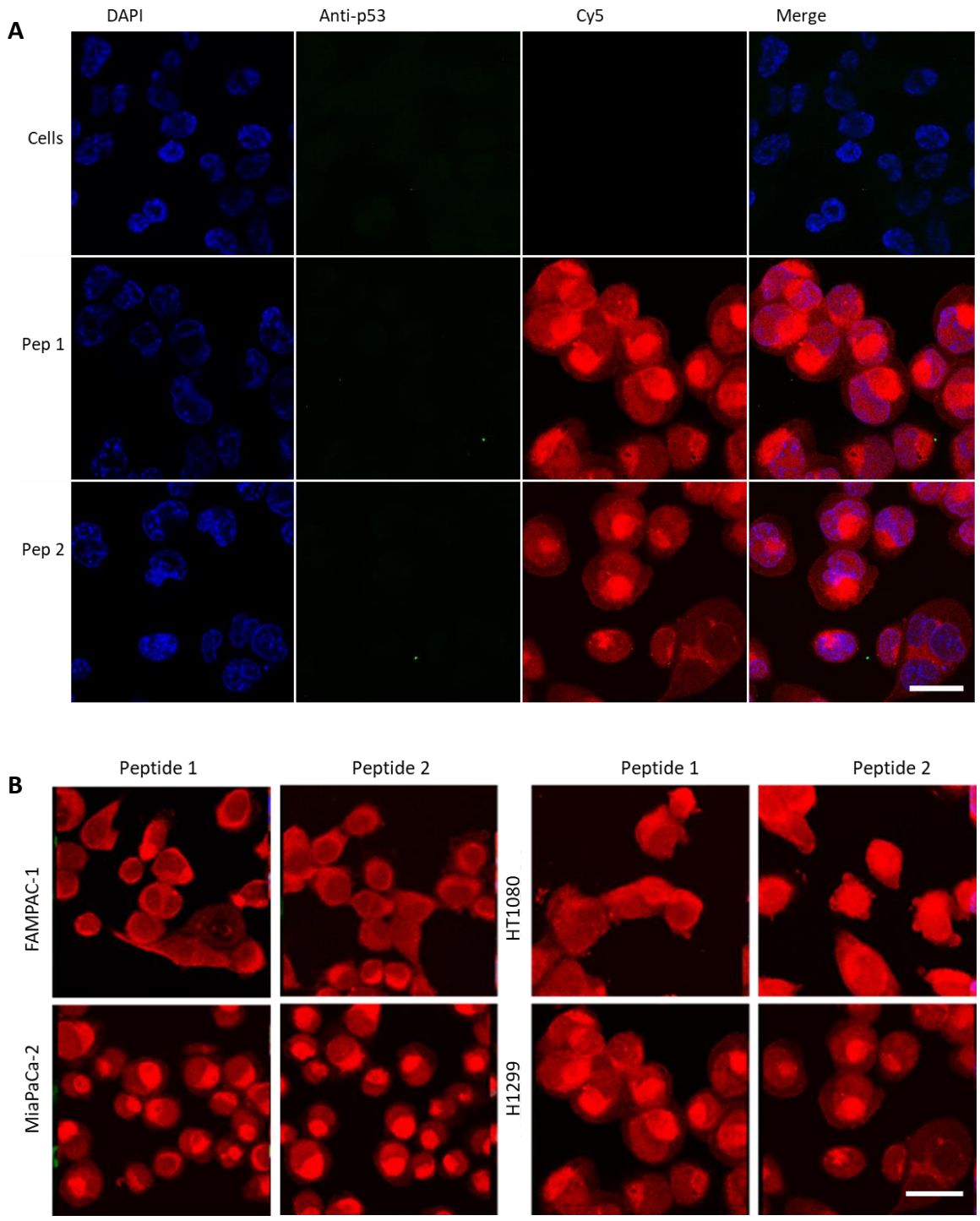


Figure 5:4) H1299 immunofluorescence confocal microscopy and peptide cell uptake. A) Colocalization of anti-total-p53 (49A1/H10) mAb (green) with peptide 1 and 2 (red) in H1299 cells. DAPI was used to stain the nucleus. **B)** uptake and distribution of Cy5-labelled peptides 1 and 2 in FAMPAC-1, MiaPaCa-2, HT1080 and H1299 cells. Scale bars indicate 20 µm.

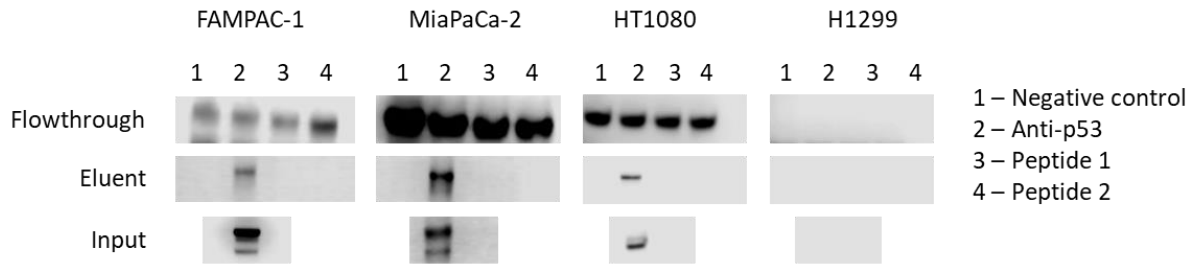


Figure 5:5) Biotin peptide-streptavidin pulldown assay of p53 with cell lysates. Western blot analysis of various fractions (input, eluent, and unbound flowthrough) from pulldown experiments of FAMPAC-1, MiaPaCa-2, HT1080 and H1299 cell lysates. p53 proteins were captured by biotinylated peptide bound on streptavidin beads on the column. Biotinylated anti-total p53 (49A1/H10) mAb was used a positive control.

5.3.3 Peptides cell viability effect

The peptide induced toxicity was evaluated across different concentrations (0 µM, 2.5 µM, 5 µM, 10 µM, 20 µM) on four cell lines with different p53 protein status: FAMPAC-1 (structural mutant R175H), MiaPaCa-2 (contact mutant R248W), HT1080 (wild type) and H1299 (p53 null). In FAMPAC-1 cell lines, peptide 2 displayed a concentration depended significant toxicity (**Figure 5:6**). The cell viability dramatically decreased to 67.82% at 20 µM of peptide 2 concentration ($p < 0.0001$). Peptide 1 treatment of FAMPAC-1 cells resulted in a decline in viability although the effect was not statistically significant at concentrations 2.5 µM (90.47%), 5 µM (84%) and 10 µM (82%), (p values 0.44, 0.10 and 0.07, respectively) (**Figure 5:6**). The cell viability after treatment of FAMPAC-1 cells with 20 µM of peptide 1 significantly declined to 79% ($p = 0.03$). In MiaPaCa-2 cells, both peptides 1 and 2 resulted in decrease in cell viabilities (**Figure 5:6**). While peptide 1 resulted in a concentration dependent decline in percentage cell viabilities: 2.5 µM (90%) , 5 µM (87%), 10 µM (87%) and 20 µM (86%), the effect was not significant (p values 0.36, 0.16, 0.44 and 0.18, respectively. In HT1080 cells, peptides 1 resulted in concentration dependent significant toxicity (**Figure 5:6**) while peptide

2 had no significant effect on viability except at high concentration (20 µM, p = 0.16). H1299 viability significantly decreased in a concentration dependent manner after treatment with peptide 2, while peptide 1 resulted in inconsequential toxicities across all concentrations (**Figure 5:6**). Together, the MTT assays demonstrated that peptide 2 resulted in significant decrease in viability of FAMPAC-1, HT1080 and H1299 cells, with exception of MiaPaCa-2 cells, while peptide 1 produced significant toxicities in HT1080 cells alone.

5.4 Discussion

Development of peptide-based cancer therapeutics is an area of great interest because they possess several advantages over other therapies including easier and cheaper to synthesise, higher target specificity and selectivity, and low immunogenicity and off-target toxicity. In addition, the faster pharmacokinetics of small peptides coupled to easy radiolabelling chemistry make them better candidates for cancer imaging compared to monoclonal antibodies. To qualify as a potential candidate for cancer imaging, peptide imaging agents must display high binding specificity and affinity towards the cancer biomarker of interest. Because of their vulnerability to proteolytic degradation, peptides must also be optimised for their *in vivo* stability and performance to increase their bioavailability.

In this work, I envisioned to evaluate and confirm the p53 binding specificities of the previously validated mutant p53 targeting therapeutic peptides. These peptides were enriched using phage display peptide screening and selected based on their ability to interact with mutant p53 (R175H) and restore its wild-type tumour destruction capacity (Tal et al., 2016).

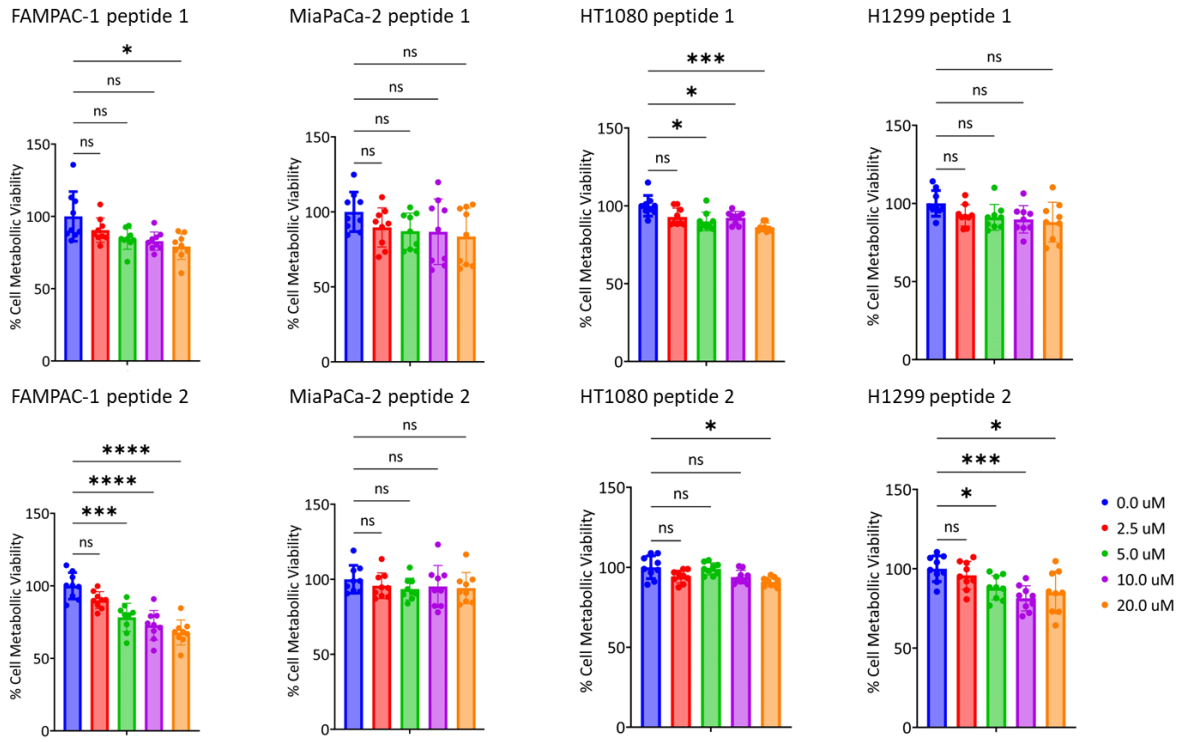


Figure 5:6) MTT assay cell viability results after treatment with peptides 1 or 2. Results are represented as a mean ± SD. Statistical analysis was performed using GraphPad Prism version 8 and a one-way ANOVA test. (ns – not significant, P-values < 0.05 (ns- not significant, *P < 0.05, **P < 0.01, ***P < 0.001).

Two lead peptides from the Tal et al work were evaluated for ability to target total p53 protein using immunofluorescence confocal microscopy, pulldown and MTT assays. The R values were grouped into three categories based on the degree of colocalization between nuclear p53 and DAPI signals in p53 positive cells. Both peptide 1 and 2 exhibited a p53-DAPI R values of above 0.60 in FAMPAC-1, MiaPaCa-2 and HT1080 cells, which indicated a high degree of colocalization. The intensity colocalization assay between p53 monoclonal antibody Alexa Flour 488 dye (green) and Cy5 peptide (red) signals demonstrated heterogeneous R values for both peptide 1 and 2 among the four cell lines. Only p53 wild type cells (HT1080) exhibited stronger colocalization R values for both peptide 1 and 2, which is congruent with Tal et al results who showed using ELISA that, while their peptides reactivated mutant p53 wild type

function, they exhibited strong binding to properly folded wild type p53 protein than to the mutant counterpart (Tal et al., 2016). The interaction of peptide 1 and 2 and mutant p53 in FAMPAC-1 (p53 mutant R175H) revealed a medium degree of colocalization, which was in keeping with Tal et al ELISA results where peptides binding to mutant p53 R175 was 50-80% lower compared to wild type p53. In addition, the colocalization results revealed that the binding of both peptides to mutant p53 protein was mutant type dependent. While both peptide 1 and 2 demonstrated a medium degree of colocalization with structural mutant p53 R175H (FAMPAC-1), they displayed weak colocalization strength with the contact mutant R248W (MiaPaCa-2 cells). In H1299 cells which were used as hosts for transfected mutant and wild type p53 proteins by Tal et al, there was a medium strength colocalization for both peptide 1 and 2. As H1299 cells were p53 null in our assay, these results could mean that the peptides interact with protein target (s) other than p53 protein itself. In all cell lines, there was uptake and staining of both peptide 1 and 2, although a strong Cy5 red signal emanated from the cytoplasm compared to the nucleus where p53 is expressed. The nucleus displayed a weak Cy5 signal (**Figure 5:4B**). We do not know whether the preferential accumulation of the peptides in the cytoplasm was because they lacked sufficient nuclear membrane translocation capacity or they bound preferentially to a protein target expressed in the cytoplasm. Tal et al team did not perform any assays to confirm cellular uptake of the peptides. However, they added a myristic acid at the N-terminal of their peptides facilitating intracellular delivery.

Biotin-peptide pulldown assays demonstrated that neither peptide 1 nor 2 interacted with or captured, either wild type or mutant p53 (**Figure 5:5**). While this was unexpected for HT1080 cells (wild type p53), based on our confocal microscopy colocalization results, these results could be because of a number of plausible reasons. First, the interaction between the

peptides and p53 protein was weak or transient, hence was unable to capture and pulldown the 53 kDa p53 protein. Second, ionic concentration of the wash and elution buffers was too stringent preventing strong peptide-p53 protein interaction. Third, the conjugation of the biotin molecule at the N-terminal of the peptides via a triple lysine linker weakened or abrogated the interaction with p53 protein. Lastly, the amount of peptide used (100 µg) was not sufficient to pull down the p53 protein (Brymora et al., 2001). The latter might not be a possible cause since we tried 150 µg and 200 µg of the peptides to pulldown HT1080 wild type p53 protein and obtained no positive results (results not shown here).

As the Tal et al peptides caused cell toxicity and tumour regression in mutant p53 expressing cells and xenografts, respectively, we evaluated the cancer cells killing ability of the two peptides on the four cell lines using as MTT assay. Peptide 2 displayed concentration dependent significant toxicity in FAMPAC-1, HT1080 and H1299 cells (**Figure 5:6**), which was in line with confocal microscopy results as it demonstrated medium-strong R values in these cells. Peptide 1 resulted in similar toxicity profile in HT1080 and FAMPAC-1 cells, while in H1299, significant cytotoxicity was only seen at a higher concentration of 20 µM. Both peptides displayed no cytotoxic effect in MiaPaCa-2 cells, which is also in line with intensity colocalization analysis results. These results are fit well with the Tal et al. annexin V staining and *in vivo* peptides therapeutic effect study results (Tal et al., 2016).

Given that the biotin-peptide pulldown results revealed that neither of the peptides interact directly with p53 protein, and that both peptides accumulated in and stained p53 null cells (confocal microscopy results, **Figure 5:4A**) and resulted in significant toxicity in H1299 cells, we chose not to proceed with further validation assays because of time constraints. Further

optimisation of pulldown assay results followed by mass spectroscopy analysis may better confirm interaction of the peptides with p53 protein.

5.5 Conclusion

In summary, this chapter attempted to identify potential p53-protein binding peptides using *in vitro* screening assays. Our results revealed no promising candidate for radiolabelling and use as a PET/SPECT p53 imaging agent. While our data contradicts Tal et al. work, it is important to note that none of our validation experiments were employed in their work. Tal and colleagues used Western blot and ELISA assays with p53 mutant specific antibody (PAb240) and wild type p53 antibody (PAb1620) to evaluate the effect of peptide-mutant p53 interaction on the specificity of the two antibodies. In their work, they demonstrated that treatment of mutant p53 proteins (R249S and R175H) with several of their lead peptides restored the binding of PAb1620 antibody on the two p53 mutants and abolished the binding of mutant p53 specific antibody. They also noted that while the PAb1620 antibody is wild type p53 specific, it still showed minimal binding to the mutant proteins, although this was completely abolished when the protein was heated at 60 °C to misfolded state. In addition, they demonstrated using Annexin V staining assay that treatment of cells expressing mutant p53 lead to activation of wild type p53 target genes such as PUMA and p21. This was also demonstrated *in vivo* where the treatment of MDA-MB-231 ($p53^{R280K}$), SKBR3 ($p53^{R175H}$) and SW480 ($p53^{R273H, P309S}$) xenografts lead to dramatic tumour reduction (Tal et al., 2016). These experiments, we believe, were not robust enough to provide evidence of direct peptide interaction with mutant p53 protein. Peptide-antibody colocalisation assay using confocal microscopy and pulldown assay followed by mass spectroscopy would have been the suitable experiments to demonstrate the binding specificity of the peptides. Our work using the two

assays demonstrated that there was no colocalisation of anti-p53 (49A1/H10) mAb with the two Tal et al. peptides. In addition, none of the peptides was able to bind and pulldown mutant or wild type p53 protein.

Although this project was unsuccessful, the lessons learnt from the work can inform future work to screen for a p53-targeting peptide imaging agent. We propose the use of phage display technology to screen for a novel p53 targeting small peptides and selection of lead candidates for molecular imaging. As the N-terminal region of p53 is less mutable, using a peptide from this region as a bait could help to identify peptides that bind to total p53 protein. An alternative approach could involve using the anti-total (49A1/H10) mAb p53 binding domain sequence to rationally design an anti-p53 binding affibody. The anti-p53 binding affibody could serve as a template to construct a phagemid library for screening for best candidates using phage display methodology. The small size of affibodies (<7 kDa), picomolar affinity, ease of engineering, proteolytic and thermostability, and faster pharmacokinetics make them promising molecular imaging agents than antibodies and small peptides (Frejd & Kim, 2017).

6 Overall discussion and future work

PDAC incidence are alarmingly increasing yet majority of the patients are beset with the challenge of late diagnosis and resistant to standard treatments, resulting in overall poor prognosis and a five-year survival rates of less than 8%. The lack of early diagnosis methods necessitates an urgent need for research to identify and validate novel PDAC screening biomarkers and diagnostic agents. The work presented in this thesis describes the validation of a novel p53 monoclonal antibody radionuclide imaging agent for SPECT imaging of p53 status in PDAC xenografts. Our work has established the first successfully proof-of-concept of feasibility of imaging p53 in PDAC which opens an opportunity for further validation and clinical translation.

TP53 is the most consequential gene in humans, and it encodes the p53 protein that function to modulate diverse cellular processes involved in averting detrimental cellular and genomic events capable of instigating malignant transformation. Wild type and mutant p53 multifarious and contrasting roles in normal and cancer cells, respectively, are a reminiscent of the long controversial scientific detour by multiple research groups that led to p53 discovery in 1979 (Soussi, 2010). Wild type p53 acts as a transcriptional factor involved in regulating a plethora of signalling pathways that operate to maintain the integrity of the genome, thus preventing cancer development. Functional p53 protein responds to diverse cellular stressors such as DNA damage, hypoxia, and oncogene activation, leading to its activation and sequence-specific transcription of a plethora of genes that function to halt/inhibit cell cycle progression (p21), promote senescence (p21), or induce apoptosis (PUMA and NOXA) (Brady & Attardi, 2010). Each of these downstream p53 cellular outcomes plays important role in suppressing abnormal cell proliferation and malignant transformation.

The loss of wild type p53 function is a sine qua non of malignant transformation and cancer development. p53 role in preventing cancer development is evident among Li Fraumeni syndrome patients who develop cancers at a rather early age including breast cancer, osteosarcoma, and soft tissue sarcomas. Li Fraumeni syndrome is an autosomal dominant disorder caused by germline mutations in TP53, which predispose individuals to cancer development. In addition, mice devoid of p53 exhibit extreme susceptibility to developing lymphomas and sarcomas (Freed-Pastor & Prives, 2012). Somatic mutations of p53 are the most common genetic abnormalities in humans occurring in more than half of cancers. The tumours suppressive role of p53 in normal cells is reversed in cancer as the mutant counterpart acts as an oncogene rather than a tumour suppressor protein. p53 wild type function are lost through loss of heterozygosity leading accumulation of stable mutant p53 protein with tumour enhancing traits. The newly mutant protein acquire dominant-negative effect and gain-of-function oncogenic capabilities, that promote tumours aggressiveness, enhance metastasis, and therapy resistance (Mantovani et al., 2018). Mutant p53 is more frequently found in ovarian cancer, pancreatic cancer and non-small cell lung cancer, and hotspot mutants such as R175H, R248W and R273H are overly expressed in these cancers and associated with poor prognosis among patients. In PDAC, p53 is mutated in approximately 75% of PanIN-3 lesions and invasive tumours. Mutant p53 is often overly expressed among PDAC patients and associated with chemo/radiotherapy resistance and overall poor prognosis (75%) (Blandino & di Agostino, 2018; Koorstra et al., 2009). The high penetrance and overexpression of mutant p53 underscores the need to develop p53-based therapeutics for diagnosis and stratification of patients during treatment.

Mutant p53 in cancer is currently being explored for therapeutic targeting. Most therapeutic strategies have focused on either restoring wild type p53 function or degrading mutant p53

in cancer. Among the promising efforts is the use of small molecules to targeting mutant p53 for wild-type function restoration and induction tumour suppressive function. PRIMA-1^{MET}, a small molecule, binds to p53 in a sequence specific restoring the wild type of function. It has already demonstrated high level of potency in preclinical studies and is currently under phase I/II clinical trials for ovarian cancer, prostate cancer, and haematological cancers (Hu et al., 2021). In addition, mutant p53 has been targeted for wild type function restoration using small peptides. Tal et al. and colleagues used to phage display to enrich mutant p53 reactivating peptides. In their work, they demonstrated that the lead peptides were capable of upregulating wild type p53 cell cycle arrest and apoptosis target genes. These peptides resulted in cell death upon treatment of mutant p53 expressing cancer cells. In addition, the peptides lead to dramatic tumour regression of mutant p53 xenografts. Their conclusion was, these peptides were mutant p53 binders and reactivators (Tal et al., 2016). Incongruent with their findings, our work in chapter 4 demonstrated that two of their lead peptides were not mutant/wild type p53 binders, emphasizing the need to select the best techniques for evaluating direct interactions between a protein and their targeting molecules.

Hitherto, no work has been published on biologics or compounds developed to target p53 for imaging using PET or SPECT. This remains a setback for many cancer patients who could benefit from early detection through PET screening of enriched high-risk individuals predisposed to developing cancers of the pancreas, ovary, lungs, and colon. Mutant p53 imaging could prove invaluable for treatment stratification enabling patients to receive drugs likely to benefit them. There is, therefore, an urgent need to develop molecular imaging agents targeting p53 for PET imaging.

PET and SPECT are the epitome of cancer imaging because of their unrivalled sensitivities, enabling the detection of cellular and molecular events at picomolar concentrations. However, the full potential of these molecular imaging modalities remain to be realised because of lack of better biomarkers and targeting agents, as well limited affordability, and accessibility due to high cost. While the latter problem is an economic problem that can be solved by making PET/SPECT more cost-effective and enabling people to have access to medical insurance, the former challenges are of most urgency and should be addressed by researchers. In the context of PDAC, there is still lack of a representable and reliable biomarker for early diagnosis. Several biomarkers are currently under investigation including MUC-1, MUC-5, CEA, CEACAM-6 and p53, each presenting its own limits and strengths (Brezgyte et al., 2021; W. H. Zhang et al., 2020). The tumour suppressor protein p53 is of keen interest for PDAC diagnosis because of two main reasons: (i) it is mutated in approximately 75% of PDAC patients, with majority of the mutations being missense that overexpress the abnormal p53 protein compared to normal wild type p53 levels, and (ii) p53 mutations and overexpression occur in PanIN-3s and invasive PDAC making it an ideal biomarker to differentiate inconsequential precancerous lesions (PanIN-1 and PanIN-2) from the consequential invasive ones (Koorstra et al., 2009). Targeting p53 aberrant expression in PDAC using PET/SPECT requires an imaging agent possessing high p53 binding affinity and specificity, as well as an ability to translocate across the cell and nuclear membranes and localise within the nucleus. An ideal p53 targeting agent should be able to bind to all forms of p53 because of the high frequency and heterogeneous nature of p53 mutations. Monoclonal antibodies targeting total p53 represent the most potent and promising biologics because of their excellent binding kinetics and specificities, known pharmacokinetics profile and established methods of production and validation via hybridoma technology. This work aimed

to validate a novel monoclonal antibody targeting total p53 in PDAC. The antibody was radioconjugated with CPP-TAT and DTPA for indium-111 radiolabelling and employed to image p53 mouse xenografts *in vivo* using SPECT.

The initial aim (Chapter 2) of this work was to validate a novel anti-total p53 mAb from several p53 mouse antibodies produced in collaboration with the Banham group at the NDCLS, University of Oxford. Previous work from our group (not published) employed a commercially available mouse anti-p53 (1C12) mAb (Cell Signalling Technology, UK) to image p53 which yielded suboptimal results due to batch-to-batch variation. Coupled to high cost, it became challenging to optimise the study protocols and use the same antibody in the repeat experiments. The production of an inhouse total-p53 binding antibody enabled us to have control over the quantity and quality of antibody produced at a relatively insignificant cost. Our newly produced and validated antibody anti-total p53 (49A1/H10) mAb displayed high p53 binding specificities with nanomolar affinities on structural p53 mutant (FAMPAC-1), contact p53 mutant (MiaPaCa-2), and wild type p53. While our the novel p53 49A1/H10 mAb demonstrated excellent properties, additional validation assays are needed before the antibody is considered for commercialisation or human use. First, the use of RNA interference (RNAi) or CRISPR knockdown/out p53 cell lines could help provide robust evidence on the specificity of the antibody. The reduction or elimination of p53 protein followed by anti-total p53 (49A1/H10) mAb staining would provide more information on its specificity and crossreactivity. In addition, the antibody specificity and selectivity should be evaluated on both mouse and human tissues samples to qualify for immunohistochemical assays. Lastly, the anti-total p53 (49A1/H10) mAb should be isotyped to determine its subclass. In all our studies, we used Mouse (G3A1) mAb IgG1 (Cell Signalling Technology, UK) as our non-specific control. While this served well to achieve the project's overall aim, we do not have any

evidence that anti-total p53 (49A1/H10) mAb is of the same subclass as Mouse (G3A1) mAb IgG1. Knowledge of the subclass of the p53 antibody would be critical in helping to select the correct isotype control. The use of the right isotype control helps to distinguish the true antibody signal from non-specific background staining and limit off-target interactions with dyes conjugated to the antibody (Choosing an Isotype Control Antibody | Abcam, n.d.).

The anti-total p53 (49A1/H10) mAb was employed to determine the expression levels of p53 hotspot mutants among PDAC cell lines. The four p53 hotspot mutants (R175H, R248W, Y220C and R273H) were overly expressed compared to normal pancreas p53 levels, although displaying heterogenous expression levels. Mutant p53 have been shown to be overexpressed in different cancer types, with majority of research focusing on a single gain-of-function mutants such as R175H, R248Q/W and R273H (Chiang et al., 2021; Hassin et al., 2022). Mutant p53 stabilisation and overexpression result from loss of negative autoregulatory MDM2/MDMX interactions as well as interaction with small heat shock proteins such as HSPB1 and HSPB5 (Choi et al., 2019; Inoue et al., 2012). p53 overexpression in human tumours was discovered in the last quarter of the 20th century when the protein was first discovered (Soussi, 2010). Since its discovery in 1979, the focus of p53 research shifted to understanding its function and pathways in normal and cancerous cells, with less focus on therapeutic targeting. It was not until the last decade that research started focusing on targeting overexpressed mutant p53 protein for cancer therapy. Several groups have employed small peptides and small molecules to target gain-of-function mutants R175 and R248Q/W for restoration of wild type tumour suppressive capabilities with successes at the preclinical stage (Lewis & Taylor, 2015; Tal et al., 2016). The high frequency and overexpression of p53 missense mutations in human precancerous lesions and invasive cancers necessitate urgent efforts for therapeutic targeting for cancer diagnosis and treatment. While our study

confirmed that p53 hotspot mutants are highly overexpressed in PDAC, we propose the following should be done in the future to confirm aberrant p53 expression as a reliable biomarker for screening enriched high risk PDAC population. The evaluation of p53 protein expression levels should be broadened to all forms of p53 missense mutants in PDAC. Approximately 1,135 p53 missense mutations have been documented in cancer which confer loss of heterozygosity, gain-of-function, or dominant negative effect capabilities in cancers (Kato et al., 2003). There is no robust evidence of the p53 expression status in PDAC hence the need to evaluate p53 expression status across a representable population of missense mutants in PDAC. The expression status should be correlated with PDAC development stages and clinical data to make meaningful conclusions on the utility of p53 targeting in PDAC as an early diagnosis and prognosis biomarker. In addition, it has been shown that protein copy number per cell can influence the sensitivity and detection limit of both PET and SPECT. The lower abundance thresholds for targeting extracellular and intracellular epitopes using SPECT have been predicted to be 8000 and 240,000 copies per cell, respectively (Veal et al., 2021). While this can be affected by the type and affinity of imaging agent used (mAb, antibody fragments or small peptides) and sensitivity of imaging modality (PET more sensitive that SPECT) and tumour inherent characteristics such as EPR effect, it is crucial that the lowest mutant p53 copy number in PDAC is determined. Future experiments should aim to address this gap to provide clear evidence of the detection limit of overexpressed p53 mutants in cancer.

The second aim of this study focused on radioconjugating anti-total p53 (49A1/H10) mAb to CPP-TAT and indium-111 radionuclide to produce a total p53 targeting mAb SPECT imaging agent. We demonstrated that addition of 7-fold molar excess of DBCO-N_3 to p53 mAb 49A1/H10 or MIgG led to attachment of approximately 5 DBCO molecules on the mAb. This

was in line with previous work from our group which demonstrated that approximately 5 DBCO molecules per mAb enabled CPP-TAT-N_3 and DTPA-N_3 conjugation without significantly altering the binding affinities and pharmacokinetics profile of the antibody (Veal et al., 2021). Indeed, both western blot and radioimmunoassay data showed that the total p53 binding specificities and affinity of anti-p53-49A1/H10 mAb remained unchanged after conjugation to TAT and DTPA chelator. The DBCO-N_3 radioconjugation method is an improvement of the conventional EDC-NHS methods as it provides for quality control of the reaction and the number of DTPA and TAT molecules attached to the antibody. In addition, this method overcomes the possibility antibody-to-antibody and CPP-TAT-to-DTPA crosslinking which results in heterogeneous RICs with suboptimal binding kinetics affecting *in vivo* performance (Dennler et al., 2015). However, the DBCO-N_3 does not provide the exact number of CPP-TAT and DTPA per antibody, and one cannot tell the exact mAb position where the payloads are added due to lack of site-specific conjugation. Several site-specific mAb conjugations techniques have been developed including coupling of radionuclide chelators and CPPs on engineered unnatural amino acids, N297 glycans and short peptide tags, which generate more homogenous RICs compared to conventional methods (Q. Zhou, 2017). We believe future work should explore these novel radiolabelling methods to produce homogeneous and reproducible radiolabelled mAbs.

The addition of CPP TAT enabled significant cell uptake of RICs confirming the usefulness of using a CPP to deliver large therapeutic cargos into the cells. Our data showed that over 2.5% of the RIC was delivered into the cells, which is more than two-times the amount of TAT-conjugated mAb that enters the cell when labelled using the traditional EDC/NHS method. It is not evident whether the DBCO-N_3 method increases non-specific TAT-conjugated antibody and how of much of it gets into the nucleus to interact with p53 or stay in cytoplasm and

endosomes. An immunofluorescence confocal microscopy assay can help to shed light on the intracellular localisation and distribution of the TAT-conjugated antibody after cellular uptake. The inclusion of RNA interference (RNAi) or CRISPR knockdown/out p53 cell lines cell uptake assays would also provide evidence to target interaction and non-specific accumulation in the nucleus. The retention assays demonstrated that p53 49A1/H10 mAb was significant retained in MiaPaCa-2 and HT1080 cells and not in H1299 p53 null cells, suggesting evidence of p53-specific interaction and rapid non-specific cellular exclusion of MIgG. Hitherto, the mechanisms of TAT-mAb conjugates entry into the cells, endosomal escape and exclusion from the cells remain unclear. TAT has been proposed to bind to the plasma membrane heparan sulfate proteoglycans followed by entry into the cells by macropinocytosis (Palm-Apergi et al., 2012). Once the TAT-conjugated cargo is internalised into the cells, it must escape the endosome and released to reach its intended target. Several proposed mechanisms of endosomal escape include proton sponge hypothesis (Sonawane et al., 2003), direct endosomal membrane translocation via pore formation and membrane destabilisation (Rehman et al., 2013) and promotion of endosomal membrane budding to form smaller sub-vesicles that collapse to release the TAT-cargo compound (Qian et al., 2016). It still remains unknown how the non-specific antibody is released from the cells after entry. Further research into elucidating these mechanisms shall help to optimise mAb therapeutics delivery into the cells and accelerate the potential clinical translation.

Indium-111 radionuclide was selected for use in this study because of availability, possession of preclinical SPECT gamma camera and because its half-life matches that of mAb residence time in the system. While SPECT offers the advantage of affordability and accessibility, PET has unrivalled sensitivity and spatial resolution and is more quantitative than SPECT (Wernick & Aarsvold, 2004). The use of PET and the positron emitting radionuclide Zirconium-89 have

already been used to successfully image several cancer epitopes including epidermal growth factor2 (HER2), prostate specific membrane antigen (PSMA) and PDL1 (Even et al., 2017; Kikuchi et al., 2017).

In chapter 4, we showed the feasibility of SPECT imaging of both mutant and wild type p53 using indium-111 labelled mAb. Two non-PDAC cell lines (HT1080 and H1299) were used in this study for logistical and time-factor reasons, as we could not get hold of SW1990 cells (PDAC p53 wild type cell line) more than 9 months after purchase while AsPC-1 (PDAC p53 null cells) had problems of growing in our tissue culture. The two cell lines were replaced with HT1080 (fibrosarcoma p53 wild type) and H1299 (non-small cell lung cancer p53 null), which are known and widely used cancer cell lines that enabled us to accomplish our study objective. However, because cancers are highly heterogenous, it is likely that the tumour uptake profiles in these cells might not be the same as the foregone PDAC counterparts. Future study s hould aim to include SW1990 and AsPC-1 xenografts. Nonetheless, our results showed that in both MiaPaCa-2 and HT1080 xenografts, there was statistically significant time-dependent higher tumour uptake of [^{111}In]-DTPA-49A1/H10-TAT compared to non-specific control [^{111}In]-DTPA-MIgG-TAT, suggesting evidence of p53 and tumour specificity. A similar tumour uptake profile was observed between the highly expressing mutant p53 xenografts (MiaPaCa-2) and lowly expressing wild type p53 (HT1080 xenografts). It was expected that the uptake of [^{111}In]-DTPA-49A1/H10-TAT in the two tumours would correlate with p53 levels as revealed in the *in vitro* studies. It is well known that enhanced tumour vasculature and permeability (EPR effect), promotes nonspecific tumour uptake of large therapeutics (above 40 kDa) including mAbs, a common trait of most solid tumours (Wu, 2021). The EPR effect has been explored for effective delivery of nanodrugs reaching several folds higher in tumours than plasma and nontarget tissues (Longmire et al., 2008; Subhan et al., 2021). While the nonspecific

accumulations of nanodrugs and mAbs in tumours can improve therapeutic efficacy, this is a double-edged sword for cancer imaging. The lack of clearance of non-specific imaging agents can lead to wrong conclusions about the pattern and levels of biomarker expression which can result in overdiagnosis as seen in the HT1080 tumours. In addition, the EPR effect can also lead to false positives during imaging, especially in cancers that do not express the biomarker of interest as exemplified by H1299 xenograft in our study.

Several methods have been proposed and trialled to solve the challenge of nonspecific solid tumour uptake of cancer imaging therapeutics. The use of smaller antibody fragments, affibodies and small peptides with faster tumour diffusive penetration and rapid clearance from nontarget regions is a promising strategy for delivery of cancer imaging agents in tumours. Radiolabelled PET/SPECT peptides, antibody fragments and affibodies have already been explored to image cancer cells displaying faster blood and non-target tissues clearance, high tumour-to-normal tissues uptake ratios and better biodistribution profile than large biologics (X. Li et al., 2020; Xenaki et al., 2017; Xu et al., 2020). As such, we propose that future *in vivo* PET/SPECT imaging of p53 protein should exploit the promising features of small antibody fragments, peptides, and scaffolds as imaging tracers. In addition, small imaging tracers are metabolised and cleared from the system by the rapid renal metabolism system (Huang et al., 2020; Nygren, 2008). The proximity of the pancreas to the liver coupled to its dense desmoplastic stroma poses a challenge to the use of mAb RICs to image PDAC. The high liver radioactivity signal is expected to mask both the pancreatic cancer signal as well us liver metastasis signal. The PDAC stroma is a huge obstacle to effective therapeutic delivery, making it challenging to target PDAC biomarkers for diagnosis as well as contributing to therapy resistance (Jiang et al., 2020). Therefore, small sized PET/SPECT imaging tracers

should be explored in future efforts to effectively target PDAC for diagnosis and therapeutic delivery.

Small peptide-based radiopharmaceuticals are making significant progress in the field of cancer imaging. Peptides' improved pharmacokinetics profiles guarantees faster tumour accumulation and intratumour distribution, and rapid clearance from circulating system and non-target tissues. Peptides have already been employed to target neuroendocrine tumours for radionuclide imaging and therapy (Fani et al., 2012c; Naik et al., 2022). Tal et al employed phage display screening to fish and enrich mutant-p53 reactivating peptides demonstrating tumour killing potential in mutant p53 mouse xenografts (Tal et al., 2016). Two of the best lead peptides from Tal et al work were chosen and their ability to bind and interact with total p53 protein evaluated in this study in chapter 5. None of the two peptides showed direct binding to either wild type or mutant p53 protein. While we could not proceed with the peptide projects, we believe further optimisation of assay conditions are needed. In addition, a new phage display screening using p53 N-terminal peptide as a peptide would be the most potent approach to help identify a better total p53-targeting lead candidate for further optimisation and radioconjugation for PET/SPECT imaging.

Peptides are often beset with the challenge of *in vivo* instability due to proteolytic cleavage. Rapid clearance from the blood often results in reduced tumour accumulation (Marqus et al., 2017). These two challenges have been overcome through cyclisation of peptides, N or C-terminal modifications, PEGylation and use D- or unnatural amino acids that are more withstanding to enzymatic degradation (Yao et al., 2018). Therefore, identification and optimisation of binding and pharmacokinetics profile of novel total p53 targeting peptides would overcome the limitations faced in the current study.

In conclusion, this study has explored the feasibility of using a radionuclide labelled mAb to image total p53 using SPECT. We have shown that anti-total p53 (49A1/H10) mAb is capable of binding to both mutant forms and wild type p53 with high specificity and nanomolar affinity, and that hotspot mutant p53 are heterogeneously overexpressed in PDAC. We also demonstrated *in vitro* and *in vivo* that [^{111}In]-DTPA-49A1/H10 mAb is capable for intracellular uptake resulting in significant cellular and tumour uptake in p53 expressing tumour xenografts compared to non-specific control. We propose further experiments with [^{111}In]-DTPA-49A1/H10 mAb in KPC mouse models and human and mouse PDAC organoid models to exploit the full potential and utility of this molecular imaging tracer for PDAC imaging. Mutant p53 imaging in PDAC will likely offer new hopes for PDAC patients and clinicians. Additional optimisation of peptide screening experiments and/or phage display techniques are needed to identify better p53-targeting lead peptides.

7 Bibliography

Adel. Nelly. (2019). Current Treatment Landscape and Emerging Therapies for Pancreatic Cancer. *The American Journal Of Managed Care*, *25*(1), S3–S10.

A-Kader, H. H., & Ghishan, F. K. (2012). The Pancreas. *Textbook Of Clinical Pediatrics*, 1925-1936.

Alexandrova, E. M., Mirza, S. A., Xu, S., Schulz-Heddergott, R., Marchenko, N. D., & Moll, U. M. (2017). P53 Loss-Of-Heterozygosity Is A Necessary Prerequisite For Mutant P53 Stabilization And Gain-Of-Function *In Vivo*. *Cell Death & Disease 2017 8*(3), 1-5.

Altunay, B., Morgenroth, A., Beheshti, M., Vogg, A., Wong, N. C. L., Ting, H. H., Biersack, H. J., Stickeler, E., & Mottaghy, F. M. (2021). Her2-Directed Antibodies, Affibodies And Nanobodies As Drug-Delivery Vehicles In Breast Cancer With A Specific Focus On Radioimmunotherapy And Radioimmunoimaging. *European Journal Of Nuclear Medicine And Molecular Imaging*, *48*(5), 1371-1389.

Amato, E., Molin, M. D., Mafficini, A., Yu, J., Malleo, G., Rusev, B., Fassan, M., Antonello, D., Sadakari, Y., Castelli, P., Zamboni, G., Maitra, A., Salvia, R., Hruban, R. H., Bassi, C., Capelli, P., Lawlor, R. T., Goggins, M., & Scarpa, A. (2014). Targeted Next-Generation Sequencing Of Cancer Genes Dissects The Molecular Profiles Of Intraductal Papillary Neoplasms Of The Pancreas. *The Journal Of Pathology*, *233*(3), 217–227.

Amirtharaj, F., Venkatesh, G. H., Wojtas, B., Nawafleh, H. H., Mahmood, A. S., Nizami, Z. N., Khan, M. S., Thiery, J., & Chouaib, S. (2022). p53 reactivating small molecule PRIMA-1MET/APR-246 regulates genomic instability in MDA-MB-231 cells. *Oncology Reports*, *47*(4), 1–9.

Antibodypedia. (N.D.). Retrieved October 31, 2022, From Https://Www.Antibodypedia.Com/

Aubrey, B. J., Kelly, G. L., Janic, A., Herold, M. J., & Strasser, A. (2017). How Does P53 Induce Apoptosis And How Does This Relate To P53-Mediated Tumour Suppression? *Cell Death & Differentiation*, *25*(1), 104–113.

Ayo, A., & Laakkonen, P. (2021). Peptide-Based Strategies For Targeted Tumor Treatment And Imaging. *Pharmaceutics*, *13*(4), 481.

Baptiste, N., Friedlander, P., Chen, X., & Prives, C. (2002). The Proline-Rich Domain Of P53 Is Required For Cooperation With Anti-Neoplastic Agents To Promote Apoptosis Of Tumor Cells. *Oncogene*, *21*(1), 9–21.

Basturk, O., Hong, S. M., Wood, L. D., Adsay, N. V., Albores-Saavedra, J., Biankin, A. V., Brosens, L. A. A., Fukushima, N., Goggins, M., Hruban, R. H., Kato, Y., Klimstra, D. S., Klöppel, G., Krasinskas, A., Longnecker, D. S., Matthaei, H., Offerhaus, G. J. A., Shimizu, M., Takaori, K., … Furukawa, T. (2015). A Revised Classification System And Recommendations From The Baltimore Consensus Meeting For Neoplastic Precursor Lesions In The Pancreas. *American Journal Of Surgical Pathology*, *39*(12), 1730–1741.

Blandino, G., & Di Agostino, S. (2018a). New Therapeutic Strategies To Treat Human Cancers Expressing Mutant P53 Proteins. *Journal Of Experimental & Clinical Cancer Research*, *37*(1), 1–13.

Boj, S. F., Hwang, C. Il, Baker, L. A., Chio, I. I. C., Engle, D. D., Corbo, V., Jager, M., Ponz-Sarvise, M., Tiriac, H., Spector, M. S., Gracanin, A., Oni, T., Yu, K. H., Van Boxtel, R., Huch, M., Rivera, K. D., Wilson, J. P., Feigin, M. E., Öhlund, D., … Tuveson, D. A. (2015). Organoid Models Of Human And Mouse Ductal Pancreatic Cancer. *Cell*, *160*(0), 324.

Brady, C. A., & Attardi, L. D. (2010). p53 at a glance. *Journal of Cell Science*, *123*(15), 2527.

Brennan, D. D. D., Zamboni, G. A., Raptopoulos, V. D., & Kruskal, J. B. (2007). Comprehensive Preoperative Assessment Of Pancreatic Adenocarcinoma With 64-Section Volumetric Ct. *Radiographics*, *27*(6), 1653–1666.

Brezgyte, G., Shah, V., Jach, D., & Crnogorac-Jurcevic, T. (2021). Non-Invasive Biomarkers For Earlier Detection Of Pancreatic Cancer—A Comprehensive Review. *Cancers*, *13*(11), 1-25.

Brigati, C., Giacca, M., Noonan, D. M., & Albini, A. (2003). Hiv Tat, Its Targets And The Control Of Viral Gene Expression. *Fems Microbiology Letters*, *220*(1), 57–65.

Brymora, A., Cousin, M. A., Roufogalis, B. D., & Robinson, P. J. (2001). Enhanced Protein Recovery And Reproducibility From Pull-Down Assays And Immunoprecipitations Using Spin Columns. *Analytical Biochemistry*, *295*(1), 119–122.

Butler, J. S., & Loh, S. N. (2003). Structure, Function, And Aggregation Of The Zinc-Free Form Of The P53 Dna Binding Domain†. *Biochemistry*, *42*(8), 2396–2403.

Capasso, M., Franceschi, M., Rodriguez-Castro, K. I., Crafa, P., Cambiè, G., Miraglia, C., Barchi, A., Nouvenne, A., Leandro, G., Meschi, T., De' Angelis, G. L., & Di Mario, F. (2018). Epidemiology And Risk Factors Of Pancreatic Cancer. *Acta Bio Medica : Atenei Parmensis*, *89*(9), 141-146.

Cardozo, A. K., Buchillier, V., Mathieu, M., Chen, J., Ortis, F., Ladrière, L., Allaman-Pillet, N., Poirot, O., Kellenberger, S., Beckmann, J. S., Eizirik, D. L., Bonny, C., & Maurer, F. (2007). Cell-Permeable Peptides Induce Dose- And Length-Dependent Cytotoxic Effects. *Biochimica Et Biophysica Acta (Bba) - Biomembranes*, *1768*(9), 2222–2234.

Casey, G., Yamanaka, Y., Friess, H., Kobrin, M. S., Lopez, M. E., Buchler, M., Beger, H. G., & Korc, M. (1993). P53 Mutations Are Common In Pancreatic Cancer And Are Absent In Chronic Pancreatitis. *Cancer Letters*, *69*(3), 151–160.

Chen, J. (2016). The Cell-Cycle Arrest And Apoptotic Functions Of P53 In Tumor Initiation And Progression. *Cold Spring Harbor Perspectives In Medicine*, *6*(3), 1-16.

Chen, Z., Fillmore, C. M., Hammerman, P. S., Kim, C. F., & Wong, K. K. (2014). Non-Small-Cell Lung Cancers: A Heterogeneous Set Of Diseases. *Nature Reviews Cancer*, *14*(8), 535–546.

Chiang, Y. T., Chien, Y. C., Lin, Y. H., Wu, H. H., Lee, D. F., & Yu, Y. L. (2021). The Function Of The Mutant P53-R175h In Cancer. *Cancers, 13*(16), 4088.

Choi, S., Chen, M., Cryns, V. L., & Anderson, R. A. (2019). A Nuclear Phosphoinositide Kinase Complex Regulates P53. *Nature Cell Biology*, *21*(4), 462.

Chomet, M., Van Dongen, G. A. M. S., & Vugts, D. J. (2021). *State Of The Art In Radiolabelling Of Antibodies With Common And Uncommon Radiometals For Preclinical And Clinical Immuno-Pet*, 32, 1315-1330.

Choosing An Isotype Control Antibody | Abcam. (N.D.). Retrieved January 27, 2023, From Https://Www.Abcam.Com/Primary-Antibodies/Your-Guide-To-Selecting-An-Isotype-Control.

Cicenas, J., Kvederaviciute, K., Meskinyte, I., Meskinyte-Kausiliene, E., & Skeberdyte, A. (2017). Kras, Tp53, Cdkn2a, Smad4, Brca1, And Brca2 Mutations In Pancreatic Cancer. *Cancers*, *9*(5), 42.

Connor, A. A., & Gallinger, S. (2021). Pancreatic Cancer Evolution And Heterogeneity: Integrating Omics And Clinical Data. *Nature Reviews Cancer*, *22*(3), 131–142.

Cornelissen, B., Able, S., Kartsonaki, C., Kersemans, V., Allen, P. D., Cavallo, F., Cazier, J. B., Iezzi, M., Knight, J., Muschel, R., Smart, S., & Vallis, K. A. (2014). Imaging Dna Damage Allows Detection Of Preneoplasia In The Balb-Neut Model Of Breast Cancer. *Journal Of Nuclear Medicine*, *55*(12), 2026–2031.

Cornelissen, B., Darbar, S., Kersemans, V., Allen, D., Falzone, N., Barbeau, J., Smart, S., & Vallis, K. A. (2012). Amplification Of Dna Damage By A Γh2ax-Targeted Radiopharmaceutical. *Nuclear Medicine And Biology*, *39*(8), 1142–1151.

Cornelissen, B., Hu, M., Mclarty, K., Costantini, D., & Reilly, R. M. (2007). Cellular Penetration And Nuclear Importation Properties Of 111in-Labeled And 123i-Labeled Hiv-1 Tat Peptide Immunoconjugates In Bt-474 Human Breast Cancer Cells. *Nuclear Medicine And Biology*, *34*(1), 37–46.

Cornelissen, B., Kersemans, V., Darbar, S., Thompson, J., Shah, K., Sleeth, K., Hill, M. A., & Vallis, K. A. (2011). Imaging Dna Damage *In Vivo* Using Γh2ax-Targeted Immunoconjugates. *Cancer Research*, *71*(13), 4539–4549.

Criscitiello, C., Morganti, S., & Curigliano, G. (2021). Antibody–Drug Conjugates In Solid Tumors: A Look Into Novel Targets. *Journal Of Hematology & Oncology*, *14*(1), 1–18.

Dai, Z., Zhang, X. N., Nasertorabi, F., Cheng, Q., Li, J., Katz, B. B., Smbatyan, G., Pei, H., Louie, S. G., Lenz, H. J., Stevens, R. C., Zhang, Y., Zhang, Y., Zhang, Y., & Zhang, Y. (2020). Synthesis Of Site-Specific Antibody-Drug Conjugates By Adp-Ribosyl Cyclases. *Science Advances*, *6*(23).

Dammes, N., & Peer, D. (2020a). Monoclonal Antibody-Based Molecular Imaging Strategies And Theranostic Opportunities. *Theranostics*, *10*(2), 938.

Delidakis, G., Kim, J. E., George, K., & Georgiou, G. (2022). Improving Antibody Therapeutics By Manipulating The Fc Domain: Immunological And Structural Considerations. *Annurev-Bioeng*, *24*, 249–274.

Dennler, P., Fischer, E., & Schibli, R. (2015). Antibody Conjugates: From Heterogeneous Populations To Defined Reagents. *Antibodies, 4*(3), 197–224.

Derakhshankhah, H., & Jafari, S. (2018). Cell Penetrating Peptides: A Concise Review With Emphasis On Biomedical Applications. *Biomedicine & Pharmacotherapy*, *108*, 1090–1096.

Diao, L., & Meibohm, B. (2013). Pharmacokinetics And Pharmacokinetic–Pharmacodynamic Correlations Of Therapeutic Peptides. *Clinical Pharmacokinetics*, *52*(10), 855–868.

Dijkers, E. C. F., Kosterink, J. G. W., Rademaker, A. P., Perk, L. R., Van Dongen, G. A. M. S., Bart, J., De Jong, J. R., De Vries, E. G. E., & Lub-De Hooge, M. N. (2009). Development And Characterization Of Clinical-Grade 89zr-Trastuzumab For Her2/Neu Immunopet Imaging. *Journal Of Nuclear Medicine*, *50*(6), 974–981.

Du, X. H., Wei, H., Zhang, P., Yao, W. T., & Cai, Q. Q. (2020). Heterogeneity Of Soft Tissue Sarcomas And Its Implications In Targeted Therapy. *Frontiers In Oncology*, *10*.

Ducharme, M., Houson, H. A., Fernandez, S. R., & Lapi, S. E. (2022). Evaluation Of 68ga-Radiolabeled Peptides For Her2 Pet Imaging. *Diagnostics*, *12*(11), 2710.

Ducharme, M., & Lapi, S. E. (2020). Peptide Based Imaging Agents For Her2 Imaging In Oncology. *Molecular Imaging*, *19*.

E. Poruk, K., Z. Gay, D., Brown, K., D. Mulvihill, J., M. Boucher, K., L. Scaife, C., A. Firpo, M., & J. Mulvihill, S. (2013). The Clinical Utility Of Ca 19-9 In Pancreatic Adenocarcinoma: Diagnostic And Prognostic Updates. *Current Molecular Medicine*, *13*(3), 340–351.

Engeland, K. (2017). Cell Cycle Arrest Through Indirect Transcriptional Repression By P53: I Have A Dream. *Cell Death & Differentiation*, *25*(1), 114–132.

Evans, B. J., King, A. T., Katsifis, A., Matesic, L., & Jamie, J. F. (2020). Methods To Enhance The Metabolic Stability Of Peptide-Based Pet Radiopharmaceuticals. *Molecules*, *25*(10), 2014.

Even, A. J. G., Hamming-Vrieze, O., Van Elmpt, W., Winnepenninckx, V. J. L., Heukelom, J., Tesselaar, M. E. T., Vogel, W. V., Hoeben, A., Zegers, C. M. L., Vugts, D. J., Van Dongen, G. A. M. S., Bartelink, H., Mottaghy, F. M., Hoebers, F., & Lambin, P. (2017). Quantitative Assessment Of Zirconium-89 Labeled Cetuximab Using Pet/Ct Imaging In Patients With Advanced Head And Neck Cancer: A Theragnostic Approach. *Oncotarget*, *8*(3), 3870.

Fani, M., Maecke, H. R., & Okarvi, S. M. (2012a). Radiolabeled Peptides: Valuable Tools For The Detection And Treatment Of Cancer. *Theranostics*, *2*(5), 481–501.

Fiorini, C., Cordani, M., Padroni, C., Blandino, G., Di Agostino, S., & Donadelli, M. (2015). Mutant P53 Stimulates Chemoresistance Of Pancreatic Adenocarcinoma Cells To Gemcitabine. *Biochimica Et Biophysica Acta (Bba) - Molecular Cell Research*, *1853*(1), 89–100.

Freed-Pastor, W. A., & Prives, C. (2012). Mutant p53: one name, many proteins. *Genes & Development*, *26*(12), 1268.

Freitas, N., & Cunha, C. (2009). Mechanisms And Signals For The Nuclear Import Of Proteins. *Current Genomics*, *10*(8), 550.

Frejd, F. Y., & Kim, K. T. (2017). Affibody Molecules As Engineered Protein Drugs. *Experimental & Molecular Medicine*, *49*(3), E306–E306.

Fu, Z., Li, S., Han, S., Shi, C., & Zhang, Y. (2022). Antibody Drug Conjugate: The "Biological Missile" For Targeted Cancer Therapy. *Signal Transduction And Targeted Therapy*, *7*(1), 1–25.

Futaki, S., Nakase, I., Tadokoro, A., Takeuchi, T., & Jones, A. T. (2007). Arginine-Rich Peptides And Their Internalization Mechanisms. *Biochemical Society Transactions*, *35*(4), 784–787.

Haeberle, L., & Esposito, I. (2019). Pathology Of Pancreatic Cancer. *Translational Gastroenterology And Hepatology*, *4*(50), 1¬12.

Hallin, J., Bowcut, V., Calinisan, A., Briere, D. M., Hargis, L., Engstrom, L. D., Laguer, J., Medwid, J., Vanderpool, D., Lifset, E., Trinh, D., Hoffman, N., Wang, X., David Lawson, J., Gunn, R. J., Smith, C. R., Thomas, N. C., Martinson, M., Bergstrom, A., … Christensen, J. G. (2022). Anti-tumor efficacy of a potent and selective non-covalent KRASG12D inhibitor. *Nature Medicine 2022 28:10*, *28*(10), 2171–2182.

Hanyu, A., Kojima, K., Hatake, K., Nomura, K., Murayama, H., Ishikawa, Y., Miyata, S., Ushijima, M., Matsuura, M., Ogata, E., Miyazawa, K., & Imamura, T. (2009). Functional *In Vivo* Optical Imaging Of Tumor Angiogenesis, Growth, And Metastasis Prevented By Administration Of Anti-Human Vegf Antibody In Xenograft Model Of Human Fibrosarcoma Ht1080 Cells. *Cancer Science*, *100*(11), 2085–2092.

Harris, S. L., & Levine, A. J. (2005). The P53 Pathway: Positive And Negative Feedback Loops. *Oncogene*, *24*(17), 2899–2908.

Hassin, O., Nataraj, N. B., Shreberk-Shaked, M., Aylon, Y., Yaeger, R., Fontemaggi, G., Mukherjee, S., Maddalena, M., Avioz, A., Iancu, O., Mallel, G., Gershoni, A., Grosheva, I., Feldmesser, E., Ben-Dor, S., Golani, O., Hendel, A., Blandino, G., Kelsen, D., … Oren, M. (2022). Different Hotspot P53 Mutants Exert Distinct Phenotypes And Predict Outcome Of Colorectal Cancer Patients. *Nature Communications*, *13*(1), 1–15.

Haugland, R. P. (1995). Coupling Of Monoclonal Antibodies With Fluorophores. *Methods In Molecular Biology (Clifton, N.J.)*, *45*, 205–221.

Hezel, A. F., Kimmelman, A. C., Stanger, B. Z., Bardeesy, N., & Depinho, R. A. (2006). *Genetics And Biology Of Pancreatic Ductal Adenocarcinoma*, 20, 1218-1249.

Hingorani, S. R., Zheng, L., Bullock, A. J., Seery, T. E., Harris, W. P., Sigal, D. S., Braiteh, F., Ritch, P. S., Zalupski, M. M., Bahary, N., Oberstein, P. E., Wang-Gillam, A., Wu, W., Chondros, D., Jiang, P., Khelifa, S., Pu, J., Aldrich, C., & Hendifar, A. E. (2018). HALO 202: Randomized phase II Study of PEGPH20 Plus Nab-Paclitaxel/Gemcitabine Versus Nab-Paclitaxel/Gemcitabine in Patients With Untreated, Metastatic Pancreatic Ductal Adenocarcinoma. *Journal of Clinical Oncology*, *36*(4), 359–366.

Hong, E., Park, S., Ooshima, A., Hong, C. P., Park, J., Heo, J. S., Lee, S., An, H., Kang, J. M., Park, S. H., Park, J. O., & Kim, S. J. (2020). Inhibition of TGF-β signalling in combination with nal-IRI plus 5-Fluorouracil/Leucovorin suppresses invasion and prolongs survival in pancreatic tumour mouse models. *Scientific Reports 2020 10:1*, *10*(1), 1–12.

Horvat, N., Ryan, D. E., Lagratta, M. D., Shah, P. M., & Do, R. K. (2018). Imaging For Pancreatic Ductal Adenocarcinoma. *Chinese Clinical Oncology*, *6*(6), 6–6.

Hruban, R. H., Maitra, A., & Goggins, M. (2008). Update On Pancreatic Intraepithelial Neoplasia. *International Journal Of Clinical And Experimental Pathology*, *1*(4), 306.

Hu, J., Cao, J., Topatana, W., Juengpanich, S., Li, S., Zhang, B., Shen, J., Cai, L., Cai, X., & Chen, M. (2021). Targeting mutant p53 for cancer therapy: direct and indirect strategies. *Journal of Hematology & Oncology 2021 14:1*, *14*(1), 1–19.

Hu, J. X., Lin, Y. Y., Zhao, C. F., Chen, W. B., Liu, Q. C., Li, Q. W., & Gao, F. (2021). Pancreatic Cancer: A Review Of Epidemiology, Trend, And Risk Factors. *World Journal Of Gastroenterology*, *27*(27), 4298.

Huang, Y., Jiang, K., Zhang, X., & Chung, E. J. (2020). The Effect Of Size, Charge, And Peptide Ligand Length On Kidney Targeting By Small, Organic Nanoparticles. *Bioengineering & Translational Medicine*, *5*(3), 1¬11.

Inoue, K., Kurabayashi, A., Shuin, T., Ohtsuki, Y., & Furihata, M. (2012). Overexpression Of P53 Protein In Human Tumors. *Medical Molecular Morphology*, *45*(3), 115–123.

Jain, A. K., & Barton, M. C. (2018). P53: Emerging Roles In Stem Cells, Development And Beyond. *Development (Cambridge)*, *145*(8).

Jain, N., Smith, S. W., Ghone, S., & Tomczuk, B. (2015). Current Adc Linker Chemistry. *Pharmaceutical Research*, *32*(11), 3526.

James, M. L., & Gambhir, S. S. (2012). A Molecular Imaging Primer: Modalities, Imaging Agents, And Applications. *Physiological Reviews*, *92*(2), 897–965.

Jiang, B., Zhou, L., Lu, J., Wang, Y., Liu, C., You, L., & Guo, J. (2020). Stroma-Targeting Therapy In Pancreatic Cancer: One Coin With Two Sides? *Frontiers In Oncology*, *10,* 1-9.

Joerger, A. C., & Fersht, A. R. (2007). Structure–Function–Rescue: The Diverse Nature Of Common P53 Cancer Mutants. *Oncogene*, *26*(15), 2226–2242.

Joerger, A. C., & Fersht, A. R. (2008). Structural Biology Of The Tumor Suppressor P53. *Annurev.Biochem*, *77*, 557–582.

Joerger, A. C., & Fersht, A. R. (2010). The Tumor Suppressor P53: From Structures To Drug Discovery. *Cold Spring Harbor Perspectives In Biology*, *2*(6), 1-21.

Joerger, A. C., & Fersht, A. R. (2016). *The P53 Pathway: Origins, Inactivation In Cancer, And Emerging Therapeutic Approaches*, 85, 375–404.

Junutula, J. R., Flagella, K. M., Graham, R. A., Parsons, K. L., Ha, E., Raab, H., Bhakta, S., Nguyen, T., Dugger, D. L., Li, G., Mai, E., Phillips, G. D. L., Hiraragi, H., Fuji, R. N., Tibbitts, J., Vandlen, R., Spencer, S. D., Scheller, R. H., Polakis, P., & Sliwkowski, M. X. (2010). Engineered Thio-Trastuzumab-Dm1 Conjugate With An Improved Therapeutic Index To Target Human Epidermal Growth Factor Receptor 2-Positive Breast Cancer. *Clinical Cancer Research*, *16*(19), 4769–4778.

Junutula, J. R., Raab, H., Clark, S., Bhakta, S., Leipold, D. D., Weir, S., Chen, Y., Simpson, M., Tsai, S. P., Dennis, M. S., Lu, Y., Meng, Y. G., Ng, C., Yang, J., Lee, C. C., Duenas, E., Gorrell, J., Katta, V., Kim, A., … Mallet, W. (2008). Site-Specific Conjugation Of A Cytotoxic Drug To An Antibody Improves The Therapeutic Index. *Nature Biotechnology*, *26*(8), 925–932.

Kano, M. R., Bae, Y., Iwata, C., Morishita, Y., Yashiro, M., Oka, M., Fujii, T., Komuro, A., Kiyono, K., Kaminishi, M., Hirakawa, K., Ouchi, Y., Nishiyama, N., Kataoka, K., & Miyazono, K. (2007). Improvement Of Cancer-Targeting Therapy, Using Nanocarriers For Intractable Solid Tumors By Inhibition Of Tgf-B Signaling. *Proceedings Of The National Academy Of Sciences Of The United States Of America*, *104*(9), 3460–3465.

Kaplan, I. M., Wadia, J. S., & Dowdy, S. F. (2005). Cationic Tat Peptide Transduction Domain Enters Cells By Macropinocytosis. *Journal Of Controlled Release*, *102*(1), 247–253.

Kato, S., Han, S. Y., Liu, W., Otsuka, K., Shibata, H., Kanamaru, R., & Ishioka, C. (2003). Understanding The Function-Structure And Function-Mutation Relationships Of P53 Tumor Suppressor Protein By High-Resolution Missense Mutation Analysis. *Proceedings Of The National Academy Of Sciences Of The United States Of America*, *100*(14), 8424–8429.

Khalil, M. M., Tremoleda, J. L., Bayomy, T. B., & Gsell, W. (2011). Molecular Spect Imaging: An Overview. *International Journal Of Molecular Imaging*, *2011*, 1–15.

Kholodenko, R. V., Kalinovsky, D. V., Doronin, I. I., Ponomarev, E. D., & Kholodenko, I. V. (2019). Antibody Fragments As Potential Biopharmaceuticals For Cancer Therapy: Success And Limitations. *Current Medicinal Chemistry*, *26*(3), 396–426.

Khorana, H. G. (1953). The Chemistry Of Carbodiimides. *Chemical Reviews*, *53*(2), 145–166.

Kikuchi, M., Clump, D. A., Srivastava, R. M., Sun, L., Zeng, D., Diaz-Perez, J. A., Anderson, C. J., Edwards, W. B., & Ferris, R. L. (2017). Preclinical Immunopet/Ct Imaging Using Zr-89-Labeled Anti-Pd-L1 Monoclonal Antibody For Assessing Radiation-Induced Pd-L1 Upregulation In Head And Neck Cancer And Melanoma. *Oncoimmunology*, *6*(7), E1329071.

Kim, J. Y., & Hong, S. M. (2018). Precursor Lesions Of Pancreatic Cancer. *Oncology Research And Treatment*, *41*(10), 603–610.

Kim, M. H., Kim, S. G., & Kim, D. W. (2022). A Novel Dual-Labeled Small Peptide As A Multimodal Imaging Agent For Targeting Wild-Type Egfr In Tumors. *Plos One*, *17*(2), E0263474.

Klein, A. (2019). Pancreatic Cancer: A Growing Burden. *Lancet Gastroenterol. Hepatol.*, *4*, 895–896.

Knight, J. C., Bagu~ Na Torres, J., Goldin, R., Mosley, M., Dias, G. M., Contreras Bravo, L., Kersemans, V., Allen, P. D., Mukherjee, S., Smart, S., & Cornelissen, B. (2020). *Early Detection In A Mouse Model Of Pancreatic Cancer By Imaging Dna Damage Response Signaling*, 62(7), 1006-1013.

Knight, J. C., Koustoulidou, S., & Cornelissen, B. (2017). Imaging The Dna Damage Response With Pet And Spect. *European Journal Of Nuclear Medicine And Molecular Imaging*, *44*(6), 1065-1078.

Knight, J. C., Topping, C., Mosley, M., Kersemans, V., Falzone, N., Fernández-Varea, J. M., & Cornelissen, B. (2015). Pet Imaging Of Dna Damage Using 89zr-Labelled Anti-Γh2ax-Tat Immunoconjugates. *European Journal Of Nuclear Medicine And Molecular Imaging*, *42*(11), 1707–1717.

Knowles, S. M., Tavaré, R., Zettlitz, K. A., Rochefort, M. M., Salazar, F. B., Jiang, Z. K., Reiter, R. E., & Wu, A. M. (2014). Applications Of Immunopet: Using124i-Anti-Psca A11 Minibody For Imaging Disease Progression And Response To Therapy In Mouse Xenograft Models Of Prostate Cancer. *Clinical Cancer Research*, *20*(24), 6367–6378.

Köhler, G., & Milstein, C. (1975). Continuous Cultures Of Fused Cells Secreting Antibody Of Predefined Specificity. *Nature*, *256*(5517), 495–497.

Koorstra, J. B. M., Hong, S. M., Shi, C., Meeker, A. K., Ryu, J. K., Offerhaus, G. J. A., Goggins, M. G., Hruban, R. H., & Maitra, A. (2009a). Widespread Activation Of The Dna Damage Response In Human Pancreatic Intraepithelial Neoplasia. *Modern Pathology : An Official Journal Of The United States And Canadian Academy Of Pathology, Inc*, *22*(11), 1439.

Koren, E., Apte, A., Sawant, R. R., Grunwald, J., & Torchilin, V. P. (2011). Cell-Penetrating Tat Peptide In Drug Delivery Systems: Proteolytic Stability Requirements. *Drug Delivery*, *18*(5), 377.

Lee, J. W., Komar, C. A., Bengsch, F., Graham, K., & Beatty, G. L. (2016). Genetically Engineered Mouse Models Of Pancreatic Cancer: The Kpc Model (Lsl-Krasg12d/+;Lsl-Trp53r172h/+;Pdx-1-Cre), Its Variants And Their Application In Immuno-Oncology Drug Discovery. *Current Protocols In Pharmacology / Editorial Board, S.J. Enna (Editor-In-Chief) ... [Et Al.]*, *73*(1),14.39.1 - 14.39.20.

Levine, A. J., & Oren, M. (2009). The First 30 Years Of P53: Growing Ever More Complex. *Nature Reviews. Cancer*, *9*(10), 749.

Lewis, E. J., & Taylor, E. (2015). Prima-1 As A Cancer Therapy Restoring Mutant P53: A Review. *Bioscience Horizons: The International Journal Of Student Research*, *8*, 1-5.

Li, H., Zhang, J., Tong, J. H. M., Chan, A. W. H., Yu, J., Kang, W., & To, K. F. (2019). Targeting The Oncogenic P53 Mutants In Colorectal Cancer And Other Solid Tumors. *International Journal Of Molecular Sciences*, *20*(23), 5999.

Li, X., Cai, H., Wu, X., Li, L., Wu, H., & Tian, R. (2020). New Frontiers In Molecular Imaging Using Peptide-Based Radiopharmaceuticals For Prostate Cancer. *Frontiers In Chemistry*, *8*, 1106.

Linzer, D. I. H., & Levine, A. J. (1979). Characterization Of A 54k Dalton Cellular Sv40 Tumor Antigen Present In Sv40-Transformed Cells And Uninfected Embryonal Carcinoma Cells. *Cell*, *17*(1), 43–52.

Liu, D., & Xu, Y. (2011). P53, Oxidative Stress, And Aging. *Antioxidants & Redox Signaling*, *15*(6), 1669.

Longmire, M., Choyke, P. L., & Kobayashi, H. (2008). Clearance Properties Of Nano-Sized Particles And Molecules As Imaging Agents: Considerations And Caveats. *Nanomedicine (London, England)*, *3*(5), 703.

Lu, R. M., Hwang, Y. C., Liu, I. J., Lee, C. C., Tsai, H. Z., Li, H. J., & Wu, H. C. (2020). Development of therapeutic antibodies for the treatment of diseases. *Journal of Biomedical Science 2020 27:1*, *27*(1), 1–30.

Luo, Y., Pan, Q., Yang, H., Peng, L., Zhang, W., & Li, F. (2021). Fibroblast Activation Protein-Targeted PET/CT with 68Ga-FAPI for Imaging IgG4-Related Disease: Comparison to 18F-FDG PET/CT.

Journal of Nuclear Medicine : Official Publication, Society of Nuclear Medicine, *62*(2), 266–271.

Machado, N. O., Al Qadhi, H., & Al Wahibi, K. (2015). Intraductal Papillary Mucinous Neoplasm Of Pancreas. *North American Journal Of Medical Sciences*, *7*(5), 160.

Mantovani, F., Collavin, L., & Del Sal, G. (2018). Mutant p53 as a guardian of the cancer cell. *Cell Death & Differentiation 2018 26:2*, *26*(2), 199–212.

Marqus, S., Pirogova, E., & Piva, T. J. (2017). Evaluation Of The Use Of Therapeutic Peptides For Cancer Treatment. *Journal Of Biomedical Science*, *24*(1), 1–15.

Marrelli, D., Caruso, S., Pedrazzani, C., Neri, A., Fernandes, E., Marini, M., Pinto, E., & Roviello, F. (2009). Ca19-9 Serum Levels In Obstructive Jaundice: Clinical Value In Benign And Malignant Conditions. *American Journal Of Surgery*, *198*(3), 333–339.

Mary, B. (2022). The Role P53 Protein In Dna Repair. *P53 - A Guardian Of The Genome And Beyond*.

Mccombs, J. R., & Owen, S. C. (2015). Antibody Drug Conjugates: Design And Selection Of Linker, Payload And Conjugation Chemistry. *The Aaps Journal*, *17*(2), 339.

Michalovitz, D., Halevy, O., & Oren, M. (1990). Conditional Inhibition Of Transformation And Of Cell Proliferation By A Temperature-Sensitive Mutant Of P53. *Cell*, *62*(4), 671–680.

Milletti, F. (2012). Cell-Penetrating Peptides: Classes, Origin, And Current Landscape. *Drug Discovery Today*, *17*(15–16), 850–860.

Mishra, A., Lai, G. H., Schmidt, N. W., Sun, V. Z., Rodriguez, A. R., Tong, R., Tang, L., Cheng, J., Deming, T. J., Kamei, D. T., & Wong, G. C. L. (2011). Translocation Of Hiv Tat Peptide And

Analogues Induced By Multiplexed Membrane And Cytoskeletal Interactions. *Proceedings Of The National Academy Of Sciences Of The United States Of America*, *108*(41), 16883–16888.

Mitra, S., & Tomar, P. C. (2021). Hybridoma Technology; Advancements, Clinical Significance, And Future Aspects. *Journal Of Genetic Engineering & Biotechnology*, *19*(1), 159.

Moradi, F., & Iagaru, A. (2020). Will FAPI PET/CT Replace FDG PET/CT in the Next Decade? Counterpoint—No, Not So Fast! *Https://Doi.Org/10.2214/AJR.20.23794*, *216*(2), 307–308.

Mori, Y., Dendl, K., Cardinale, J., Kratochwil, C., Giesel, F. L., & Haberkorn, U. (2023). FAPI PET: Fibroblast Activation Protein Inhibitor Use in Oncologic and Nononcologic Disease. Radiology, 306(2), 1–14.

Morton, J. P., Timpson, P., Karim, S. A., Ridgway, R. A., Athineos, D., Doyle, B., Jamieson, N. B., Oien, K. A., Lowy, A. M., Brunton, V. G., Frame, M. C., Evans, T. R. J., & Sansom, O. J. (2010). Mutant P53 Drives Metastasis And Overcomes Growth Arrest/Senescence In Pancreatic Cancer. *Proceedings Of The National Academy Of Sciences Of The United States Of America*, *107*(1), 246–251.

Muller, P. A. J., & Vousden, K. H. (2014). Mutant P53 In Cancer: New Functions And Therapeutic Opportunities. *Cancer Cell*, *25*(3), 304–317.

N. Kalimuthu, S., & Notta, F. (2016). Molecular Pathogenesis Of Pancreatic Ductal Adenocarcinoma. *Diagnostic Histopathology*, *22*(6), 226–235.

Nagaraju, G. P., & Ahmad, S. (2019). *Theranostic Approach For Pancreatic Cancer*.

Naik, M., Al-Nahhas, A., & Khan, S. R. (2022). Treatment Of Neuroendocrine Neoplasms With Radiolabeled Peptides—Where Are We Now. In *Cancers*, 14(3), 1-24.

Nygren, P. Å. (2008). Alternative Binding Proteins: Affibody Binding Proteins Developed From A Small Three-Helix Bundle Scaffold. *Febs Journal*, *275*(11), 2668–2676.

Oni, T. E., Bautista, C., Merrill, J. R., Goos, J. A. C. M., Rivera, K. D., Miyabayashi, K., Biffi, G., Garcia, L., Plenker, D., Patel, H., Elyada, E., Samaritano, M., Yu, K. H., Pappin, D. J., Goggins, M. G., Hruban, R. H., Lewis, J. S., Lyons, S. K., Yeh, J. T., & Tuveson, D. A. (2020). Detection of incipient pancreatic cancer with novel tumor-specific antibodies in mouse models. BioRxiv, 1–17.

Orth, M., Metzger, P., Gerum, S., Mayerle, J., Schneider, G., Belka, C., Schnurr, M., & Lauber, K. (2019). Pancreatic Ductal Adenocarcinoma: Biological Hallmarks, Current Status, And Future Perspectives Of Combined Modality Treatment Approaches. *Radiation Oncology*, *14*(1), 1–20.

Otowa, Y., Kishimoto, S., Saida, Y., Yamashita, K., Yamamoto, K., Chandramouli, G. V., Devasahayam, N., Mitchell, J. B., Krishna, M. C., & Brender, J. R. (2022). Evofosfamide And Gemcitabine Act Synergistically In Pancreatic Cancer Xenografts By Dual Action On Tumor Vasculature And Inhibition Of Homologous Recombination Dna Repair. *Biorxiv*, 2022.07.04.498761.

P53 antibody (10442-1-AP) | Proteintech. (n.d.). Retrieved June 2, 2023, from https://www.ptglab.com/products/P53-Antibody-10442-1-AP.htm.

Palm-Apergi, C., Lönn, P., & Dowdy, S. F. (2012). Do Cell-Penetrating Peptides Actually "Penetrate" Cellular Membranes? *Molecular Therapy*, *20*(4), 695–697.

Pandey, R., Zhou, M., Islam, S., Chen, B., Barker, N. K., Langlais, P., Srivastava, A., Luo, M., Cooke, L. S., Weterings, E., & Mahadevan, D. (2019). Carcinoembryonic antigen cell adhesion molecule 6 (CEACAM6) in Pancreatic Ductal Adenocarcinoma (PDA): An integrative analysis of a novel therapeutic target. Scientific Reports 2019 9:1, 9(1), 1–14.

Panowski, S., Bhakta, S., Raab, H., Polakis, P., & Junutula, J. R. (2013). Site-Specific Antibody Drug Conjugates For Cancer Therapy. *Mabs*, *6*(1), 34–45.

Parakh, S., Lee, S. T., Gan, H. K., & Scott, A. M. (2022). Radiolabelled Antibodies For Cancer Imaging And Therapy. *Cancers*, *14*(6), 1454.

Patel, S. G., Sayers, E. J., He, L., Narayan, R., Williams, T. L., Mills, E. M., Allemann, R. K., Luk, L. Y. P., Jones, A. T., & Tsai, Y. H. (2019). Cell-Penetrating Peptide Sequence And Modification Dependent Uptake And Subcellular Distribution Of Green Florescent Protein In Different Cell Lines. *Scientific Reports*, *9*(1), 1–9.

Perik, P. J., Lub-De Hooge, M. N., Gietema, J. A., Van Der Graaf, W. T. A., De Korte, M. A., Jonkman, S., Kosterink, J. G. W., Van Veldhuisen, D. J., Sleijfer, D. T., Jager, P. L., & De Vries, E. G. E. (2006). Indium-111-Labeled Trastuzumab Scintigraphy In Patients With Human Epidermal Growth Factor Receptor 2-Positive Metastatic Breast Cancer. *Journal Of Clinical Oncology*, *24*(15), 2276–2282.

Permuth-Wey, J., & Egan, K. M. (2008). Family History Is A Significant Risk Factor For Pancreatic Cancer: Results From A Systematic Review And Meta-Analysis. *Familial Cancer*, *8*(2), 109–117.

Perri, F., Pisconti, S., & Vittoria Scarpati, G. Della. (2016). P53 Mutations And Cancer: A Tight Linkage. *Annals Of Translational Medicine*, *4*(24), 1-4.

Peters, M. L. B., Eckel, A., Mueller, P. P., Tramontano, A. C., Weaver, D. T., Lietz, A., Hur, C., Kong, C. Y., & Pandharipande, P. V. (2018). Progression To Pancreatic Ductal Adenocarcinoma From Pancreatic Intraepithelial Neoplasia: Results Of A Simulation Model. *Pancreatology : Official Journal Of The International Association Of Pancreatology (Iap) ... [Et Al.]*, *18*(8), 928.

Peters, M. L. B., Tseng, J. F., & Miksad, R. A. (2016). Genetic Testing In Pancreatic Ductal Adenocarcinoma: Implications For Prevention And Treatment. *Clinical Therapeutics*, *38*(7), 1622–1635.

Poeppel, T. D., Binse, I., Petersenn, S., Lahner, H., Schott, M., Antoch, G., Brandau, W., Bockisch, A., & Boy, C. (2011). 68 Ga-Dotatoc Versus 68 Ga-Dotatate Pet/Ct In Functional Imaging Of Neuroendocrine Tumors. *J Nucl Med*, *52*, 1864–1870.

Polyakov, V., Sharma, V., Dahlheimer, J. L., Pica, C. M., Luker, G. D., & Piwnica-Worms, D. (2000). Novel Tat-Peptide Chelates For Direct Transduction Of Technetium-99m And Rhenium Into Human Cells For Imaging And Radiotherapy. *Bioconjugate Chemistry*, *11*(6), 762–771.

Pysz, M. A., Gambhir, S. S., & Willmann, J. K. (2010). Molecular Imaging: Current Status And Emerging Strategies. *Clinical Radiology*, *65*(7), 500–516.

Pyzik, M., Rath, T., Lencer, W. I., Baker, K., & Blumberg, R. S. (2015). Fcrn: The Architect Behind The Immune And Non-Immune Functions Of Igg And Albumin. *Journal Of Immunology (Baltimore, Md. : 1950)*, *194*(10), 4595.

Qian, Z., Martyna, A., Hard, R. L., Wang, J., Appiah-Kubi, G., Coss, C., Phelps, M. A., Rossman, J. S., & Pei, D. (2016). Discovery And Mechanism Of Highly Efficient Cyclic Cell-Penetrating Peptides. *Biochemistry*, *55*(18), 2601.

R€ Ohrich, M., Naumann, P., Giesel, F. L., Choyke, P. L., Staudinger, F., Wefers, A., Liew, D. P., Kratochwil, C., Rathke, H., Liermann, J., Herfarth, K., J€ Ager, D., Urgen Debus, J., Haberkorn, U., Lang, M., & Koerber, S. A. (2021). Impact of 68Ga-FAPI PET/CT Imaging on the Therapeutic Management of Primary and Recurrent Pancreatic Ductal Adenocarcinomas. Journal of Nuclear Medicine, 62(6), 779–786.

Rath, T., Baker, K., Dumont, J. A., Peters, R. T., Jiang, H., Qiao, S. W., Lencer, W. I., Pierce, G. F., & Blumberg, R. S. (2015). Fc-Fusion Proteins And Fcrn: Structural Insights For Longer-Lasting And More Effective Therapeutics. *Critical Reviews In Biotechnology*, *35*(2), 235–254.

Ratnayake, B., Savastyuk, A. Y., Nayar, M., Wilson, C. H., Windsor, J. A., Roberts, K., French, J. J., & Pandanaboyana, S. (2020). Recurrence Patterns For Pancreatic Ductal Adenocarcinoma After Upfront Resection Versus Resection Following Neoadjuvant Therapy: A Comprehensive Meta-Analysis. *Journal Of Clinical Medicine*, *9*(7), 1–19.

Rawla, P., Sunkara, T., & Gaduputi, V. (2019). Epidemiology of Pancreatic Cancer: Global Trends, Etiology and Risk Factors. *World Journal of Oncology*, *10*(1), 10.

Rehman, Z. U., Hoekstra, D., & Zuhorn, I. S. (2013). Mechanism Of Polyplex- And Lipoplex-Mediated Delivery Of Nucleic Acids: Real-Time Visualization Of Transient Membrane Destabilization Without Endosomal Lysis. *Acs Nano*, *7*(5), 3767–3777.

Riley, T., Sontag, E., Chen, P., & Levine, A. (2008b). Transcriptional Control Of Human P53-Regulated Genes. *Nature Reviews Molecular Cell Biology*, *9*(5), 402–412.

Rizzuti, M., Nizzardo, M., Zanetta, C., Ramirez, A., & Corti, S. (2015). Therapeutic Applications Of The Cell-Penetrating Hiv-1 Tat Peptide. *Drug Discovery Today*, *20*(1), 76–85.

Rodrigo, G., Gruvegård, M., & Van Alstine, J. M. (2015). Antibody Fragments And Their Purification By Protein L Affinity Chromatography. *Antibodies*, *4*(3), 259–277.

Ruseska, I., & Zimmer, A. (2020). Internalization Mechanisms Of Cell-Penetrating Peptides. *Beilstein J. Nanotechnol*, 101–123.

Sahni, A., Qian, Z. & Pei, D. 2020. Cell-Penetrating Peptides Escape the Endosome by Inducing Vesicle Budding and Collapse. ACS Chem Biol, 15, 2485-2492.

Sayed, S. A. El, & Mukherjee, S. (2022). Physiology, Pancreas. *Statpearls*.

Scheck, R. A., & Francis, M. B. (2007). *Regioselective Labeling Of Antibodies Through N-Terminal Transamination*, 2(4), 247–251

Shi, J., Wang, F., & Liu, S. (2016). Radiolabeled Cyclic Rgd Peptides As Radiotracers For Tumor Imaging. *Biophysics Reports*, *2*(1), 1–20.

Singla, A. K., Downey, C. M., Bebb, G. D., & Jirik, F. R. (2015). Characterization Of A Murine Model Of Metastatic Human Non-Small Cell Lung Cancer And Effect Of Cxcr4 Inhibition On The Growth Of Metastases. *Oncoscience*, *2*(3), 263.

Slastnikova, T. A., Ulasov, A. V., Rosenkranz, A. A., & Sobolev, A. S. (2018). Targeted Intracellular Delivery Of Antibodies: The State Of The Art. *Frontiers In Pharmacology*, *9*(Oct), 1208.

Sonawane, N. D., Szoka, F. C., & Verkman, A. S. (2003). Chloride Accumulation And Swelling In Endosomes Enhances Dna Transfer By Polyamine-Dna Polyplexes. *Journal Of Biological Chemistry*, *278*(45), 44826–44831.

Soussi, T. (2010). The History Of P53: A Perfect Example Of The Drawbacks Of Scientific Paradigms. *Embo Reports*, *11*(11), 822-826.

Strobel, O., & Büchler, M. W. (2013). Fdg-Pet Is Not Useful In Early Pancreatic Cancer Diagnosis. *Nature Reviews Gastroenterology & Hepatology*, *10*(4), 203–205.

Subhan, M. A., Yalamarty, S. S. K., Filipczak, N., Parveen, F., & Torchilin, V. P. (2021). Recent Advances In Tumor Targeting Via Epr Effect For Cancer Treatment. *Journal Of Personalized Medicine, 11*(6), 1-27.

Sugrue, M. M., Shin, D. Y., Lee, S. W., & Aaronson, S. A. (1997). Wild-Type P53 Triggers A Rapid Senescence Program In Human Tumor Cells Lacking Functional P53. *Proceedings Of The National Academy Of Sciences Of The United States Of America*, 9648–9653.

Sun, X., Li, Y., Liu, T., Li, Z., Zhang, X., & Chen, X. (2017). Peptide-Based Imaging Agents For Cancer Detection. *Advanced Drug Delivery Reviews*, (*110–111)*, 38–51.

Tal, P., Eizenberger, S., Cohen, E., Goldfinger, N., Pietrokovski, S., Oren, M., & Rotter, V. (2016). *Cancer Therapeutic Approach Based On Conformational Stabilization Of Mutant P53 Protein By Small Peptides*. *7*(11) , 11817-11837.

Talar-Wojnarowska, R., Gasiorowska, A., Beata, S., Centrum, I., Polki, Z. M., & Romanowicz, H. (2006). Comparative Evaluation Of P53 Mutation In Pancreatic Adenocarcinoma And Chronic Pancreatitis. *Hepatogastroenterology,* 53(70), 608-612

Tang, Y., Tang, F., Yang, Y., Zhao, L., Zhou, H., Dong, J., & Huang, W. (2017). Real-Time Analysis On Drug-Antibody Ratio Of Antibody-Drug Conjugates For Synthesis, Process Optimization, And Quality Control. *Scientific Reports*, *7*(1), 1–10.

Taniguchi, Y., & Kawakami, M. (2012a). Variation In The Mechanical Unfolding Pathway Of P53dbd Induced By Interaction With P53 N-Terminal Region Or Dna. *Plos One*, *7*(11), 1-7.

Thompson, L. D. R., Becker, R. C., Przygodzki, R. M., Adair, C. F., & Heffess, C. S. (1999). Mucinous Cystic Neoplasm (Mucinous Cystadenocarcinoma Of Low-Grade Malignant Potential) Of The Pancreas: A Clinicopathologic Study Of 130 Cases. *The American Journal Of Surgical Pathology*, *23*(1), 1–16.

Tietz, O., Cortezon-Tamarit, F., Chalk, R., Able, S., & Vallis, K. A. (2022). Tricyclic cell-penetrating peptides for efficient delivery of functional antibodies into cancer cells. *Nature Chemistry 2021 14:3*, *14*(3), 284–293.

Tolmachev, V., & Orlova, A. (2020). Affibody Molecules As Targeting Vectors For Pet Imaging. *Cancers*, *12*(3), 1-21.

Torchilin, V. P. (2006). Recent Approaches To Intracellular Delivery Of Drugs And Dna And Organelle Targeting. *Annurev.Bioeng, 8*, 343–375.

Uhlen, M., Bandrowski, A., Carr, S., Edwards, A., Ellenberg, J., Lundberg, E., Rimm, D. L., Rodriguez, H., Hiltke, T., Snyder, M., & Yamamoto, T. (2016). A Proposal For Validation Of Antibodies. *Nature Methods*, *13*(10), 823–827.

Urquhart, L. (2020). Top Companies And Drugs By Sales In 2019. *Nature Reviews. Drug Discovery*, *19*(4), 228.

Veal, M., Dias, G., Kersemans, V., Sneddon, D., Faulkner, S., & Cornelissen, B. (2021). A Model System To Explore The Detection Limits Of Antibody-Based Immuno-Spect Imaging Of Exclusively Intranuclear Epitopes. *Journal Of Nuclear Medicine*, *62*(11), 1537–1544.

Vivier, D., Sharma, S. K., Adumeau, P., Rodriguez, C., Fung, K., & Zeglis, B. M. (2019). The Impact Of Fcγri Binding On Immuno-Pet. *Journal Of Nuclear Medicine*, *60*(8), 1174-1182.

Vogiatzi, F., Brandt, D. T., Schneikert, J., Fuchs, J., Grikscheit, K., Wanzel, M., Pavlakis, E., Charles, J. P., Timofeev, O., Nist, A., Mernberger, M., Kantelhardt, E. J., Siebolts, U., Bartel, F., Jacob, R., Rath, A., Moll, R., Grosse, R., & Stiewe, T. (2016). Mutant p53 promotes tumor progression and metastasis by the endoplasmic reticulum UDPase ENTPD5. *Proceedings of the National Academy of Sciences of the United States of America*, *113*(52), E8433–E8442.

Voskuil, J. L. A. (2014). Commercial Antibodies And Their Validation. *F1000research*, *3*(232), 1-15)

Wållberg, H., & Ståhl, S. (2013). Design And Evaluation Of Radiolabeled Tracers For Tumor Imaging. *Biotechnology And Applied Biochemistry*, *60*(4), 365–383.

Wang, X., Sun, Q., Wang, X., & Sun, Q. (2016). Tp53 Mutations, Expression And Interaction Networks In Human Cancers. *Oncotarget*, *8*(1), 624–643.

Weissmueller, S., Manchado, E., Saborowski, M., Morris Iv, J. P., Wagenblast, E., Davis, C. A., Moon, S. H., Pfister, N. T., Tschaharganeh, D. F., Kitzing, T., Aust, D., Markert, E. K., Wu, J., Grimmond, S. M., Pilarsky, C., Prives, C., Biankin, A. V., & Lowe, S. W. (2014). Mutant P53 Drives Pancreatic Cancer Metastasis Through Cell-Autonomous Pdgf Receptor Beta Signaling. *Cell*, *157*(2), 382-394.

Wernick, M. N., & Aarsvold, J. N. (2004). *Emission Tomography : The Fundamentals Of Pet And Spect*. 576.

Wu, J. (2021). The Enhanced Permeability And Retention (Epr) Effect: The Significance Of The Concept And Methods To Enhance Its Application. *Journal Of Personalized Medicine*, *11*(8), 1-8.

Xenaki, K. T., Oliveira, S., & Van Bergen En Henegouwen, P. M. P. (2017). Antibody Or Antibody Fragments: Implications For Molecular Imaging And Targeted Therapy Of Solid Tumors. *Frontiers In Immunology*, *8*(Oct), 1287, 1-5.

Xu, Y., Wang, L., Pan, D., Yan, J., Wang, X., Yang, R., Li, M., Liu, Y., & Yang, M. (2020). Synthesis Of A Novel 89zr-Labeled Her2 Affibody And Its Application Study In Tumor Pet Imaging. *Ejnmmi Research*, *10*(1), 1–10.

Yao, J.-F., Yang, H., Zhao, Y.-Z., & Xue, M. (2018). Metabolism Of Peptide Drugs And Strategies To Improve Their Metabolic Stability. *Current Drug Metabolism*, *19*(11), 892–901.

Zhang, L., Sanagapalli, S., & Stoita, A. (2018). Challenges In Diagnosis Of Pancreatic Cancer. *World Journal of Gastroenterology*, *24*(19), 2047–2060.

Zhang, W. H., Wang, W. Q., Han, X., Gao, H. L., Li, T. J., Xu, S. S., Li, S., Xu, H. X., Li, H., Ye, L. Y., Lin, X., Wu, C. T., Long, J., Yu, X. J., & Liu, L. (2020). Advances On Diagnostic Biomarkers Of Pancreatic Ductal Adenocarcinoma: A Systems Biology Perspective. *Computational And Structural Biotechnology Journal*, *18*, 3606–3614.

Zhao, L., Ren, T. H., & Wang, D. D. (2012). Clinical Pharmacology Considerations In Biologics Development. *Acta Pharmacologica Sinica*, *33*(11), 1339–1347.

Zhou, Q. (2017). Site-Specific Antibody Conjugation For Adc And Beyond. *Biomedicines*, *5*(4), 1-15.

Zhou, X., Hao, Q., & Lu, H. (2019). Mutant P53 In Cancer Therapy—The Barrier Or The Path. *Journal Of Molecular Cell Biology*, *11*(4), 293-395.

8 Appendix

8.1 Western blot

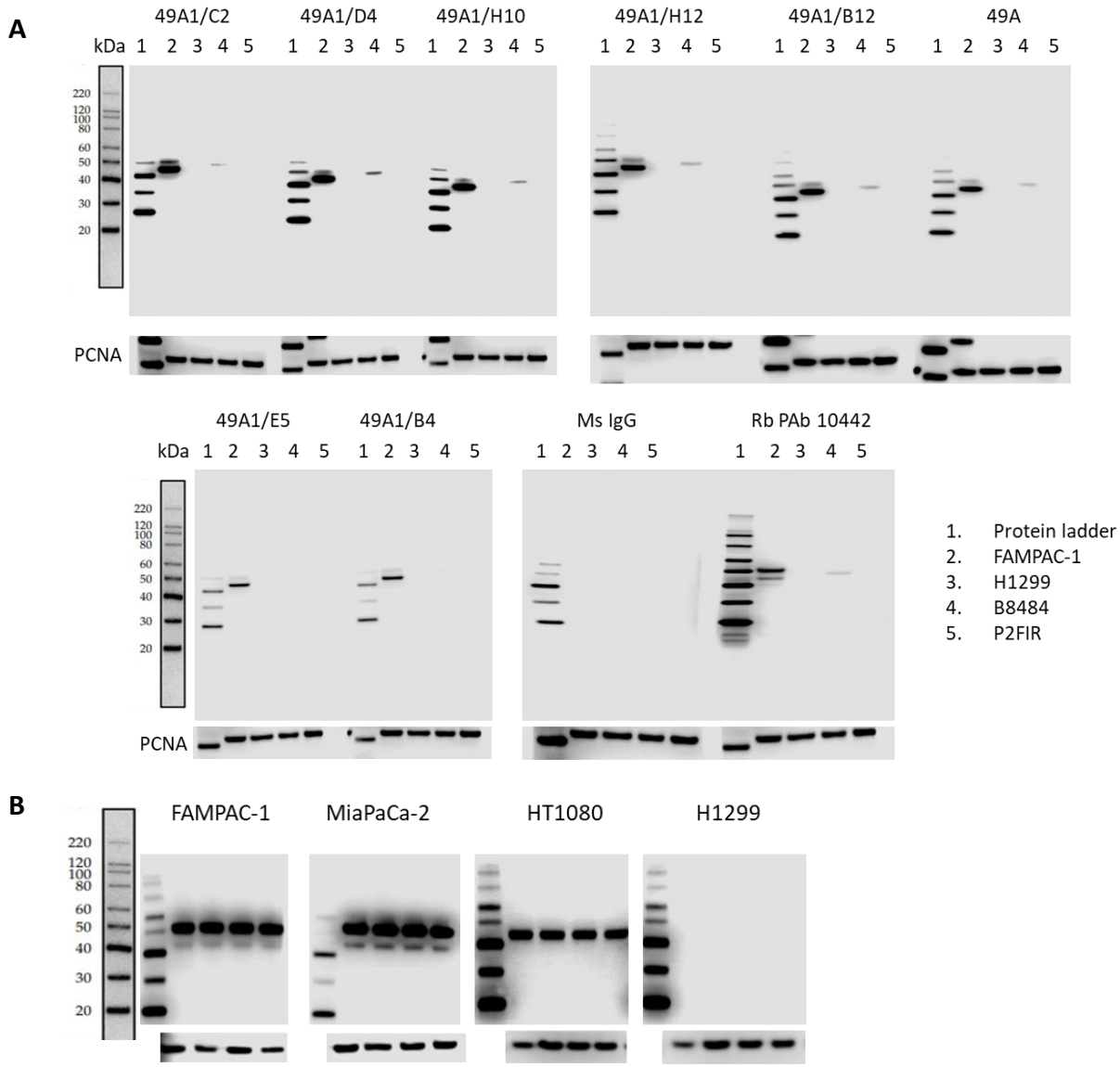


Figure 8:1) Western blot analysis of p53 antibodies. **A)** Analysis of specificities of the eight novel p53 antibodies on cell extracts. **B)** Analysis of anti-p53 49A1/H10 specificity on total p53 protein (mutant and wild type p53). Membranes were incubated with the primary p53 antibodies and then probed by HRP-conjugated anti-mouse IgG secondary antibody and imaged using the C-DiGit Chemiluminescent Western Blot Scanner. After imaging, membranes were washed with Western blot stripping buffers and probed for PCNA loading control using Anti-PCNA antibody.

8.2 Biodistribution data in percentage injected dose per gram (%ID/g)

Table 8.1) Biodistribution data (raw) of MiaPaCa-2 xenografts in %ID/g. (RIC – radioimmunoconjugate)

RIC	Anti-p53 (49A1/H10						MIgG				
Mouse	M1	M2	M3	M4	Average	STDEV	M6	M7	M8	Average	STDEV
Blood	5.26	5.65	11.02	6.71	7.16	2.65	3.44	3.06	5.28	3.93	1.19
Spleen	1.73	1.72	3.58	2.66	2.42	0.89	1.28	1.39	0.87	1.18	0.27
Pancreas	0.46	0.55	0.99	1.01	0.75	0.29	0.32	0.49	0.77	0.53	0.23
Kidney	1.75	2.14	3.31	2.73	2.48	0.68	1.52	1.83	3.07	2.14	0.82
Liver	15.13	15.85	22.98	20.81	18.69	3.81	17.25	14.75	15.57	15.86	1.27
Lungs	2.25	2.47	3.97	3.25	2.99	0.78	1.48	1.73	3.69	2.30	1.21
Heart	1.68	2.26	3.62	1.49	2.26	0.96	1.25	1.09	2.25	1.53	0.63
Muscle	0.57	0.68	1.03	0.9	0.80	0.21	0.4	0.44	0.65	0.50	0.13
Bone	0.48	0.9	1.03	0.94	0.84	0.24	0.4	0.45	0.92	0.59	0.29
Tumour	3.27	3.51	5.42	3.94	4.04	0.96	2.08	0.7	1.64	1.47	0.70

Table 8.2) Raw biodistribution data of HT1080 xenografts in %ID/g.

RIC	Anti-p53 (49A1/H10)						MIgG					
Mouse	M11	M12	M13	M14	Average	STDEV	M16	M17	M18	M19	Average	STDEV
Blood	1.81*	11.39	8.42	9.06	9.62	1.56	6.01	4.76	5.92	8.22	6.23	1.45
Spleen	0.68*	5.2	3.41	3.42	4.01	1.03	3.47	2.39	2.65	6.81	3.83	2.04
Pancreas	0.16*	0.96	1.09	0.82	0.96	0.14	0.76	0.59	0.6	0.84	0.70	0.12
Kidney	1.04*	3.87	3.91	5.18	4.32	0.75	3.24	3.12	3.02	4.04	3.36	0.47
Liver	6.29*	17.72	22.07	18.86	19.55	2.26	13.22	9.27	10.51	17	12.50	3.42
Lungs	0.74*	5.13	4.65	4.07	4.62	0.53	3.27	2.53	3.58	4.33	3.43	0.75
Heart	0.55*	4.5	3.06	2.77	3.44	0.93	2.53	1.8	1.88	2.28	2.12	0.34
Muscle	0.22*	1.3	0.83	1.08	1.07	0.24	0.86	0.69	0.72	0.84	0.78	0.09
Bone	0.29*	2.95	4.13	2.87	3.32	0.71	1.34	1.06	1.06	1.65	1.28	0.28
Tumour	1.08*	6.1	5.42	5.38	5.63	0.40	2.66	2.43	2.72	3.63	2.86	0.53

Table 8.3) Raw biodistribution data of H1299 xenografts in %ID/g.

RIC	Anti-p53 (49A1/H10)					MIgG				
Mouse	M21	M22	M23	Average	STDEV	M26	M27	M28	Average	STDEV
Blood	7.27	8.37	12.12	9.25	2.54	10.31	11.32	8.48	10.04	1.44
Spleen	2.56	2.91	5.88	3.78	1.82	5.72	4.25	1.91	3.96	1.92
Pancreas	0.72	0.79	0.86	0.79	0.07	0.86	0.79	0.44	0.70	0.23
Kidney	2.36	2.77	2.92	2.68	0.29	3.71	3.05	2.01	2.92	0.86
Liver	12.95	14.71	13.76	13.81	0.88	15.02	21.6	14.15	16.92	4.07
Lungs	2.7	3.13	5.34	3.72	1.42	4.23	6.6	2.42	4.42	2.10
Heart	2.61	3.12	4.02	3.25	0.71	2.83	3.2	1.22	2.42	1.05
Muscle	0.82	0.93	1.24	1.00	0.22	1.09	1.1	0.97	1.05	0.07
Bone	0.85	1.08	1.86	1.26	0.53	1.54	1.62	0.58	1.25	0.58
Tumour	2.64	3.55	3.97	3.39	0.68	3.99	4.08	4.6	4.22	0.33

8.3 SPECT images VOI data injected activity per millilitre (IA/mL)

Table 8.4) Raw data in IA/mL of [^{111}In]-DTPA-49A1/H10-TAT in MiaPaCa-2 xenografts.

Timepoint	24 h						48 h						72 h					
Mouse	M1	M2	M4	M4	Average	STDEV	M1	M2	M4	M4	Average	STDEV	M1	M2	M4	M4	Average	STDEV
Tumour	1.87	1.26	1.27	1.52	1.48	0.29	3.25	2.04	1.54	1.38	2.05	0.85	3.45	2.77	1.79	2.42	2.61	0.69
Muscle	0.41	0.15	0.36	0.33	0.31	0.11	0.38	0.21	0.47	0.34	0.35	0.11	0.4	0.27	0.39	0.5	0.39	0.09
Liver	6.4	6.34	7.81	9.63	7.55	1.55	10.58	5.98	6.47	8.52	7.89	2.11	6.89	5.5	5.63	7.75	6.44	1.07
Heart	4.28	2.83	2.7	4.42	3.56	0.92	3.22	2	1.99	3.44	2.66	0.78	2.66	1.39	1.17	1.38	1.65	0.68

Table 8.5) Raw data in IA/mL of [^{111}In]-DTPA-MIgG-TAT in MiaPaCa-2 xenografts.

Timepoint	24 h					48 h					72 h				
Mouse	M6	M7	M8	Average	STDEV	M6	M7	M8	Average	STDEV	M6	M7	M8	Average	STDEV
Tumour	0.83	0.66	0.37	0.62	0.23	1.17	0.58	0.24	0.66	0.47	1.04	0.55	0.36	0.65	0.35
Muscle	0.37	0.16	0.17	0.23	0.12	0.16	0.27	0.11	0.18	0.08	0.23	0.17	0.14	0.18	0.05
Liver	7.94	7.22	6.68	7.28	0.63	6.96	6.04	5.47	6.16	0.75	6.21	5.43	5.02	5.55	0.60
Heart	2.43	1.44	1.8	1.89	0.50	1.98	1.27	1.43	1.56	0.37	1.69	0.98	0.96	1.21	0.42

Table 8.6) Raw data in IA/mL of [^{111}In]-DTPA-49A1/H10-TAT in HT1080 xenografts.

Timepoint	24 h						48 h						72 h					
Mouse	M16	M17	M18	M19	Average	STDEV	M16	M17	M18	M19	Average	STDEV	M16	M17	M18	M19	Average	STDEV
Tumour	0.75	0.73	0.73	1.42	0.91	0.34	1.14	0.36	0.58	0.58	0.67	0.33	0.8	0.34	0.68	1.06	0.72	0.30
Muscle	0.32	0.23	0.23	0.38	0.29	0.07	0.17	0.1	0.18	0.18	0.16	0.04	0.13	0.14	0.15	0.19	0.15	0.03
Liver	5.1	5.86	4.39	5.89	5.31	0.71	5.96	6.12	8.14	8.16	7.10	1.22	7.45	8.5	7.87	6.16	7.50	0.99
Heart	2.6	1.84	1.84	3.19	2.37	0.66	1.61	0.77	1.36	1.37	1.28	0.36	1.31	1.16	0.75	1.46	1.17	0.31

Table 8.7) Raw data in IA/mL of [^{111}In]-DTPA-MIgG-TAT in HT1080 xenografts.

Timepoint	24 h					48 h					72 h				
Mouse	M11	M12	M13	Average	STDEV	M11	M12	M13	Average	STDEV	M11	M12	M13	Average	STDEV
Tumour	3.09	2.89	2.99	2.99	0.10	3.45	3.62	3.62	3.56	0.10	4.87	4.56	4.76	4.73	0.16
Muscle	0.79	0.37	0.45	0.54	0.22	0.29	0.47	0.47	0.41	0.10	0.39	0.48	0.39	0.42	0.05
Liver	5.49	5.99	5.9	5.79	0.27	5.64	8.48	8.48	7.53	1.64	7.71	7.99	7.84	7.85	0.14
Heart	5.21	4.29	4.49	4.66	0.48	2.48	3.28	3.28	3.01	0.46	2.85	2.75	3.05	2.88	0.15

Table 8.8) Raw data in IA/mL of [^{111}In]-DTPA-49A1/H10-TAT in H1299 xenografts.

Timepoint	24 h					48 h					72 h				
Mouse	M21	M22	M23	Average	STDEV	M21	M22	M23	Average	STDEV	M21	M22	M23	Average	STDEV
Tumour	1.73	1.41	1.39	1.51	0.19	1.24	1.49	1.46	1.40	0.14	1.36	1.4	1.27	1.34	0.07
Muscle	0.49	0.22	0.42	0.38	0.14	0.27	0.33	0.44	0.35	0.09	0.25	0.42	0.45	0.37	0.11
Liver	7.22	7.82	5.93	6.99	0.97	5.85	6.53	5.02	5.80	0.76	5.24	6.09	4.1	5.14	1.00
Heart	3.39	4.39	4.25	4.01	0.54	3.17	3.15	2.56	2.96	0.35	2.01	2.32	1.72	2.02	0.30

Table 8.9) Raw data in IA/mL of [^{111}In]-DTPA-MIgG-TAT in H1299 xenografts.

Timepoint	24 h					48 h					72 h				
Mouse	M26	M27	M28	Average	STDEV	M26	M27	M28	Average	STDEV	M26	M27	M28	Average	STDEV
Tumour	1.27	2.4	0.8	1.49	0.82	1.6	2.26	1.48	1.78	0.42	1.4	1.86	0.79	1.35	0.54
Muscle	0.38	0.34	0.19	0.30	0.10	0.27	0.33	0.32	0.31	0.03	0.33	0.44	0.15	0.31	0.15
Liver	6.49	8.08	7.46	7.34	0.80	5.98	7.23	7.37	6.86	0.77	4.03	6.28	5.68	5.33	1.17
Heart	3.89	3.86	2.1	3.28	1.02	3.59	3.45	1.41	2.82	1.22	3.12	2.88	1.38	2.46	0.94

Table 8.10) Anti-p53 (49A1/H10) mAb – peptides Pearson R correlation coefficients from coloco2 analysis.

	FAMPAC-1				MiaPaCa-2			
	Peptide 1	Peptide 2	DAPI	DAPI	Peptide 1	Peptide 2	DAPI	DAPI
49A1/H10	0.59	0.56	0.69	0.75	0.38	0.36	0.69	0.68
	HT1080				H1299			
	Peptide 1	Peptide 2	DAPI	DAPI	Peptide 1	Peptide 2		
49A1/H10	0.67	0.75	0.62	0.75				
DAPI					0.47	0.52		

8.4 Dedication

I dedicate this work to the memory of my grandfather, the late teacher Abiud Etabale Alakonya (1943 – 1975). You loved education so much, and you were passionately committed to educating young people and transforming our community. My dad told me you had promised to educate him up to the University of Oxford. Unfortunately, he could not make it because of the socioeconomic challenges that beset his fate of earth after you passed away. I hope my success brings you more peace and joy where you are in heaven. God rest you soul in eternal peace.